Simulation of Realistic Images and Exoplanet Detection for Starshade Missions

Mengya Hu

A Dissertation
Presented to the Faculty
of Princeton University
in Candidacy for the Degree
of Doctor of Philosophy

Recommended for Acceptance
by the Department of
Mechanical and Aerospace Engineering
Adviser: N. Jeremy Kasdin and Robert J. Vanderbei

May 2021

Abstract

A starshade suppresses starlight by a factor of 10^{11} in the image plane of a telescope, which is crucial for directly imaging Earth-like exoplanets. The state of the art in high-contrast signal detection methods was developed specifically for coronagraph images and focuses on the removal of quasi-static speckles. These methods are less useful for starshade images where such speckles are not present. This work is dedicated to investigating signal detection tailored to starshade images.

I begin with the first step towards the investigation: realistic starshade image simulation. The simulation considers factors such as starshade defects and detector noise. Then, signal detection methods are presented.

Due to the absolute faintness of Earth-like planets, an Electron Multiplying Charged Coupled Device operating in photon counting (PC) mode is used. Typically, PC images are added together as a co-added image before processing. Therefore, I first introduce a detection method based on a generalized likelihood ratio test (GLRT) for co-added images under the Gaussian assumption. I also extend the method to mitigate the effect of exozodiacal dust. Then, I improve the method by working directly with individual PC images using a Bernoulli distribution. The Bernoulli distribution is derived from a stochastic model for the detector, which accurately represents its noise characteristics. I show that my techniques outperform a popular detection algorithm based on signal to noise ratio.

Besides successfully flagging the dim planets, my methods provide the maximum likelihood estimate of exoplanet intensity and background intensity while doing detection. Moreover, my methods can help distinguish planet signals from artifacts caused by starshade defects. It can also guide stopping observations early, providing confidence for the existence (or absence) of planets. As a result, the observation time is efficiently used. Besides the observation time, the analysis of detection performance introduced in the thesis also gives quantitative guidance on the choice of imaging

parameters, such as the threshold for PC mode. Last but not the least, though this work focuses on the example of detecting point sources in starshade images, the framework is widely applicable. All the methods are demonstrated on realistic simulated images.

Acknowledgements

First and foremost, I would like to express my highest gratitude and appreciation for everything that my advisor, Prof. N. Jeremy Kasdin, has helped me achieve here. Jeremy provided me with the amazing opportunity to work on exoplanet exploration, which sets a great tone for my whole graduate school life. Jeremy is knowledgeable, supportive, patient, encouraging, easy-going, and humorous. Despite his busy schedule, Jeremy always replies to my emails promptly and allocates time to meet me when needed. I still remember that in our first emails, I asked about the basic concept of suppression, and Jeremy replied to me with a detailed explanation and the intuition behind it while traveling. I also vividly remember how we met every week to revise my presentation together before my general exam. It is the first time that I learn that a good presentation should be like telling a story. I continue to learn a lot from his wealth of knowledge and experience both in research and in life for years to come. It is such a privilege! Graduate school is not a smooth ride. There are times when I doubt myself. Jeremy is always generous in offering compliments, which helps a lot for me to regain confidence. I am also grateful for his unwavering support in my exploration of both research topics and life choices. His passion for engineering, science, art, and life, and his courage of restarting his career are inspiring. I hope to someday be like him.

I would like to thank my co-advisor, Prof. Robert Vanderbei, who gives me guidance on optimization and optics. I am also inspired by his broad interests and successful application of science to various areas in life. I also want to express my sincere gratitude to my committee members, Prof. Michael Littman and Prof. Robert Stengel, for the continuous support and constructive suggestions. I admire their great achievement in academia and devotion to teaching. Thank you to my thesis readers, Prof. Anirudha Majumdar and Prof. Peter Melchior, for the time and the comments. I would like to thank Prof. Peter Ramadge. I benefit a lot from the Graduate Cer-

tificate Program in Statistics and Machine Learning at the Center for Statistics and Machine Learning (CSML) that he leads. I would also like to thank Susan Johansen to make my experience of the certificate program great. I also want to express my gratitude towards MAE staff, who made my Princeton life wonderful. Special thanks to Jill Ray, Theresa Russo, and Katerina Zara, who are devoted to making our graduate program smooth and enjoyable. Jill not only did her work well but also cared for graduate students wholeheartedly. I am very grateful for her help especially through my rough times.

One of the very rewarding aspects of my graduate school has been the interaction with a superb group of colleagues and friends. I would like to thank both the previous and current members of High Contrast Imaging Lab: Dr. Tyler Groff, Dr. A.J. Riggs, Dr. Hari Subedi, Michael Galvin, Dr. Jessica Gersh-Range, Dr. Yunjong Kim, Dr. Anthony Harness, Dr. Christian Delacroix, Dr. Alexei Goun, Dr. Leonel M. Palacios Moreno, Dr. He Sun, Peter Varnai, Aaron Lemmer, Steven (Lun) Li, Susan Redmond , and Dr. Leonid Pogorelyuk. I am grateful to Yunjong for introducing me to the current research and training me on the modelling of starshades. I would also like to thank Jessica for all the help on my research, especially her detailed explanation on optics when I first joined the group. Special thanks to Anthony! I have learned so much from him. I'm so appreciative of the countless hours that he spent on discussing research with me, revising my papers, and talking about life. His passion and devotion to starshade and making the world a better place inspires me. His invaluable advice always pushing me to be the best I can be. I was nervous when traveling to new places and was clueless during the first conferences. Anthony was such a great mentor and friend, who guided me through and accompanied me. I enjoyed all these trips! I also want to thank He. He is not only an amazing labmate and officemate but also like a brother to me. We both spent many hours in the office every day, so he was usually the first person that I shared my happiness and frustra-

tion with. There are so many times my research got stuck, or I doubted myself, or I was uncertain about the future, or I had difficult choices or I faced challenges. He always assured me with his own experience, brainstormed helpful ideas, and encouraged me to believe in myself. Thank He for developing my 'can-do' spirit. I am so grateful to him for all the support! I would also like to express my gratitude to Mike. Mike is a thoughtful and caring friend, who always has my back. He is very inclusive when planning group activities(He knows my fear for height, speed, and water, and always avoids them to make the activities 'Mia-friendly'). I'm also grateful for his mentorship on navigating life in America. He has saved me from several crisis in the past years! I would also like to thank Dr. Maxime Rizzo, who helped me a lot on the image simulation by giving me guidance on Haystack and detector model.

I would like to thank my entire cohort: Dr. Adam Fisher, Dr. Alex Novoselov, Andreas Rousing, Anthony Savas, Ben Reimold, Dr. David Feng, Dr. Fan Yang, Dr. Katherine Kokmanian, Kristofer Meehan, Tara Charlotte, Tasman (Andrew) Powis, Dr. Thomas Hodson, Tianhan Zhang, Vanessa Obiageli Uzonwanne, Vivian Steyert, Yaofeng (Desmond) Zhong and Dr. Yingxian (Estella) Yu. They are the first friends I made in America. We share a lot of good and bad memories (and memes) from Graduate school. I am thankful for all their support and companionship. Special thanks to Fan Yang. I am a person who easily buries herself in work all day long. It is Fan who 'drags' me to enjoy other parts of life. We had ice cream break, bubble tea beaks and gym breaks. We went grocery shopping together and fulfilled our Chinese stomach together. I am really glad that we met. I would also like to thank all the friends at lunch table and social chairs: Dr. Sebastian Rojas Mata, Dr. Bruce Perry, Dr. Bec Gray, Kerry Klemmer, Daniel Dudt, Dr. Christopher Peters, Dr. Yibin Zhang, Jessica Wilson, Dr. Mike Hepler, Dr. Cody Nunno, Julienne LaChance, Meghan Booker, Danielle Chase, Dr. Yao Lai and Dr. Matthew Edwards. Lunch is more enjoyable because of you guys. Though there are only a few names

mentioned here, there are a lot of people who made my Princeton life special and I am grateful to them.

Last but not the least, I would like to thank my family. Thank you to my partner, Zuzhao Ye, for caring and supporting me wholeheartedly. He tried his best to nurture our relationship despite the long distance. He kept me company through the highs and lows. I still remember his surprise visit during my first year in graduate school, when I was so stressed about a sudden change. He can always calm me down and cheer me up. I am looking forward to more adventures together. I also want to thank my father Deshui Hu, mother Fang Cheng, elder sister Mengdie Hu, little sister Mengni Hu and little brother Mengyuan Hu. I always feel lucky that I have such a great family! Our video calls every week are the most relaxing time of the week. I feel safe and happy because you are always there for me. Mom and Dad, Thank you for believing in me and supporting me to explore whatever I want to try. What I have achieved seems unbelievable to me (considering what we have) from time to time. And I know the achievement is made possible by you. It is you who made the correct choices for me when I was too young and knew little at the turning points in life. It is you that give all you have to us and try your best to make our life and future better. Thank you! Mengdie, Mengni and Mengyuan, you are a true gift to me! Because of you, I never feel alone. The reason why I can chase my dream on this land far away from home with little worry is that you take care of our parents well. Mengdie, Thank you for your continued support! As the big sister in the family, you bear the most hardship and thus the rest of us bear so much less. As you are older but in the same generation, you know best about what I need and am struggling with (sometimes even better than myself). Your care and continued support made my life so much easier. You are always the first person I seek help from. Without you, I will never be able to land where I am today. As my family are not good at English, I will write my gratitude for them again in Chinese: 我要感谢我的家人：爸爸胡德水，妈妈程

芳，姐姐胡梦蝶，妹妹胡梦妮和弟弟胡梦圆。能有你们这样的家人，我非常幸运！每周的视频通话闲扯是我每周最放松的时光。有你们在，我非常安心和快乐。爸，妈，我非常您们对我的信任和支持我探索任何我想做的事。有时候我会觉得我现有的成就难以想象（考虑到我们所拥有的）。我知道是您们让这一切变得可能。是您们在各个人生的转折点，在我还小还很无知的时候为我做出了正确的选择。您们为我们奉献了所有，尽全力为我们创造好的生活条件和未来。感谢您们！梦蝶，梦妮和梦圆，你们是我生命中的礼物。因为有你们在，我从来不孤单。我之所以能在远离家乡的异国安心奋斗是因为有你们在家照顾着爸妈。梦蝶，我要特别感谢你对我一如既往的支持！你因为是家里老大，为我们承受了最多的艰难困苦，让我们剩下三个小的感受不到什么困难。你比我大，但是还是同一代人，所以你最了解我需要什么，我有什么困难（有时候比我自己还了解）。因为你的关心和帮助，我的生活轻松美好。有什么事，我总第一时间向你求助。没有你的话，我不可能有现在的一切。

Years have flown by, and I can't believe they are coming to an end. I am honored and feel extremely lucky that I get the opportunity to live, study and work in Princeton. It is a beautiful place with an amazing history and wonderful people. It is the first place I have lived other than my motherland and opens my eye to different cultures. It will always be a special place for me. Moreover, this is not only the end of my graduate school but also my school life. I have always been lucky to have good teachers and peers, who are not explicitly mentioned in this acknowledgment. This graduation means parting ways with most of them. However, I will always be grateful and appreciate all the support and the good times we shared together!

This work is supported by Caltech-JPL NASA grant NNN12AA01C. Different parts of this work has been presented in following conferences: SPIE Optical Engineering + Applications, 6−10 August 2017; the 231th Meeting of the American Astronomical Society, 8−12 January 2018; SPIE Optics + Photonics, 19−23 August 2018; the 233rd Meeting of the American Astronomical Society, 6–10 January 2019;

SPIE Optical Engineering + Applications, 11−15 August 2019; the 235th Meeting of the American Astronomical Society, 4−8 January 2020.

This dissertation carries T#3409 in the records of the Department of Mechanical and Aerospace Engineering.

To my family.

Contents

List of Tables

List of Figures

Chapter 1

Introduction

1.1 The search for other worlds

The question "Are we alone in the Universe?" has been around for thousands of years. Human beings have long been pondering over the question, speculating on it, debating it philosophically and romantically imagining the possible other worlds. In the 1990s, we eventually made exciting concrete progress to address the question in the last decades by discovering the first exoplanets[75]. It forcefully responds to the skepticism about the existence of exoplanets. Since then, the field of exoplanet research has been developing fast: thousands of new exoplanets have been observed and their properties have been studied.

The reason why the concrete progress didn't happen until the late twentieth century is not the lack of exoplanets in the Universe but that exoplanets are so hard to find. First, the exoplanets are far. Proxima Centauri, the closest star to our Sun, is 4.2 light-years away. Two planets have been found orbiting around it[2, 24]. Without any closer stars, we don't expect to find any closer exoplanets. Second, exoplanets are dim. While stars generate light by intense nuclear fusion in their interiors, planets shine either only by reflection or by thermal radiation as a by-product of their forma-

tion. A sun-like star is much brighter (typically 100 million to 10 billion times) than an Earth-like planet in its habitable zone [103]. Last but not the least, the biggest problem is that dim exoplanets are close to their star. At a distance of 10 pc, the star and the planets in its habitable zone are separated by around 0.1 arcseconds. Thus, it is difficult to separate the planet light from that of the star.

1.2 Ways to find exoplanets

1.2.1 Indirect Methods

At first, astronomers tackled the challenges by inferring the existence of the exoplanets from the starlight rather than directly observing the planets. One such method is Radial Velocity (RV), which brought the research field of exoplanets to light by discovering the first exoplanets. It has detected 821 exoplanets[76]. This method is also often used to confirm planets found with other methods. The RV method is based on the Doppler effect. It measures the line-of-sight (radial) velocity component of a star's motion. Consider a star with a planet, the plane of whose orbit lies in the line of sight towards our telescope. Since both the star and the planet move around their center of mass, the star will appear to move back and forth from the telescope. Thus, the light collected will oscillate between a red-shifted extreme and blue-shifted extreme[45]. This method provides us the knowledge of the orbital properties of the system: the period, the eccentricity, the semi-major axis, the argument of periastron, the time of periastron, and the minimum mass[17]. To validate that the Doppler effect is caused by a planet rather than a faint star or a brown dwarf, we can calculate the mass of the companion, when knowing the mass of the star and its velocity. If the mass is small enough, we can infer that the companion is a planet.

Another method is the transit method. It detects the exoplanet by observing the periodic stellar luminosity decrease[7]. The decrease happens when a planet

passes directly between its star and an observer, blocking some of the star's light[32]. Transits can help unveil important information about the planet: the period, the orbital radius, the time of the contact points, the inclination of the orbit, the radius of the planet, and the actual mass of the planet (if following it up with a spectrograph and RV)[17]. During a transit, a small portion of the starlight is filtered through the upper atmosphere of the planet, where it is wavelength-dependency due to the scattering properties of atoms and molecules in the planetary atmosphere. Thus, it may reveal the knowledge of the atmosphere's composition[91]. The transit method has found 3275 exoplanets[76]. Largely due to NASA's Kepler mission, its number of exoplanet discoveries has surpassed that of the RV method[45].

The third detection method is gravitational microlensing. In this technique, light from a distant (source) star is observed as another star at an intermediate distance (the lens star) passes close to, or in front of it. Light from the source star is gravitationally bent around the lens star and thus its apparent magnitude changes during the event[55]. The method has detected 106 exoplanets[76]. Microlensing is a rare event. Astronomers can't predict when or where these lensing events will happen, so they have to watch large parts of the sky over a long period of time[31].

The fourth method is astrometry. As mentioned in RV, a star will wobble around in space due to a planet around it. Instead of measuring the radial component of the star motion, the astrometry method measures the change of the star's apparent position in the sky[30]. It has discovered 1 exoplanet[76].

Orbital brightness modulation is a helpful method to detect an exoplanet in close orbits even if it does not transit the star. As the planet goes through phases, the reflected star-light will vary. As the planet is not resolved, its host star appears to vary periodically. Therefore, this method is biased toward large, close-in planets with high albedos, because they reflect more starlight[4]. Six exoplanets have been discovered with this method[76].

Timing variations include a set of detection methods, which is based on an exoplanet's perturbations on the system's periodic behavior. One of them is the transit timing variation method. The method uses the fact that an exoplanet (planet A) will not transit with a fixed period if the exoplanet is perturbed by another exoplanet (planet B). Though planet B is 'unseen' in the transit, we can infer its presence from planet A's transit. This provides the opportunity to detect additional planets in the system with masses potentially as small as that of Earth[49]. Twenty-one exoplanets have been discovered by the transit timing variation method[76]. The eclipse timing variation method observes binary stars. The brightness of the whole binary star system varies when they orbit around and eclipse each other. A planet orbiting the eclipsing binary will result in changes in the period of the eclipsing binary. The eclipse timing variation method has found 16 exoplanets[76]. Pulsar Timing Variations method made one of the first exoplanet discoveries[111]. The high accuracy of pulsar timing allows low mass bodies orbiting the pulsar to be detected from changes in pulse arrival times[79]. The method has detected 7 exoplanets[76]. The method of pulsation timing variations detects planets by monitoring the pulsation arrival times of a pulsating star, which is influenced by an external companion. This method is most sensitive to detecting substellar companions around the hottest pulsating stars, especially compact remnants like white dwarfs and hot subdwarfs, as well as A stars[46]. Two exoplanets have been discovered by this method[76].

The most efficient methods among the above methods, the RV method, and transit method, are biased towards planets in close orbits, typically smaller than 5 au[17]. The RV method is biased towards giant, close-orbiting, large-period planets, and the transit method is biased towards larger planets orbiting smaller stars[55, 17]. Moreover, the two methods are also hampered by astrophysical noise from the host star itself, such as the stellar pulsations and surface granulation for RV and spots for transit[17]. Last but not the least, all the techniques above are indirect detection

methods, inferring the existence of an exoplanet by observing the change of its host star's light.

1.2.2 The Direct Method: Direct Imaging

Regarding these biases, direct imaging can help. This method detects a planet either in the reflected light from the parent star (in the visible), or through its own thermal emission (in the infrared)[79]. First of all, this method is complementary to other methods by exploring the outer regions of exoplanetary systems. It is the only technique currently available to detect planets with semi-major axes greater than about 5 au in a reasonable amount of time[17]. The distribution of mass and period of confirmed exoplanets discovered via different methods is shown in Fig. 1.1. Moreover, this method is the only direct detection method. It provides valuable photometric, spectroscopic, and astrometric measurements of the detected companions, which is fundamental to characterize the planets. This provides information to identify the atmosphere's composition and determine the pressure-temperature profile[17]. It would strongly suggest the existence of life if bio-markers such as O_2, O_3 and CH_4 are present at significant abundance[56]. This evidence of the presence of life helps answer the ultimate question, "Are we alone".

1.3 High-contrast imaging

The first direct image of an exoplanet was taken in 2004 [16] and the discovery was published in 2008[29]. This detection came a decade after the first exoplanet discovery and hundreds of exoplanets had been discovered indirectly. The reason for this lag is that direct imaging of exoplanets is extremely difficult. The two challenges for direct imaging are the large contrast between the host star and the planets, and the small angular separation between them. High-contrast imaging is defined as any

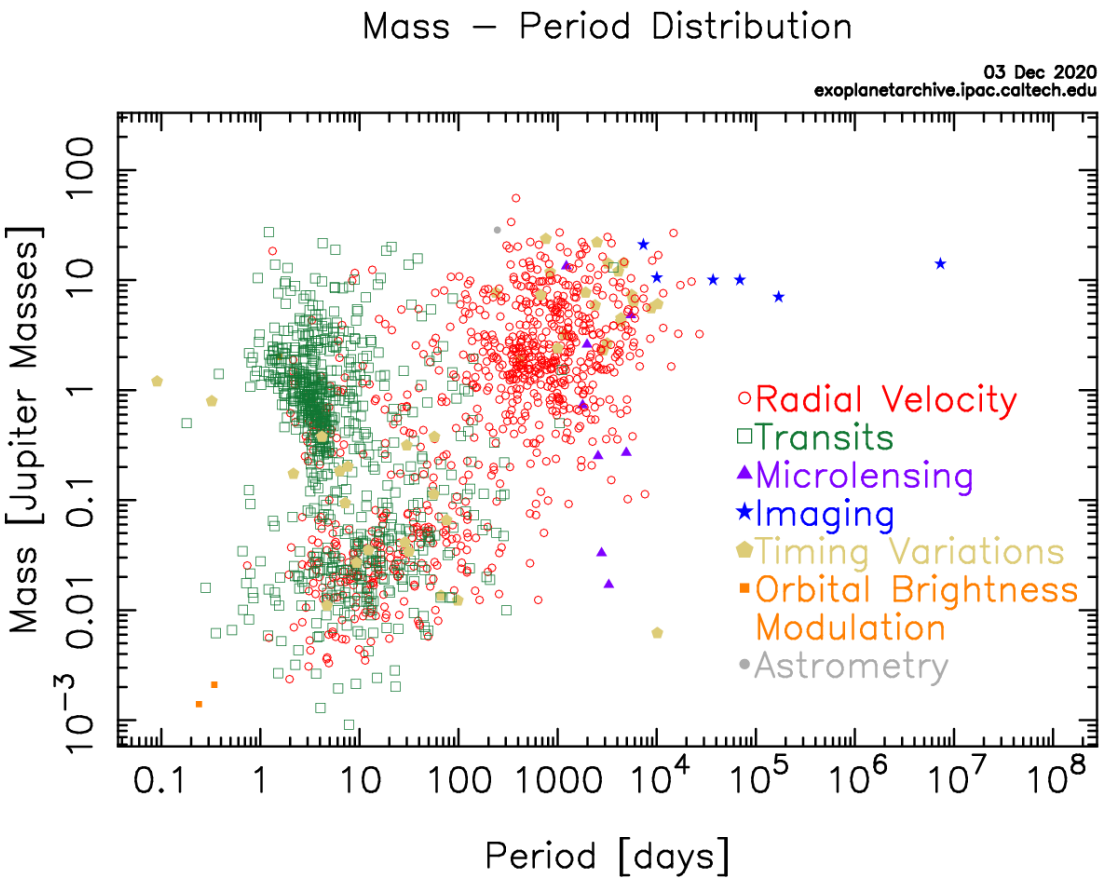

Figure 1.1: Mass vs period for confirmed exoplanets. Not all current detections are in the plot because their parameters are not known. The plot is obtained from the NASA exoplanet archive.

imaging techniques revealing a celestial object of interest that is in such close angular proximity to another source brighter by a factor of at least 10^5, that optical effects hinder or prevent the collection of photons directly from the target of observation[17]. A sun-like star is much brighter (typically 100 million to 10 billion times) than an Earth-like planet in its habitable zone [103]. Model spectrum comparison of the Sun and the planets[104] is shown in Fig. 1.2 . Moreover, at a distance of 10 pc, the star and planets in its habitable zone are separated by around 0.1 arcseconds. Thus, it is difficult to separate the planet light from that of the star in the image using conventional imaging techniques. New techniques are needed. There are two main

solutions to the challenge of imaging objects in close proximity to much brighter ones: the coronagraph and the starshade.

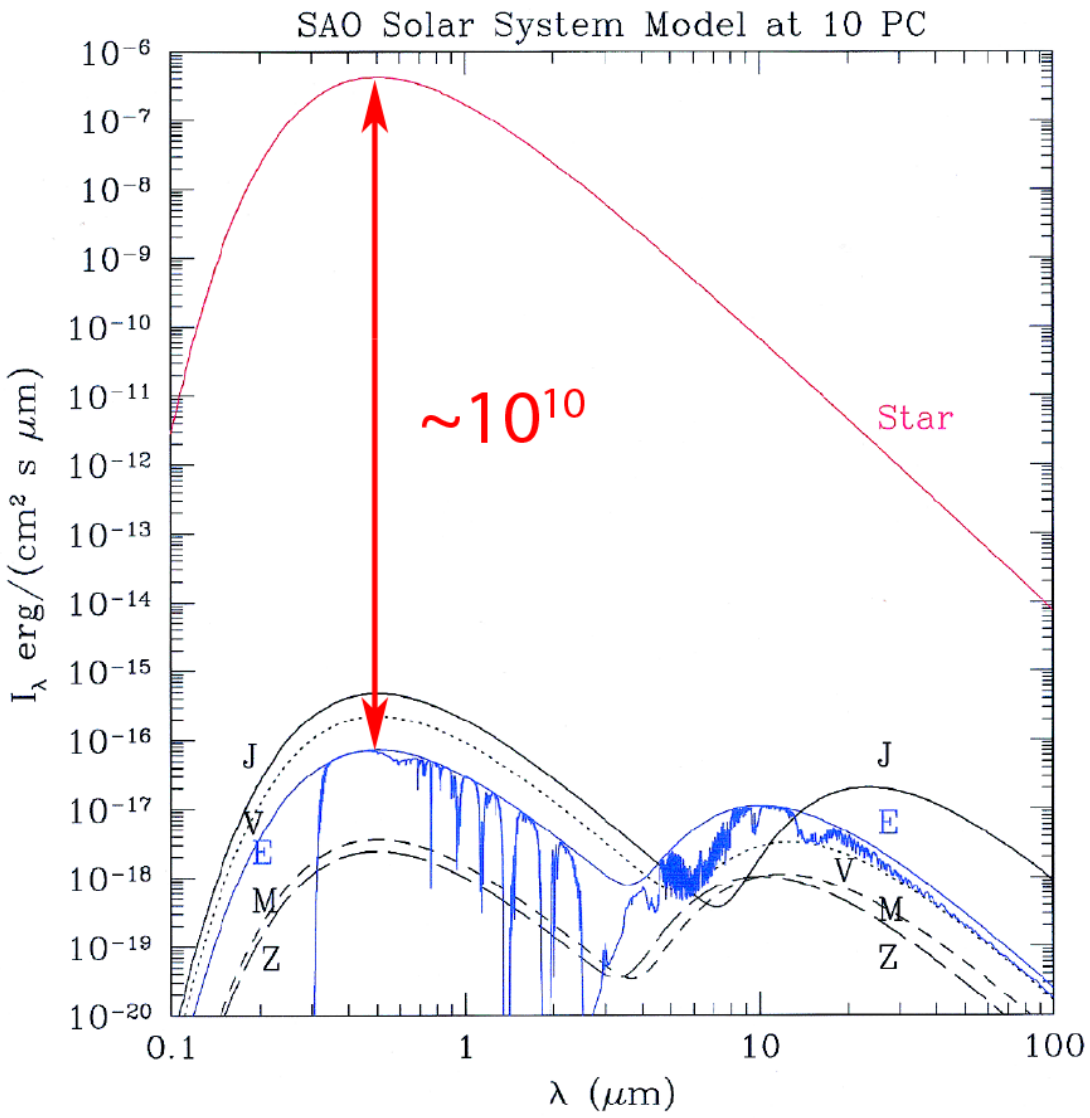

Figure 1.2: Model spectrum comparison of the Sun and the planets as seen from 10 pc[104].

1.3.1 Coronagraphs

Generally speaking, coronagraphs are the optical devices inside the telescope to attenuate the starlight. There are two types of coronagraphs: Lyot-type coronagraphs

and apodizers[83]. Lyot-type coronagraphs create contrast by blocking the starlight. It was named after French astronomer Bernard Lyot, who invented it to block the sun and observe the outer atmosphere of the sun[66]. Apodizers obtain contrast by changing the point spread function (PSF). Numerous variations of the coronagraphs have been invented[18, 11, 63, 87]. Our group at Princeton developed a type of binary apodizers called shaped pupil coronagraph[98, 59, 12, 106]. The pupil is designed to be either fully transmissive or fully opaque in different regions. Coronagraphs are extremely sensitive to wavefront errors, which can be caused by atmospheric turbulence, defects of the optical system such as imperfect mirror surfaces, and misalignments. The resulting speckles (diffracted starlight) in the search area can mask the planets. Wavefront correction is needed to mitigate the speckles. One important device for wavefront correction systems is deformable mirrors (DMs), which change the surface shape to compensate the wavefront errors. Our group at Princeton has made continuous contributions towards the research of wavefront sensing and control[38, 101, 102]. The layout of our coronagraph testbed is shown in Fig. 1.3

1.3.2 Starshades

One can also use a starshade, which is a large screen flying on a separate spacecraft positioned between the telescope and the star being observed, to suppress the starlight before it enters the telescope. The use of an occulting disc to detect exoplanets is first discussed by Lyman Spitzer at Princeton University in 1962[99]. Spitzer credited R. Danielson at Princeton for the idea in the paper. To diffract starlight, they suggested that the disk's transparency increases smoothly towards the edge. NASA later commissioned an investigation on the feasibility of an occulter mission based on this idea[112]. The concept of star-shaped external occulters is proposed by Christian Marchal in 1985[68]. The concept uses a circularly symmetric binary mask to achieve apodization. In 2006, Webster Cash at the University of Colorado

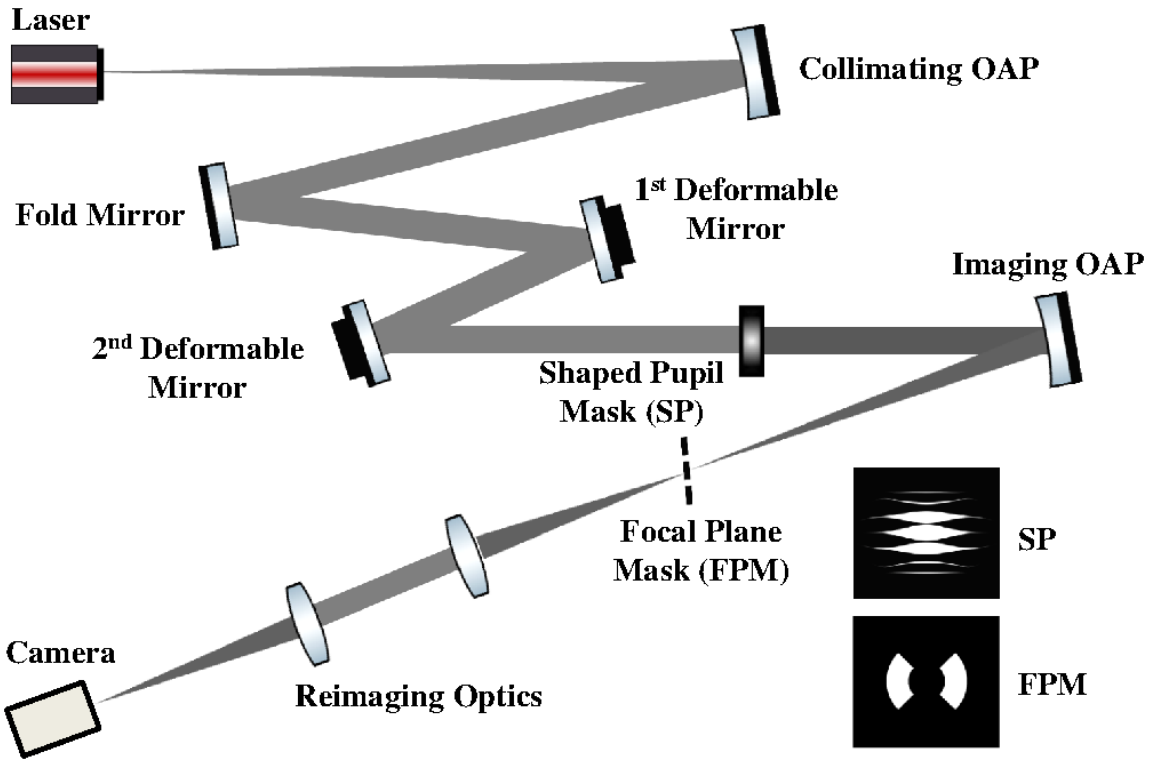

Figure 1.3: The layout of our Princeton High-contrast imaging lab (HCIL) coronagraph testbed[102].

introduced an apodization function[14], called an offset hypergaussian. It was the first to efficiently suppress diffraction by the 10 orders of magnitude needed to see an exo-Earth[40]. Robert Vanderbei at Princeton applied optimization techniques to generalize the design of the outer edge of an occulter reducing the size and achieving better performance[107]. The last two decades witnessed the growing interest in starshades and tremendous work on starshade technology advancement. Both analytical and experimental work have been carried out for various aspects of the starshade technology, such as error budgeting, optical modeling, experimental validation, deployment, edge scattering and formation flying [92, 9, 72, 94, 34, 13, 42, 61, 5, 41, 78]. Several starshade mission concepts have been investigated and new concepts are continuously being proposed [15, 57, 90, 82, 81].

1.3.3 Comparison

In many ways, coronagraphs and starshades are complementary. Coronagraphs are efficient for high-contrast surveys because it is easy to point the instrument to different targets. However, they have a low optical throughput and are very sensitive to wavefront perturbations. Even small aberrations introduce bright speckles, which influence the instrument's ability for exoplanet observations[102]. Thus, it imposes many challenging requirements on the telescope and instruments to design coronagraphs with $\sim 10^{-10}$ starlight suppression; two mission concepts under study are Habitable Exoplanet Observatory (HabEx) [82] and Large UV/Optical/Infrared Surveyor (LUVOIR) [81]. In comparison, starshades are good at deep imaging and spectroscopic characterization. As the starshade is outside of the telescope, there is less scattered light compared to using a coronagraph. Therefore, starshades are not sensitive to wavefront errors. This allows starshades to loosen the strict requirements, such as the polishing tolerances of the primary mirror, and to be designed to operate over a large bandpass. The total throughput is high since the starshade does not require any internal masking of the optical beam, which makes a starshade an excellent option for deep spectroscopy, especially at small inner working angles (IWA). Moreover, a starshade's IWA only depends on the size of the starshade and the distance between the starshade and telescope, rather than the telescope aperture. Its outer working angle is infinite. These are beneficial for exploring more areas in the habitable zone. Fig. 1.4 compares the performance of existing and future space high-contrast instruments in the context of known planets. As shown in the plot, no instruments can achieve the high contrast ($\sim 10^{-10}$) and small inner working angle (~ 0.1 arcsec) needed for detecting Earth-like planets. Fortunately, this region is accessible to starshades. Starshades' starlight suppression ability makes them an invaluable tool for exploring whether planets could harbor life. However, one disadvantage of a starshade is the time it takes to slew the starshade to realign it with different tar-

get stars. The starshade's ability to efficiently suppress the on-axis starlight while maintaining high throughput makes it an excellent tool for exploring the habitability of exoplanets. The Exoplanet Exploration Program's roadmap of NASA exoplanet missions is shown in Fig. 1.5. A recently studied potential mission is the Starshade Rendezvous Mission: a starshade that will work with the Nancy Grace Roman Space Telescope (previously called WFIRST)[90]. In the mission, the starshade is launched separately and rendezvous with the telescope in orbit. Starshades are also baselined for the HabEx mission concept[82]. LUVOIR also considers a starshade as a potential mission enhancement[81]. This work focuses on direct imaging with starshades.

1.4 Motivation

1.4.1 Simulation of Realistic Images for Starshade Missions

There are two reasons why we need to simulate realistic on-sky starshade images. First, it is impossible to have a full scale, ground-based starshade system test due to the large distance between a starshade and a telescope (tens of thousands of kilometers) and the large size of a starshade (tens of meters)[89]. Therefore, we must rely on sub-scale tests and modeling to predict the on-sky performance of a starshade. However, there is little dedicated research on the simulation of realistic images for starshade missions. After my work, Hildebrandt et al. released a starshade imaging simulation package called SISTER [47], which is similar to my work but also includes more factors like starglint from our Sun. By evaluating the simulated performance of a starshade with various errors, tolerance requirements like manufacturing and deployment tolerances, surface and edge reflectivity tolerances, transmission tolerances due to micrometeoroid damage, thermal fluctuations tolerances, and misalignment tolerances can be further validated[89]. Second, it is the first step to test image processing and detection methods for starshade images. Raw images contain speckles

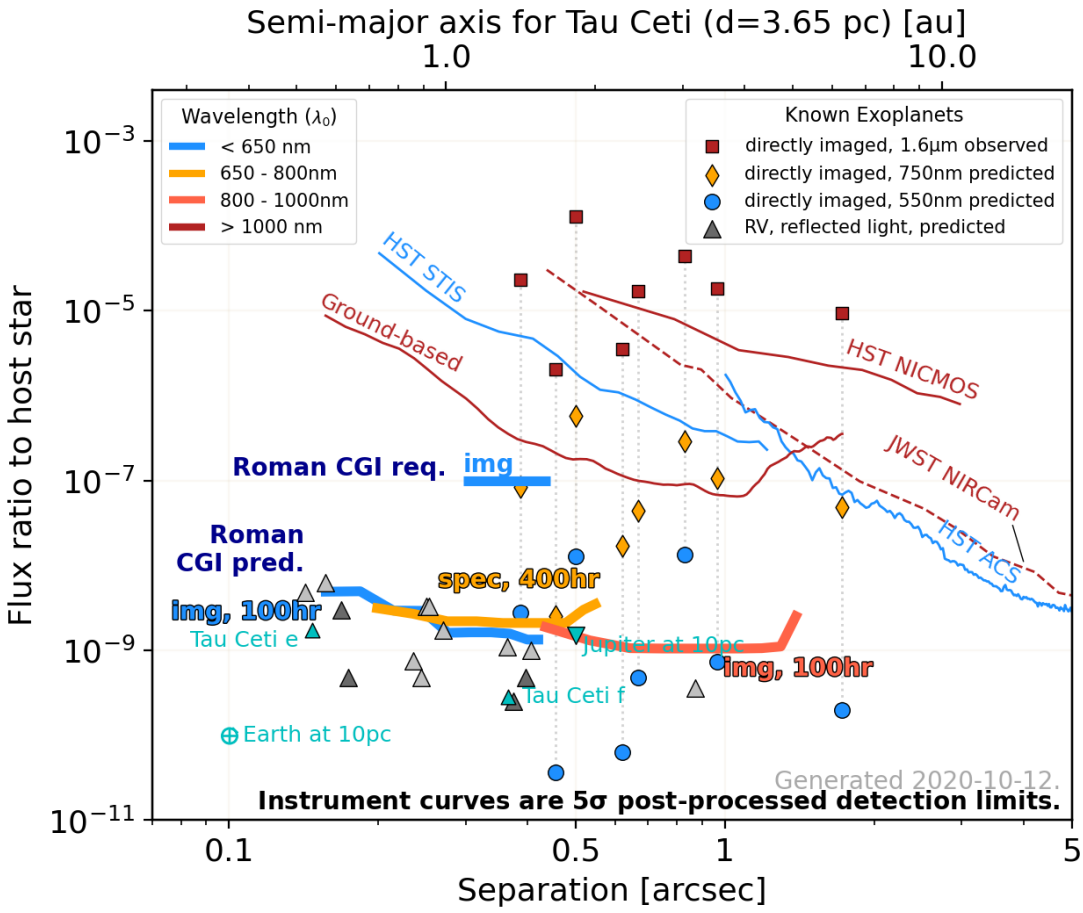

Figure 1.4: Direct imaging capabilities of current and future instrumentation. Only with starshades can we reach the small separation and low flux ratio required to see an Earth-like exoplanet. Figure created by Vanessa Bailey; Details can be found https://github.com/nasavbailey/DI-flux-ratio-plot.

that degrade the final image and make it difficult to identify planets. The first part of my project is devoted to the simulation of realistic Images for Starshade Missions.

1.4.2 Signal detection in starshade images

Due to the difference of the noise properties in coronagraphic images and starshade images, previous work on signal detection in coronagraphic images loses its utility on starshade images, which motivates the investigation of new techniques for starshade

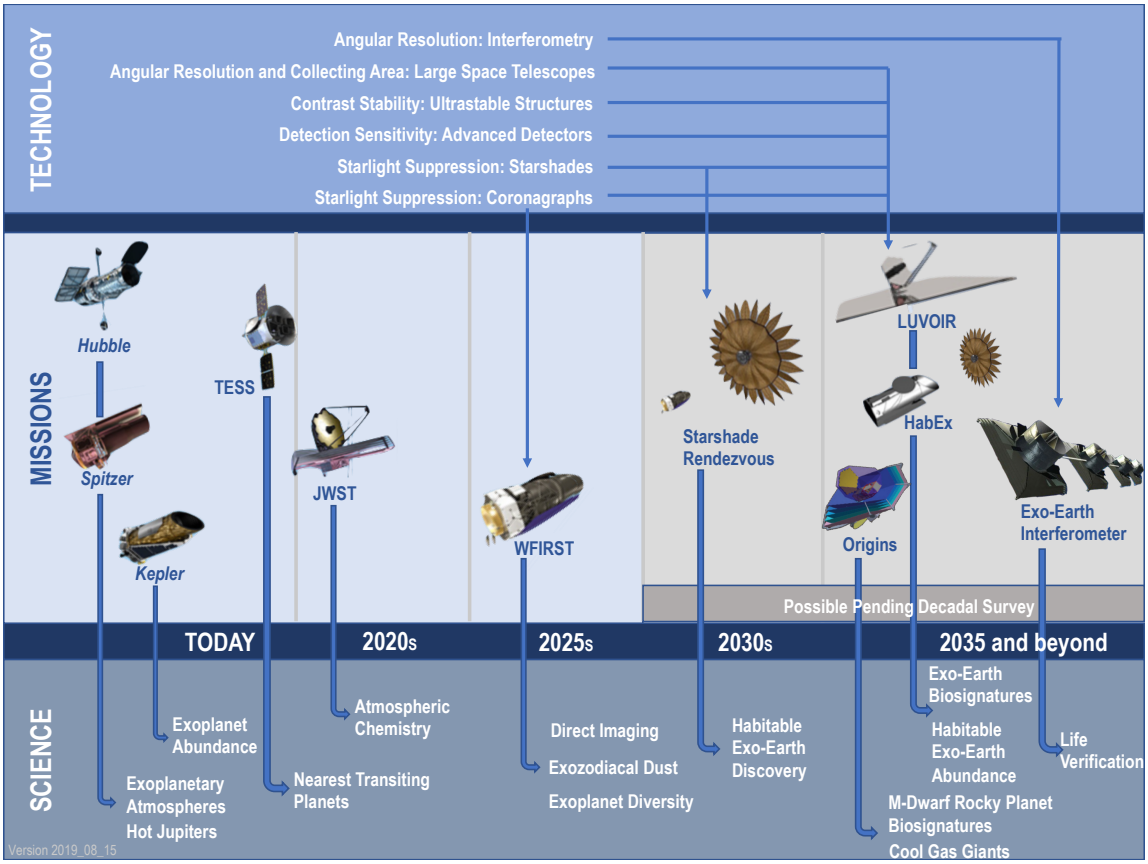

Figure 1.5: The Exoplanet Exploration Program's roadmap of NASA exoplanet missions (Image credit: NASA/JPL/Caltech)

images. In this thesis, I focus on the impact caused by errors in the starshade shape and exozodiacal dust and present an automatic detection algorithm, the generalized likelihood ratio test (GLRT), to provide robust detection on low-signal images in the presence of shape errors. I also introduce an iterative process to detect a planet in the presence of significant exozodiacal dust. This work focuses on signal detection without the need for post-processing (e.g., PSF subtraction). Post-processing may improve the detection performance but could also complicate the data analysis process and risks introducing artifacts into or removing part of the planetary signal. I believe demonstrating our signal detection method on unprocessed images strengthens the argument for the efficiency of our method. Detailed investigation on post-processing is saved for future work.

Another motivation for the investigation of signal detection in starshade images is for its special imaging mode. A starshade or internal coronagraph can suppress the starlight and leave only the planet's light to be detected, however, the planets are extremely faint, and detecting them is still a challenge. An Earth-like planet ranges from 28^{th} to 30^{th} magnitude or fainter. As a result, the signal can be smaller than the camera read noise. An Electron Multiplying Charged Coupled Device (EMCCD) can alleviate this problem by amplifying the signal in an electron-multiplication (EM) register, thus reducing the effective readout noise to less than one electron[48]. Unfortunately, at the same time, a new noise is introduced — the multiplicative noise from the amplification process. This can be overcome by operating in photon counting (PC) mode. PC Mode reports a value of 1 or 0 in each pixel for each integration time by thresholding the value at the final stage. The value reported in the pixel is one if the number of electrons in a pixel is bigger than a chosen threshold and zero otherwise. The binary value only indicates the existence of photons in the pixels during the integration time but does not reveal the exact number of those photons, so the exposure time needs to be chosen such that the expected photon count in any pixel is much less than one[71]. Examples of simulated PC images are shown in Fig. 3.12 (all the simulations mentioned in this work use a 1 second integration time) and the details about how the images are simulated can be found in Ref. 51 and Chapter 3. The operation of an EMCCD in photon counting mode is fairly new and thus still developing. Available literature on the design and characteristics of EMCCD detectors can be found in Refs. 26, 28, 67, 23, 109, 39, 80, 48. A toolkit for starshade image simulation has been published recently[47].

Previous work on image processing for PC images focuses mainly on image stacking and Bayesian estimation methods[65, 43], which are applied to co-added PC images rather than designed for individual PC images[36, 96]. However, all these methods do not provide theoretical guidance on how to choose the integration times and the total

number of PC images to combine into one co-added image. In my work, at the first attempt, I also presented an alternative methodology for co-added PC images[50] which can efficiently detect even weak signals automatically and give guidance for choosing the optimal number of PC images for a co-added image. For further improvement, I utilize a statistical model for the EMCCD to obtain a relationship between the detection probability and the photon rate. I use this distribution to formulate a Bernoulli distribution for the values of the same pixel on different PC images. Then, sequential detection and estimation are performed. Consequently, detection and accurate intensity estimation can be achieved within hundreds of seconds.

1.5 Dissertation organization

I begin this thesis with the review of the theory of diffraction and how starshades work in Chapter 2. In Chapter 3, I describe the image simulation process. It is used to generate the test set for my planet detection methods. Chapter 4 presents the GLRT detection method and represents the bulk of this work. First, I introduce the method for the co-added images[50, 52]. Then, an iterative approach of GLRT is presented to tackle the problem of exozodiacal dust. I also introduce the Bernoulli GLRT to directly work on PC images, which utilizes a statistical model for the EMCCD and is the most efficient. The Bernoulli GLRT is first introduced in our work Ref. 54, where the method is called the Sequential Generalized Likelihood Ratio Test. We change the method name to Bernoulli Generalized Likelihood Ratio Test to better reflect that the improvement of performance is from the usage of an accurate model based on the Bernoulli distribution for the detector [53]. I provide application examples and comparisons of the performance of different methods. I end by summarizing my work and outline future directions.

Chapter 2

Starshade Theory

2.1 Diffraction theory

2.1.1 Introduction to Diffraction

Diffraction is "any deviation of light rays from rectilinear paths which cannot be interpreted as reflection or refraction"[95]. It is caused by "the confinement of the lateral extent of a wave and is most appreciable when that confinement is to sizes comparable with a wavelength of the radiation being used"[37]. Diffraction theory plays a vital role in various fields in physics and engineering. It is also the foundation for my work.

The history of the development of diffraction theory is fascinating. Francesco Maria Grimaldi is the first to accurately report on the diffraction phenomenon and published the observation in 1665. The first explanation for the phenomenon is the wave theory of light by Christian Huygens in 1678. However, the further development of the theory was hampered by the famous scientist Isaac Newton, who believed in the corpuscular theory of light, partly because of his great prestige[3]. Not until Thomas Young supported the wave theory of light by the demonstration of interference did further development resume. In 1818, Augustin Jean Fresnel combined Huygens's

principle of secondary waves and Young's principle of interference, and calculated the interference patterns. Fresnel's work entered a competition sponsored by the French Academy of Sciences in 1818, one of whose committee is Siméon-Denis Poisson. Poisson was a supporter of the particle theory. He questioned Fresnel's model and pointed out that the model predicted an "absurd" result: a bright spot at the center of the shadow of a circular opaque obstacle. However, Dominique-François-Jean Arago, the head of the committee, decided to perform such an experiment, and successfully observed the predicted spot, which is known as "Poisson's spot" or the "spot of Arago" after that. The next great progress on further understanding diffraction is made by James Clerk Maxwell. He described light as a propagating electromagnetic wave. Gustav Robert Kirchhoff deduced the form of amplitude and phase from the wave equation in 1882. The inconsistency in Kirchhoff's boundary conditions was pointed out by Henri Poincaré in 1892 and Arnold Sommerfeld in 1894. Sommerfeld removed one of the boundary assumptions in Kirchhoff's theory in 1896. One defect of Kirchhoff's and Sommerfeld's theories was their scalar formulation. Friedrich Kottler obtained the first satisfactory vectorial diffraction theory in 1923.

In this section, I briefly review the basics of diffraction theory and emphasize the scalar diffraction theory, which describes the optical model of starshades. The main reference used for this section is Goodman's "Introduction of Fourier Optics"[37].

2.1.2 Scalar diffraction theory

The most fundamental analysis should be based on Maxwell's equations. They rigorously keep track of the electric and magnetic fields everywhere. They are accurate and universally applicable but are challenging for common calculations. In some cases, it is possible to make approximations to simplify the theory. For example, when the diffracting structures have much larger physical dimensions than the wavelength and the diffracting fields are not observed too close to the aperture, the scalar theory of

diffraction introduces substantial gain of simplicity with little loss of accuracy. This is precisely the case for this work. Therefore, the scalar theory of diffraction rather than the vector theory is used.

The scalar diffraction theory assumes that the light field can be adequately represented by a complex scalar potential. Let the light disturbance at position $\boldsymbol{P}$ and time t be the scalar function $u(\boldsymbol{P}, t)$. For a monochromatic wave, the scalar field can be rewritten in a compact form by using complex notation:

$$u(\boldsymbol{P}, t) = Re\{U(\boldsymbol{P})exp(-j2\pi\nu t)\}, \tag{2.1}$$

where $Re\cdot$ means "the real part of"; ν is the optical frequency; $U(\boldsymbol{P})$ is the complex scalar potential and must obey the time independent equation:

$$(\nabla^2 + k^2)U = 0, \tag{2.2}$$

where $k = \frac{2\pi}{\lambda}$ is the wave number and λ is the wavelength. This is known as the Helmholtz equation.

Consider the point $\boldsymbol{P}$ is in a closed surface S. Using Green's theorem, we can derive the result:

$$U(\boldsymbol{P}) = \frac{1}{4\pi}\iint_S \left(G\frac{\partial U}{\partial \boldsymbol{n}} - U\frac{\partial G}{\partial \boldsymbol{n}}\right) ds, \tag{2.3}$$

where G is an auxiliary function that also satisfies Eq. 2.2, and $\frac{\partial}{\partial \boldsymbol{n}}$ denotes a partial derivative in the outward normal direction at each point on surface S.

Consider a specific closed surface S consisting of two parts as shown in Fig. 2.1: a plane surface S_1 behind a diffracting screen and a spherical cap S_2. Choose

$$G = \frac{exp(jkr)}{r}. \tag{2.4}$$

It is a unit-amplitude spherical wave originated from point $\boldsymbol{P}$. Thus, on S_2, $G = \frac{exp(jkR)}{R}$, and for large R, $\frac{\partial G}{\partial \boldsymbol{n}} \approx jkG$. Therefore,

$$\begin{aligned} \iint_{S_2} \left[G\frac{\partial U}{\partial \boldsymbol{n}} - U\frac{\partial G}{\partial \boldsymbol{n}} \right] ds &\approx \iint_{S_2} \left[G\frac{\partial U}{\partial \boldsymbol{n}} - U(jkG) \right] ds \\ &= \int_{\Omega} G\left(\frac{\partial U}{\partial \boldsymbol{n}} - jkU \right) R^2 d\omega, \end{aligned} \tag{2.5}$$

where Ω is the solid angle subtended by S_2 at $\boldsymbol{P}$. As the disturbances U illuminating the aperture will be a linear combination of spherical waves, the disturbance U will satisfy

$$\lim_{R\to\infty} R\left(\frac{\partial U}{\partial \boldsymbol{n}} - jkU \right) = 0. \tag{2.6}$$

Moreover, $|RG| = |exp(jkR)| \leq 1$. Thus, the integration over S_2 as shown in Eq. 2.5 can be neglected. This requirement is known as the Sommerfeld radiation condition. Moreover, as R goes to infinity, the screen extends to infinity too. Therefore, Equation. 2.3 becomes

$$\begin{aligned} U(\boldsymbol{P}) &= \frac{1}{4\pi} \iint_{S_1} \left(G\frac{\partial U}{\partial \boldsymbol{n}} - U\frac{\partial G}{\partial \boldsymbol{n}} \right) ds \\ &\approx \frac{1}{4\pi} \iint_{\Sigma} \left(G\frac{\partial U}{\partial \boldsymbol{n}} - U\frac{\partial G}{\partial \boldsymbol{n}} \right) ds, \end{aligned} \tag{2.7}$$

where the last approximation is valid under the assumptions that: U and its derivative $\frac{\partial U}{\partial \boldsymbol{n}}$ are zero behind the opaque screen; U and its derivative $\frac{\partial U}{\partial \boldsymbol{n}}$ across Σ are the same as they would be without the screen. These conditions are known as the Kirchhoff boundary conditions.

Now consider that the Green's function G is modified to:

$$G_{-}(\boldsymbol{P_1}) = \frac{exp(jkr)}{r} - \frac{exp(jkr_1)}{r_1}, \tag{2.8}$$

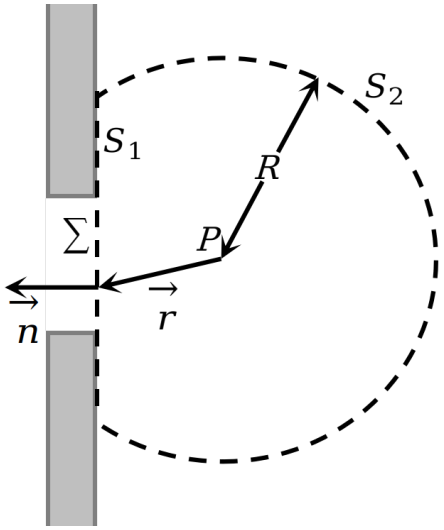

Figure 2.1: Diagram of the closed surface chosen for diffraction by a plane screen

where the later term added is a unit-amplitude spherical wave originating from point $\boldsymbol{P_2}$, which is the mirror image of point $\boldsymbol{P}$ on the other side of the screen, as shown in Fig. 2.2. The previous analysis remains valid after this modification. G_- is now zero on the aperture Σ. Therefore,

$$U(\boldsymbol{P}) = \frac{-1}{4\pi} \iint_{\Sigma} U \frac{\partial G_-}{\partial \boldsymbol{n}} ds, \tag{2.9}$$

This is the first Rayleigh-Sommerfeld solution. On the aperture Σ,

$$\begin{aligned} \frac{\partial G_-(\boldsymbol{P_1})}{\partial \boldsymbol{n}} &= cos(\boldsymbol{n}, \boldsymbol{r}) \left(jk - \frac{1}{r} \right) \frac{exp(jkr)}{r} - cos(\boldsymbol{n}, \boldsymbol{r_1}) \left(jk - \frac{1}{r_1} \right) \frac{exp(jkr_1}{r_1} \\ &= 2cos(\boldsymbol{n}, \boldsymbol{r}) \left(jk - \frac{1}{r} \right) \frac{exp(jkr)}{r} \\ &\approx 2jkcos(\boldsymbol{n}, \boldsymbol{r}) \frac{exp(jkr)}{r} \\ &= 2\frac{\partial G(\boldsymbol{P_1})}{\partial \boldsymbol{n}}, \end{aligned} \tag{2.10}$$

where the approximation is valid when $r \gg \lambda$. Thus, Eq. 2.9 can be written as

$$U(\boldsymbol{P}) = \frac{-1}{2\pi} \iint_{\Sigma} U \frac{\partial G}{\partial \boldsymbol{n}} ds. \tag{2.11}$$

As the wave number k equals $\frac{2\pi}{\lambda}$, the resulting formula would be:

$$U(\boldsymbol{P}) = \frac{1}{j\lambda}\iint_{\Sigma} U(\boldsymbol{P_1})\frac{exp(jkr)}{r}cos(\boldsymbol{n},\boldsymbol{r})ds. \tag{2.12}$$

It expresses that the observed field at $\boldsymbol{P}$ is the combination of diverging spherical waves originating from each point $\boldsymbol{P_1}$ in the aperture Σ. This is known as the Huygens-Fresnel principle.

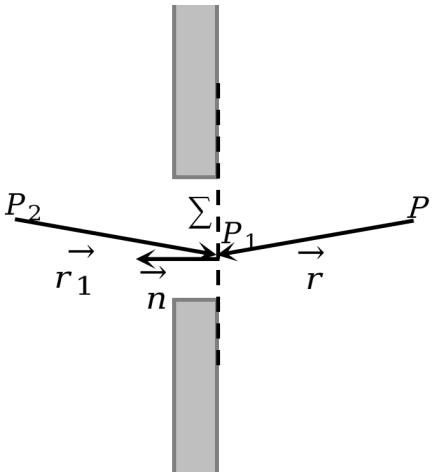

Figure 2.2: Point source illumination of a plane screen

2.1.3 Fresnel Diffraction

Now consider the Huygens-Fresnel principle in rectangular coordinates as shown in Fig. 2.3. Thus,

$$\begin{aligned} r &= z\sqrt{1+\left(\frac{x-\xi}{z}\right)^2+\left(\frac{y-\eta}{z}\right)^2} \\ &\approx z\left[1+\frac{1}{2}\left(\frac{x-\xi}{z}\right)^2+\frac{1}{2}\left(\frac{y-\eta}{z}\right)^2\right], \end{aligned} \tag{2.13}$$

where the last approximation is valid when $\left(\frac{x-\xi}{z}\right)$ and $\left(\frac{y-\eta}{z}\right)$ are reasonably small. The resulting expression for Eq. 2.12 is:

$$\begin{aligned} U(x,y) &= \frac{exp(jkz)}{j\lambda z}\iint_{\Sigma} U(\xi,\eta)exp\left\{j\frac{k}{2z}[(x-\xi)^2+(y-\eta)^2]\right\}d\xi d\eta \\ &= \frac{exp(jkz)}{j\lambda z}e^{j\frac{k}{2z}(x^2+y^2)}\iint_{\Sigma}\left\{U(\xi,\eta)e^{j\frac{k}{2z}(\xi^2+\eta)^2}\right\}e^{j\frac{k}{2z}(x\xi+y\eta)}d\xi d\eta, \end{aligned} \tag{2.14}$$

which is known as the Fresnel diffraction integral. The later expression is in the form of a Fourier transform(FT).

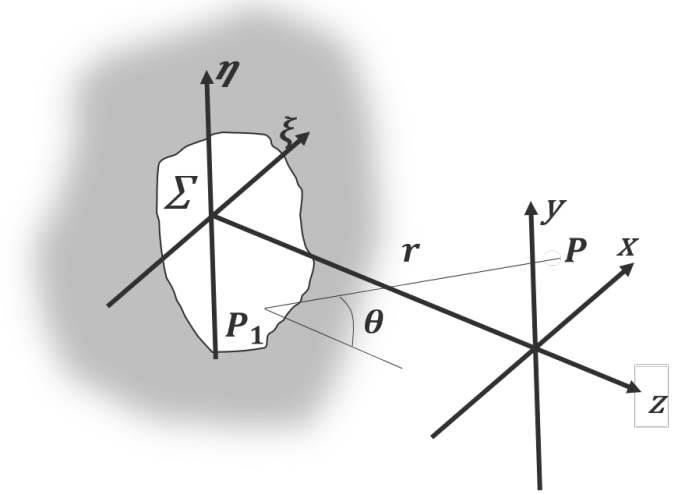

Figure 2.3: Diffraction geometry

2.1.4 Babinet's principle

In the preceding section, the diffraction formula over an aperture on a screen with infinite size was presented. In the case of starshades, there is a screen with finite size in the infinite open space, which may pose a problem for the calculation. Fortunately, Babinet's principle resolves this issue.

The principle states that, if the union of a screen with an opening Σ (as shown in Fig. 2.3) and a obstruction Σ_1 (as shown in Fig. 2.4) is a completely obstructing

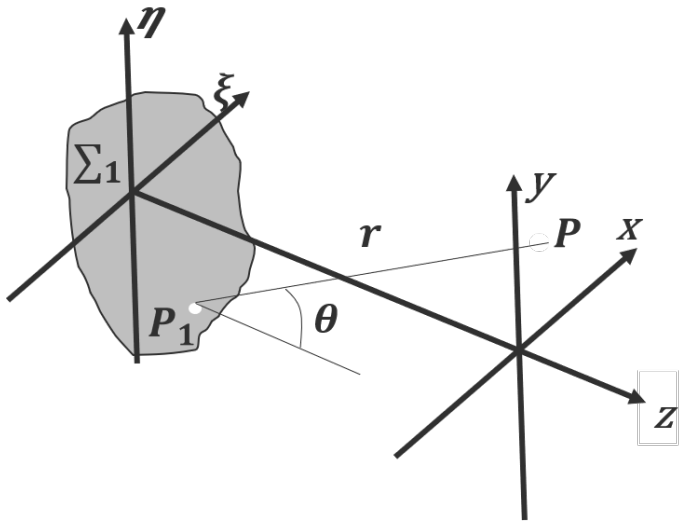

Figure 2.4: A complementary screen of the aperture in Fig. 2.3

surface, the sum of the field behind Σ and the field behind Σ_1 is equal to the field where there is no screen. That is:

$$U_{free} = U_{\Sigma} + U_{\Sigma_1}. \tag{2.15}$$

Thus,

$$U_{\Sigma_1} = U_{free} - U_{\Sigma}. \tag{2.16}$$

This is helpful to calculate the diffraction of starshades.

2.2 Theory of Starshades

We review how starshades work briefly in this section. More details about starshade theory and design can be found in [107, 93, 8, 40].

Our goal is to suppress the on-axis light from the bright star with an external occulter. Armed with the diffraction theory from Sec. 2.1, it is easy to find out that a circular opaque occulter does not suppress on-axis light due to diffraction. One design

idea is a mask with slowly increasing transmission along the radius. It is typical to design the occulter circularly symmetric, so the Fresnel integral reduces to a one-dimensional model along the radius, which is more numerically tractable. We can design how the transmission changes with the radius, i.e., the apodization function, to achieve the required level of light suppression. It is challenging to accurately make a variable transmission mask, so we can approximate the apodized occulter using a petalized binary occulter, i.e., starshades.

The value of an apodization function $A(r)$ is the corresponding opacity at radius r and can also be interpreted as the corresponding area ratio covered by the starshade along that radius. An example is shown in Fig. 2.5(a). Its corresponding apodized occulter is shown in Fig. 2.5(b). $A(r)$ in the form of a polynomial function[19] and the form of a hypergaussian [14] is proposed to achieve required performance. Our group solves for $A(r)$ by minimizing the area under the apodization function subject to the constrain of achieving the required suppression level[107]. A 2-dimensional binary starshade S can be generated from $A(r)$, using the equations[105]:

$$\begin{aligned} S &= \{(r,\theta), 0 \le r \le R, \theta \in \Theta\}, \\ \Theta(r) &= \bigcup_{n=0}^{N-1} \left[\frac{2\pi n}{N} - \frac{\pi}{N} A(r), \frac{2\pi n}{N} + \frac{\pi}{N} A(r) \right], \end{aligned} \tag{2.17}$$

where S is the set of points in polar coordinates in the starshade; $\Theta(r)$ is the set of corresponding angles for a radius r; N is the starshade's total number of petals; and n is the number of the petal that the set is defining. The resulting starshade is shown in Fig. 2.5(c).

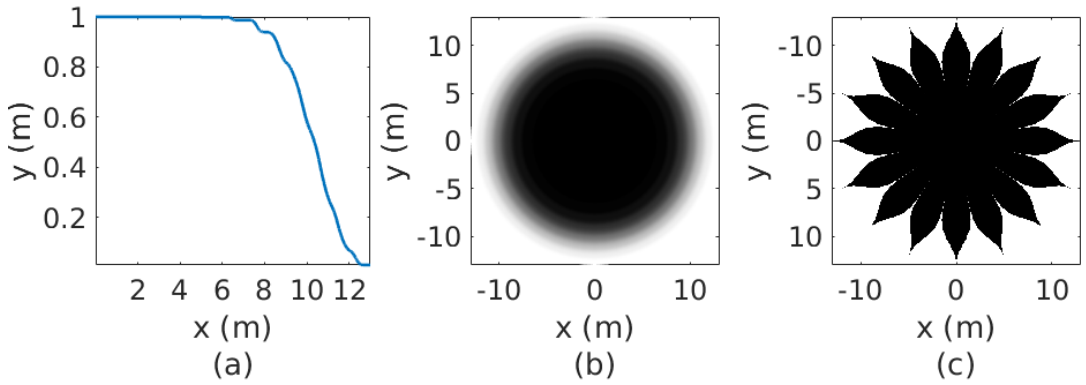

Figure 2.5: Starshade design (a) The apodization function. (b) The apodized occulter. (c) The binary occulter, i.e., the starshade. It is the one that I use in this work, which is 13 meters in radius and has 16 petals and designed for the Starshade Rendezvous Mission[90].

Chapter 3

Realistic starshade image simulation

In this chapter, I describe the process of simulating images from a starshade observation, which involves calculating the propagation of the astronomical scene through the starshade system to the telescope's image plane and then passing through the detector. Figure 3.1 shows the detailed process for simulating Starshade images, which incorporates the main factors that influence the image of a realistic starshade observation. In the simulation, a binary matrix represents the starshade outline and defects are added to the shape by adjusting this matrix; the alignment between the starshade and telescope is accounted for by adding time-dependent formation flying dynamics to the diffraction calculation; and a detector model[48] for the Roman Telescope is used, which includes a clock-induced charge, dark current, degradation during a lifetime, polarization losses, and read noise. Wavefront errors are inevitable for optical systems. By inlcuding Zernike modes at the pupil plane, the effect can be accounted in the simulation. However, they do not introduce noticeable changes in starshade images[51]. It is also easy to include misalignment is between the star, the starshade and the telescope in the simulation by change the coordinates in the corresponding

integrals. The effect on images is negligible if the misalignment within meters. In this thesis, I will not further elaborate on these two factors.

Section 3.1 starts this chapter with an explanation of how to calculate the resultant diffraction of light from a point source propagating past a starshade. Then, in Sec. 3.2, I introduce the input astronomical scene used for the simulation. I follow it with the description of the efficient method to calculate the result from a whole input astronomical scene in Sec. 3.3. After these sections of image simulation for the most basic case, I extend to cases with starshade errors in Sec. 3.4. In Sec. 3.5, the final step for realistic image generation is introduced: using the detector model to add various sources of noise. At last, I provide some examples of the simulated images. Unless otherwise stated, the starshade used in this thesis is the designed for the Roman Space Telescope and is 13 meters in radius and has 16 petals, shown in Fig. 2.5.

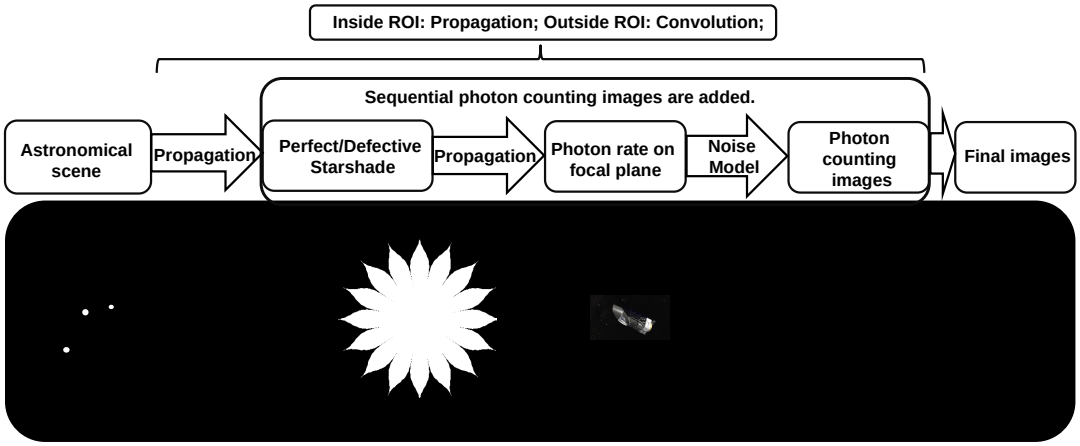

Figure 3.1: Diagram of the image simulation process with starshade system illustration(not drawn to scale). The illustration, i.e., light sources, a starshade, and a telescope, on the bottom is aligned with the description above. Region of influence (ROI) is the area defined at the simulation input, i.e., the astronomical scene, beyond which the incoming light is considered a plane wave and is not diffracted by the starshade.

3.1 Propagation through the starshade model

The propagation process contains four planes and two calculations, as shown in Fig. 3.2. P0 is the astronomical scene plane; P1 the starshade plane; P2 the pupil plane; P3 the image plane. As our starshade imaging system is very far away from the light sources, the light from a point source can be taken as a plane wave when it reaches the starshade plane P1. Additionally, we can treat off-axis light sources as plane waves with corresponding incident angles. The propagation from P1 to P2 can be calculated from the Fresnel diffraction equation. The electric field at P2 is given by

$$E(x,y;x_0,y_0) = \frac{e^{\frac{2j\pi z}{\lambda}} e^{\frac{j\pi(x^2+y^2)}{\lambda z}}}{j\lambda z} \iint_{-\infty}^{+\infty} \dots$$
$$\dots [e^{\frac{j2\pi x_s sin(\theta) sin(\alpha) + y_s sin(\theta) cos(\alpha)}{\lambda}} A_s(x_s,y_s)] e^{\frac{j\pi(x_s^2+y_s^2)}{\lambda z}} e^{-\frac{j2\pi(xx_s+yy_s)}{\lambda z}} dx_s dy_s, \quad (3.1)$$

where (x_0, y_0), (x_s, y_s) , (x, y) , are coordinates in planes P0, P1 and P2 respectively; z is the distance between planes P1 and P2; θ and α are the incident angles in plane P1 along the x- and y-axes, respectively; and $A_s(x_s, y_s)$ is the 2-D transmission profile of the starshade. The incident angles should satisfy $sin^2(\theta) + sin^2(\alpha) \leq 1$, and each value in the matrix $A_s(x_s, y_s)$ is between zero and one. Values of the pixels inside the boundary of the starshade equal zero, which means 'opaque'. Values of the pixels outside the starshade equal one, which means 'open space'. When the boundary line of the starshade falls in one pixel, one part of the pixel is outside the starshade and the other part is inside. And the value in that pixel is the area ratio of the pixel outside the starshade relative to inside.

As the focus of the telescope is set on light sources at infinity, the quadratic phase term introduced by the lens will cancel out the quadratic phase term in the Fresnel

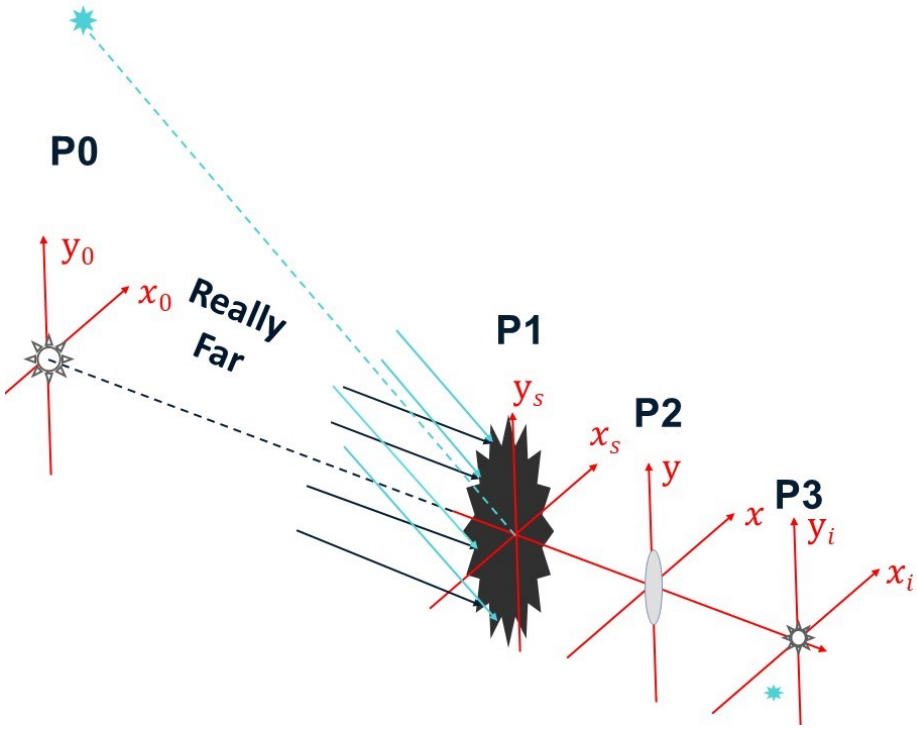

Figure 3.2: Diagram of the propagation. As our imaging system is very far away (around 10 pc) from the light sources, we can consider light from off-axis light sources as plane waves with corresponding incident angles. P0 is the astronomical scene plane; P1 the starshade plane; P2 the pupil plane; P3 the image plane.

diffraction equation from P2 to P3. Therefore, the electric field at P3 is given by

$$E_i(x_i, y_i; x_0, y_0) = \frac{e^{\frac{2j\pi f}{\lambda}} e^{\frac{j\pi(x_i^2+y_i^2)}{\lambda f}}}{j\lambda f} \iint_{-\infty}^{+\infty} [E(x, y; x_0, y_0)P(x, y)] e^{-\frac{j2\pi(xx_i+yy_i)}{\lambda f}} dxdy, \tag{3.2}$$

where (x_i, y_i) is the coordinate in plane P3, $P(x, y)$ is 1 inside the aperture and 0 otherwise; f is the distance between the two planes and also the focal length. The diffraction integrals in this work are calculated via Matrix Fourier Transforms[97]. The result of these calculation is the noiseless image arriving on the detector. The pixel size on the detector (image plane) is 0.021 arcsec/pixel, however, the calculations are performed at 0.003 arcsec/pixel and then combined into 0.021 arcsec/pixel to replicate the detector pixel size.

3.2 Input astronomical scene

The input for the image generation process is a discretized astrophysical scene of our solar system (0.0300000 AU per pixel) as viewed face-on from 10 pc away developed as part of the Haystacks Project[86]. The Haystacks models contain two state-of-the-art models of the solar system with high-fidelity spatial and spectral information of complete planetary systems including star, planets, interplanetary dust, and astrophysical background sources such as galaxies and Milky way stars. One model is for the solar system in the Archean Eon 3.5 billion years ago and the other is for the present day; we use the present day model.

The Haystacks model contains multi-wavelength image slices, covering the range from 0.3 μm to 2.5 μm. Each image centers on the star. The star and planets are set at the proper locations, represented as single-pixel sources. The pixel values in the image slices are spectral flux densities in units of Jy. The pixel size is 0.1AU × 0.1AU. Figure 3.3(a) shows a single image slice at a wavelength of $\lambda = 0.55$ μm at perfect resolution. To see the details of the image, I have reduced the dynamic range by reducing the stellar flux in Fig. 3.3. To more clearly demonstrate the detection problem in the latter part of the thesis, I will mostly zoom in to show the center star and planets around it, as shown in Fig. 3.3(b).

3.3 Simplified propagation for off-axis sources

The optical model to calculate the starshade diffraction uses Fresnel diffraction theory[93] to propagate light past the starshade. The derivation of Fresnel propagation for my application has been introduced in Chapter 2. However, calculating the propagation of each pixel separately in Haystacks is computationally expensive. To solve this problem, we first need to investigate the system's response for light sources at different angular separations from the starshade. To better demonstrate

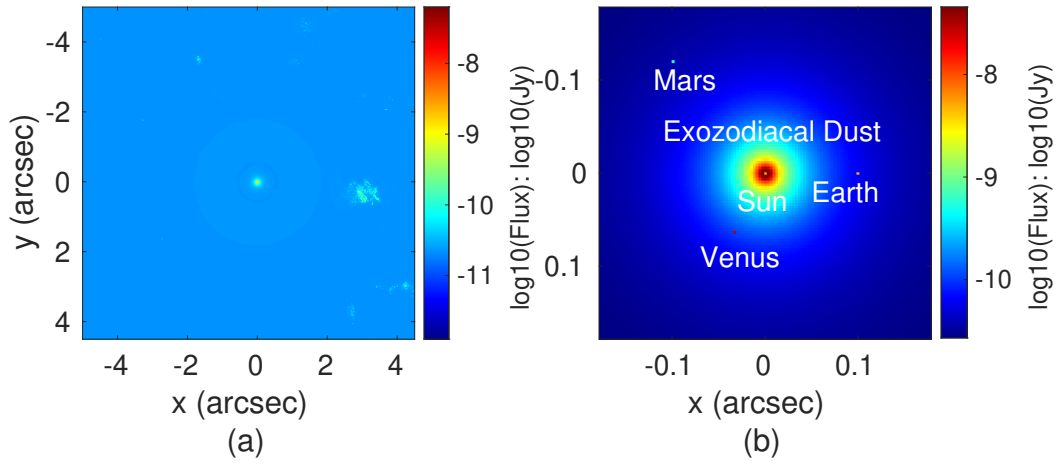

Figure 3.3: Input astronomical scene from Haystacks[86]. (a) The present solar system as viewed from 10 pc − at $\lambda = 0.55$ μm in logarithmic scale flux (the central star is made 10^{10} times dimmer to reveal fainter features). (b) The zoomed-in view of the image in (a).The star and planets are represented as single-pixel sources. The bright areas around the center are interplanetary dust.

the difference in the system's response, i.e., PSFs, the illustrations in this chapter use 0.003 arcsec as the pixel size.

The PSF without a starshade is shown in Fig. 3.4(a). Fig. 3.4(b)-(f) shows examples of PSFs where the light source has moved from on-axis to off-axis with the starshade and telescope. As the light source moves away from the alignment, the peak of the PSF shifts and the PSF brightens until it settles to the constant free-space value. Meanwhile, the shape of the PSF first becomes asymmetrical and later symmetrical again. It is noticeable that the PSF in Fig. 3.4(e) and (f) is similar to the one without the starshade as shown in Fig. 3.4(a). Fig. 3.5 compares the cross-sections of the PSFs along the center axis with and without a starshade from Fig. 3.4. As the light source moves away from the alignment, the PSF becomes similar to the one without the starshade. Fig. 3.6 demonstrates how the maximum value in the PSF changes with the light source's position. It agrees with the observation above that the PSF becomes brighter at first and then has little change when it is similar to that

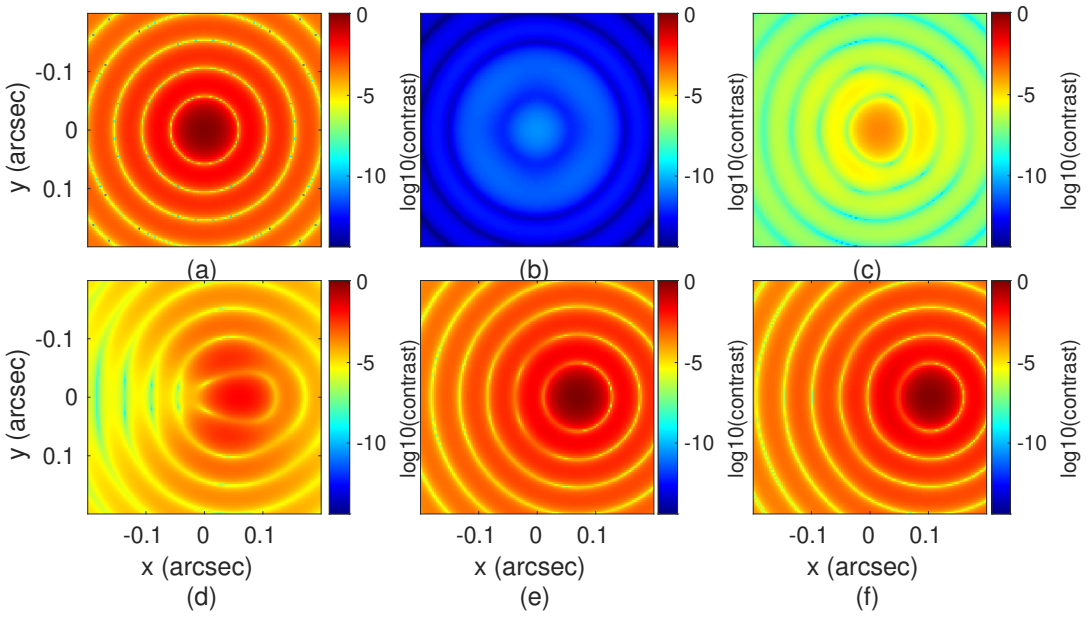

Figure 3.4: PSFs of light sources with different positions relative to aligned starshades and telescope. The color map is in a logarithmic scale. The intensity is normalized by the maximum intensity of the PSF without starshade, which is actually the contrast. (a). The PSF for the system without starshades. (b). The light source is aligned with starshade and telescope at: (b) 0 arcsec, (c) 0.018 arcsec, (d) 0.042 arcsec, (e) 0.072 arcsec, and (f) 0.102 arcsec. As the light source moves out of alignment, the PSF becomes brighter and then becomes constant. Meanwhile, the shape of the PSF first becomes asymmetrical and later symmetrical again. It is noticeable that the PSF in (e) and (f) is similar to the one without the starshade as shown in (a).

of the PSF without starshades. Finally, Fig. 3.7 validates how similar the shape of the PSFs are. I shift the off-axis PSFs with the starshade to the center by the length of its corresponding light source's misalignment. The two lines overlap very well in Fig. 3.7 (b), meaning PSFs are the same. As the plot is in a log scale, the main light spot is much brighter than all other locations. Thus, I consider that the two PSFs are the same if the main spots are the same. The starshade stops having an effect at roughly 0.09 arcsec for $\lambda = 0.55$ μm.

The above discussion shows that starshades have a noticeable influence on light propagation only for a small area in close proximity to the starshade, which I call the

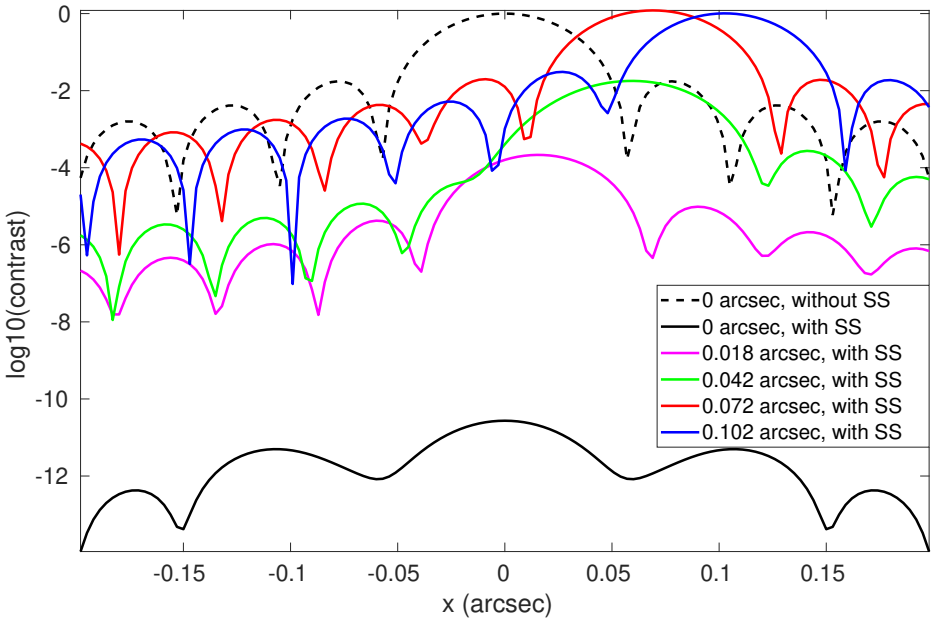

Figure 3.5: The cross-sections of the PSFs of light sources with different positions relative to aligned starshades and telescope, as shown in Fig. 3.4. As the light source moves away from the alignment, the PSF becomes similar to the one without the starshade. As I calculate one result every 0.003 arcsec, the curves are piece-wise linear rather than smooth.

region of influence (ROI). The ROI is defined at the input plane of the simulation and is the angular separation of a source, beyond which the incoming light is considered a plane wave and is not diffracted by the starshade. When the light source is outside the ROI, we can neglect the effect of the starshade. Furthermore, when the PSFs for sources are outside the ROI, the shifted on-axis PSF without a starshade is a good approximation for them, as shown in Fig. 3.7. Therefore, outside the ROI, we can approximate the system as a linear invariant system and thus use a convolution. The convolution is proved for similar cases in some textbooks [37]. Thus, I only use Fresnel propagation inside the ROI and simply convolve point sources outside the ROI with the telescope PSF without starshades.

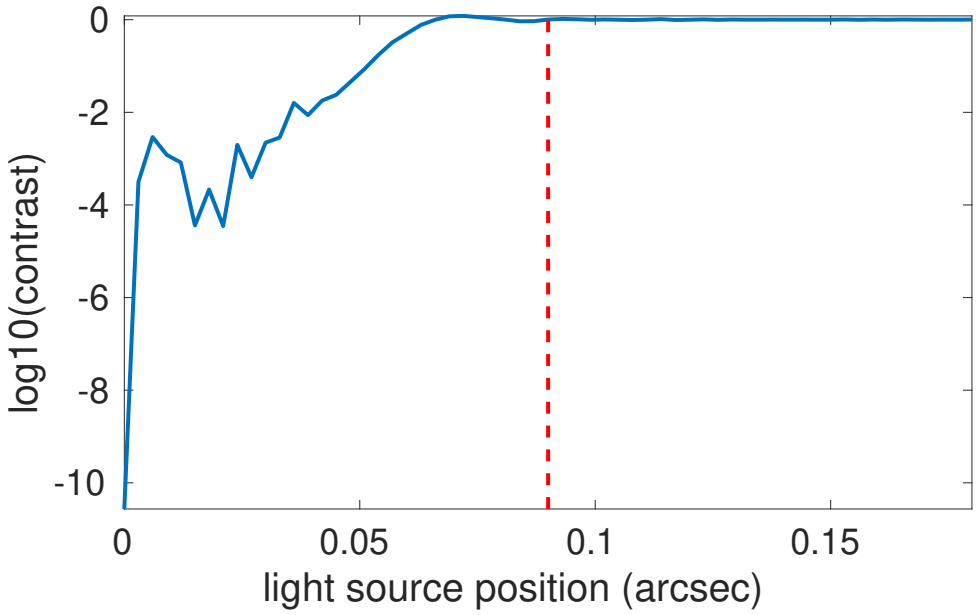

Figure 3.6: The maximum of the PSFs of light sources with different positions relative to aligned starshades and telescope. As I calculate one result every 0.003 arcsec, the curves are piece-wise linear rather than smooth.

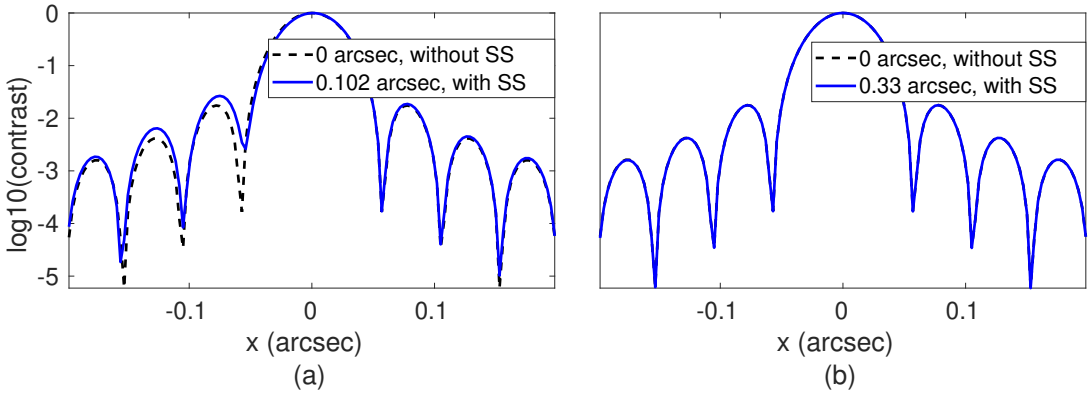

Figure 3.7: Comparison of the PSF without a starshade and the PSFs of light sources with different positions relative to aligned the starshade and telescope. The PSFs with the starshade are shifted to the center by the length of its corresponding light source's misalignment. (a) The light source is off-axis by 0.102 arcsec. (b) The light source is off-axis by 0.330 arcsec. The two lines overlap very well, meaning PSFs are the same.

3.4 Starshade errors

Accurately shaping the starshade is the key to achieving high contrast. Starshades are designed to let the right amount of light get through to destructively interfere such that the on-axis electric field is close to zero. In reality, the starshade's shape may not be the same as designed during the mission. There are several potential causes: a perfect starshade is challenging to manufacture; the starshade bends because of thermal effects or vibrations; micrometeorites damage the starshade. For example, truncated tips can occur during manufacturing and a petal clocked from its nominal position is possible during deployment in space. Thus, we need to include the influence of various shape errors to the performance of suppressing starlight and generate realistic images. To model various asymmetric errors, I change the value of the apodization function for a specific petal $A(n, r)$, i.e., A in Eq. 2.17 is now dependent on petal index n. Here I demonstrate the error effect of two shape errors: truncated tips and petal clocking. More detailed investigation on the general forms of the shape errors and the tolerance can be found in Ref. 8.

3.4.1 Truncated tip

When designed, the starshade shape changes smoothly from the solid center to the petals, and then to the open space. However, due to limited manufacturing abilities and accidental errors, tips and valleys could possibly be truncated. I will refer to the starshade with such errors as a truncated starshade for simplicity. To model the petal number n truncated by an amount of x, we can set the apodization profile $A(n, r)$ equal to zero for radial distances $r \geq (R - x)$, where R is the designed radius.

We use a specific truncated starshade as an example to demonstrate the effect of the truncation. The radius of one petal of this truncated starshade is shortened by 6.5 mm, resulting in a tip width of 48.3035 mm (the radius of the designed starshade

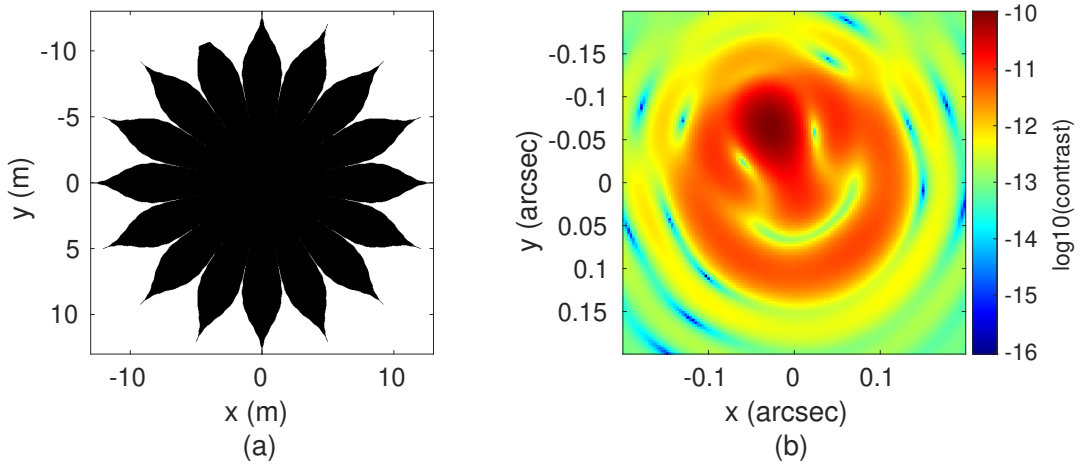

Figure 3.8: Effects of a truncated tip. (a) To better illustrate the truncation defect, the starshade is truncated by 1.6246 m in radius, resulting in a tip width of 0.8921 m. The exaggerated defect size in the figure is not to scale and is only for illustration purposes. For image simulation, the truncation is much smaller. (b) The starshade has a tip truncation in the same position as that in (a), but the radius of one petal is only truncated by 0.0065 m, resulting in a tip width of 0.0483 m. The resulting PSF is brighter in the corner because of the effect of the truncation.

is 13 m and the petal tip width is 48.3216 mm). The defect is illustrated in 3.8(a) and its corresponding PSF is shown in figure 3.8(b). The PSF is disturbed by the leaking light from the truncated tip. A comparison of the PSFs with different degrees of truncation on the same petal is shown in figure 3.9. Judging from this figure, larger truncations lead to a brighter PSF, as we would expect. Meanwhile, as the truncation size gets larger, the shape of PSF becomes symmetrical but not centered.

3.4.2 Petal clocking

The diameter of a starshade is on the order of tens of meters, so the starshade will be folded to fit inside a rocket, and then deploy to the designed shape in space. Each petal has to go to the designed place accurately to ensure good optical performance when the starshade unfolds in space. Here, I demonstrate one of the possible deployment

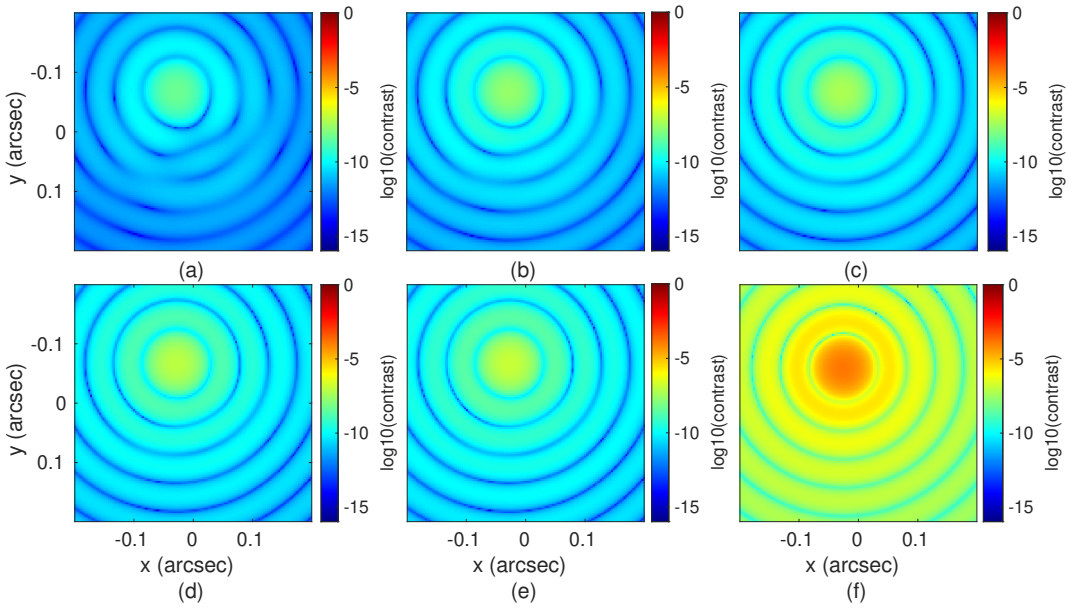

Figure 3.9: PSFs of light sources for starshades with different truncation sizes. The light source, the starshade, and the telescope are aligned. The position of the truncation is the same as shown in Fig. 3.8(a). (a). The petal is truncated by 0.0325 m, resulting in a tip width of 0.0482 m. (b). The petal is truncated by 0.0650 m, resulting in a tip width of 0.0481 m. (c). The petal is truncated by 0.0975 m, resulting in a tip width of 0.0480 m. (d) The petal is truncated by 0.1300 m, resulting in a tip width of 0.0478 m. (e). The petal is truncated by 0.1625 m, resulting in a tip width of 0.0477 m. (f). The petal is truncated by 1.6246 m, resulting in a tip width of 0.8921 m. As the truncation size gets larger, the PSF becomes brighter and its shape is asymmetrical at first and symmetrical later. Moreover, the PSF is not centered.

errors: petal clocking. I will refer to the starshade with such errors as a petal-clocking starshade for simplicity. I add a constant angle shift for number n petal in equation 2.17. The shifted petal will be located partially in the number $n-1$ or $n+1$'s region. That is to say, the revision of one petal will influence the petal area beside it. I choose the union of shifted number n petal and number $n-1$ or $n+1$ petal.

One example starshade, one of whose petals is clock-wise displaced, and the resulting PSF are shown in Fig. 3.10. Similar to a truncated starshade, the PSF of a petal-clocking starshade is disturbed by the leaking light from the displaced petal. A comparison of the PSFs with different degrees of petal displacement on the same

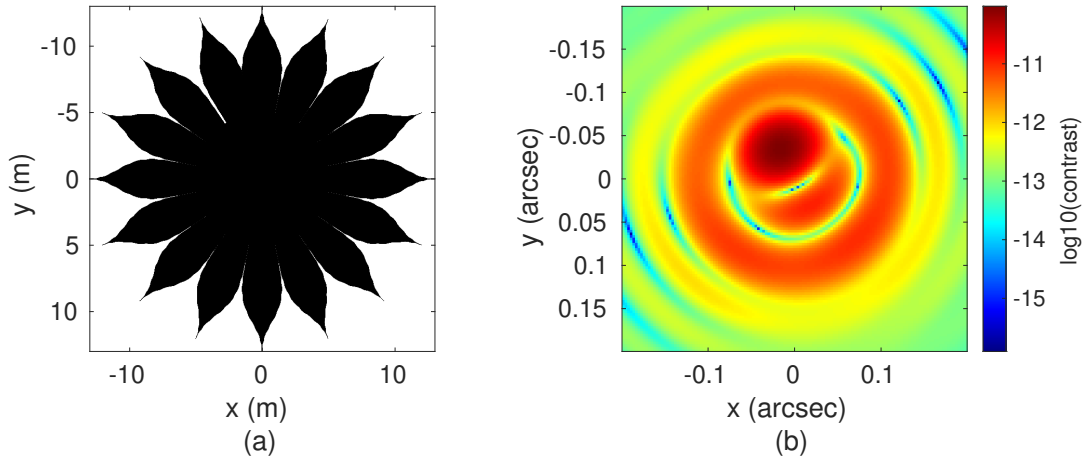

Figure 3.10: Effects of clocking petals. (a) To better illustrate the displacement defect, the petal is clock-wise rotated by $\frac{\pi}{128}$ rad. The exaggerated defect size in the figure is not to scale and is only for illustration purposes. For image simulation, the clocking angle is much smaller. (b) The PSF for the system with a starshade that has a clocking angle of $\frac{\pi}{65536}$ rad in the same position as that in (a). The resulting PSF is brighter in the corner because of the effect of the defect, compare to the PSF from the perfect starshade in Fig. 3.4.

petal is shown in figure 3.11. Judging from this figure, larger displacement leads to a brighter PSF, as we would expect. Meanwhile, as the size of the displacement gets larger, the shape of PSF becomes symmetrical but not centered.

3.5 Detector model

3.5.1 Stochastic model for EMCCDs in photon counting mode

With the information in the previous sections, we are able to obtain the photon flux arriving on the detector. The last step of simulating a realistic image is to include the detector model.

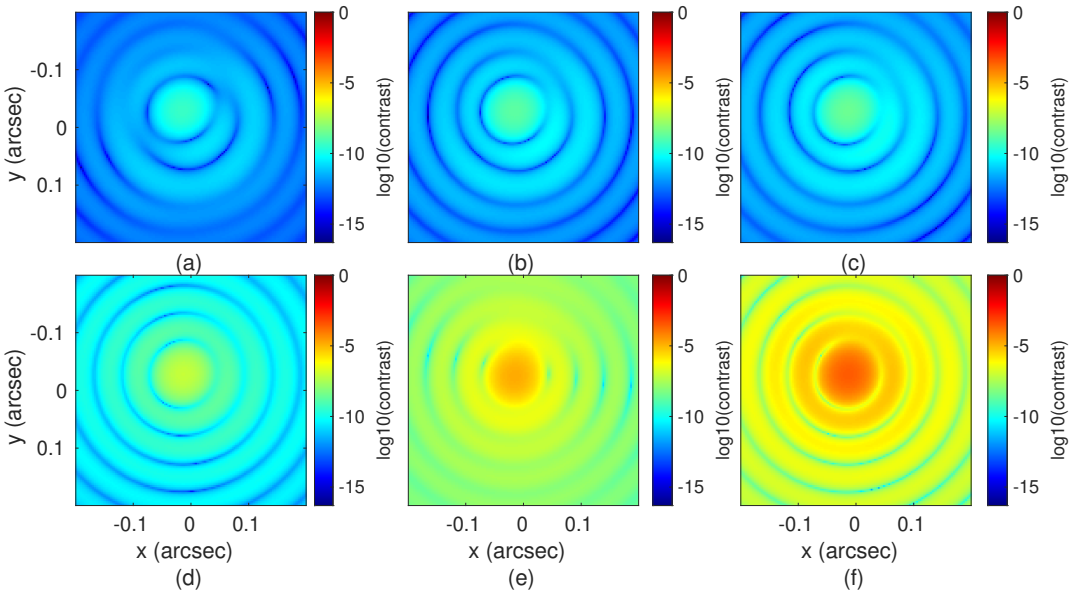

Figure 3.11: PSFs of light sources for starshades with different petal-clocking angles. The light source, the starshade and the telescope are aligned. The position of the petal clocking is the same as shown in Fig. 3.10(a). (a). The petal is rotated clock-wise by $\frac{\pi}{32768}$ rad. (b). The petal is rotated clock-wise by $\frac{\pi}{16384}$ rad. (c). The petal is rotated clock-wise by $\frac{\pi}{8192}$ rad. (d) The petal is rotated clock-wise by $\frac{\pi}{2048}$ rad. (e). The petal is rotated clock-wise by $\frac{\pi}{128}$ rad. (f). The petal is rotated clock-wise by $\frac{\pi}{32}$ rad. As the angle gets larger, the PSF becomes brighter and its shape is asymmetrical at first and symmetrical later. Moreover, the PSF is not centered.

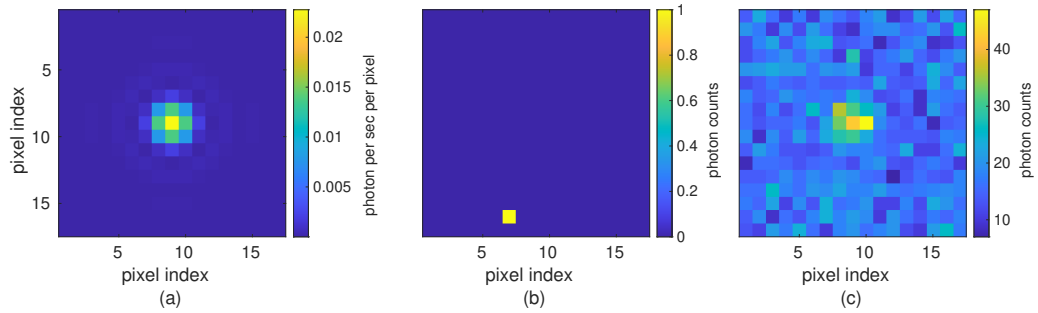

Figure 3.12: (a) Simulated point spread function (PSF) for The Nancy Grace Roman Space Telescope without a starshade for a 1e-8 Jy light source, 0.021 arcsec/pixel. (b) A photon counting (PC) image of (a) with 1s integration time. (c) A co-added image from 2000 sequential PC images.

Hirsch et al.[48] present a detailed imaging process for an EMCCD and build a statistical model for each stage of the imaging process. Their statistical model is built as follows[48]. First, incident photons follow a Poisson process. Second, the EM register is represented by a gamma distribution. Third, readout noise is added using a Gaussian distribution. Fourth, a threshold is applied to give a binary result.

Hirsch et al. use some approximations to simplify and arrive at the equation for the probability distribution for the number of electrons in a pixel,

$$p(n_{ic}) = \begin{cases} \frac{1}{\sqrt{2\pi}\sigma} exp(-\lambda - \frac{(n_{ic}-B_{PC})^2}{2\sigma^2}) + \frac{2}{g} F_{\chi}(2\lambda; 4, \frac{2n_{ic}}{g}), & n_{ic} > 0 \\ \frac{1}{\sqrt{2\pi}\sigma} exp(-\lambda + \frac{B_{PC}^2}{2\sigma^2}), & n_{ic} = 0, \end{cases} \tag{3.3}$$

where λ is the expected number of input electrons for the EM register,

$$\lambda = s \times q \times t + d \times t + CIC; \tag{3.4}$$

s is the photon rate; q is the quantum efficiency; t is the integration time; d is the dark current; CIC is the clock induced charge; n_{ic} is the number of counts after the EM register, including readout noise; $p(n_{ic})$ is the probability of counts n_{ic}; σ is the standard deviation of the readout noise; g is the EM gain; B_{PC} is the bias in PC mode; $F_{\chi}(2\lambda; 4, \frac{2n_{ic}}{g})$ is the non-central χ^2 distribution for 2λ with 4 degrees of freedom and the non-centrality parameter $\frac{2n_{ic}}{g}$. Units for these parameters are shown in Table 3.1.

An EMCCD decreases the read-out noise to the sub-electron level by amplifying the signal before readout. However, the amplification process introduces an excess noise factor (ENF) that reaches $2^{\frac{1}{2}}$ at high gains[100]. The effect on the signal to noise ratio (SNR) is the same as if the quantum efficiency of the EMCCD were halved[22]. This can be overcome completely by operating in photon counting (PC) mode. PC mode applies a single threshold at the final stage and reports a binary result. The

pixel registers a detected photon if its count level is higher than a specified threshold, and reports no photon otherwise. This solution alleviates the ENF without making any assumption on the signal's stability across multiple images[22].

Combining models for all the stages described above produces the final model, which calculates the probability of getting a value of 1 in a detector pixel given a certain incident intensity. Thus, with a threshold of $B_{PC}+T\times\sigma$, set by the threshold parameter T, the probability of detecting a value of one is:

$$f(s) = \int_{B_{PC}+T\times\sigma}^{\infty} p(n_{ic})\, dn_{ic}. \tag{3.5}$$

where $f(s)$ is shortened for $f(s; q, t, CIC, d, g, B_{PC}, \sigma, T)$ (the detector parameters are not shown explicitly). The value in each pixel in each image only has two outcomes: either 1 or 0. The probability of getting a value of 1, $f(s)$, is decided by the ground-truth of the flux, s. As the flux in each pixel is fixed for stable observations, the probability is fixed. That is to say, the measurement in each pixel in each image satisfies a Bernoulli distribution (the Bernoulli distribution is simply the probabilities of "heads" (p) and "tails" (1-p) in a weighted coin flip). In this work, the values of detector parameters are shown in Table 3.1, which are similar to the parameter values for the Nancy Grace Roman Space Telescope[84], and a starshade is aligned for starlight suppression. I assume that all the detector parameters such as integration time are fixed, which is reasonable assumption as the total integration time for the images needed in our analysis is short enough (Please see Ch.). Therefore, for each pixel, the imaging result follows a Bernoulli distribution whose probability of value 1 is only related to the flux value in the pixel. Fig. 3.13 shows results for the detection probability given different flux levels and the calculated derivative of this probability. The detection probability increases as the flux increases, where a very small flux or a very large flux tends to give deterministic zero or one measurement.

The choice of imaging parameters (integration time, PC threshold, etc.) helps efficiently detect signals. The binary value in PC images only indicates the existence of photons in a pixel during the integration time but does not reveal the exact number of the photons. To utilize the photons efficiently, the exposure time is chosen so that the expected photon count in any pixel is much less than 1. To decide a threshold for PC, we need to also pay attention to signal intensity and integration time, because they have similar influence on the result. Suppose that we have decided on the integration time and the expected range of signal intensity. To determine the imaging parameters, we can directly utilize the area under the receiver operating characteristic (ROC) curve (AUC) (Details of ROC and AUC are in Sec. 4.4.), which is a number reflecting the overall detection performance. For one threshold, we can calculate the average of the AUCs for different signal intensities in the expected intensity range. The threshold with the largest average AUC should be chosen.

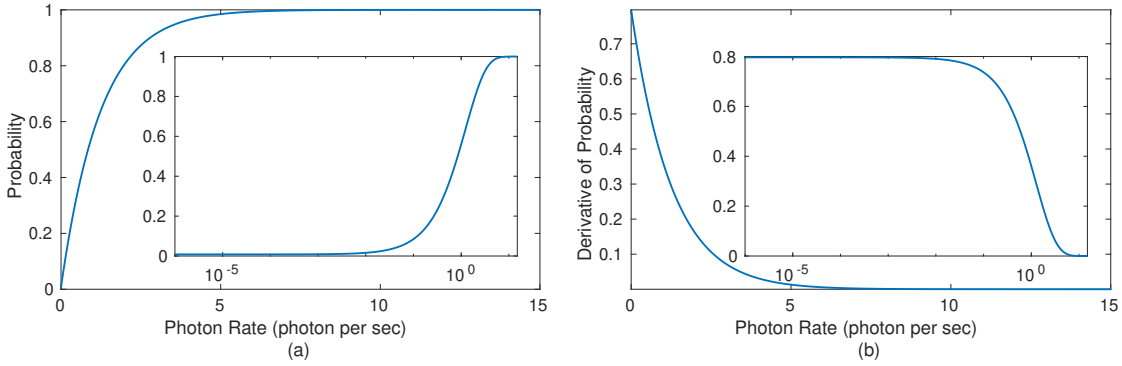

Figure 3.13: Detection probability and its derivative. (a) Detection probability as a function of photon flux, $f(s)$, calculated by Eq. (3.5), where s is in units of photons per second. (b) Derivative of the detection probability. The inserts are the same plots shown with a logarithmic abscissa. I use the detector parameters values shown in Table 3.1, which are similar to the parameter values for the Roman Telescope[84] and assume a starshade for starlight suppression.

Table 3.1: Parameters for simulation of solar system as viewed from 10 parsec.

Parameter	Value	Unit
Sun flux	45.66	Jy
Venus flux	2.99e-8	Jy
Earth flux	4.85e-9	Jy
Venus angular separation	70	mas
Earth angular separation	96	mas
Radius of the ROI	100	mas
Wavelength	0.55	μm
Bandwidth	0.12	μm
Radius of the starshade	13	m
Separation between starshade and telescope	3.72e7	m
Telescope diameter	2.4	m
Detector's pixel size	0.021	$arcsec$
Quantum efficiency	1	ph/e^-
Integration time	1	s
Clock-induced charge	0.01	$e^- pixel^{-1} frame^{-1}$
Dark current	2×10^{-4}	$e^- pixel^{-1} s^{-1}$
Electron-multiplying gain	2500	$-$
PC Bias	200	$e^- pixel^{-1} frame^{-1}$
Standard deviation of readout noise	100	$e^- pixel^{-1} frame^{-1}$
Threshold Parameter	5.5	$-$
Number of PC images in one co-added image	2000	$-$

3.5.2 Co-added images

Typically, the 'binary' PC images are not used directly, but rather are added together to create a final image, which I will call a co-added image. In this way, the co-added images have a large enough dynamic range so the different intensity of the sources can be well-reflected. The number of PC images to combine into one co-added image is denoted by N_{im}. In this work, I use $N_{im} = 2000$, if not specified otherwise; guidance on how to choose N_{im} is provided in Sec. 4.2.4. To visualize the detector's performance, Monte Carlo is used to calculate the probability density functions (PDF) of the photon counts for different ground-truth photon flux in a co-added image from 2000 PC images, shown in Fig. 3.14(a). Four of the PDF's are plotted in Fig. 3.14(b); the parameters in the simulations are listed in Table 3.1. A

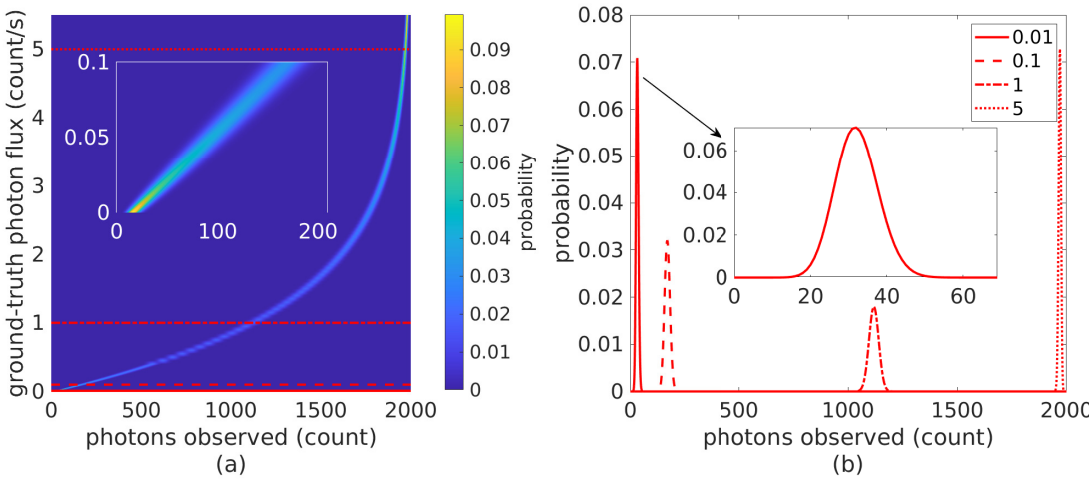

Figure 3.14: Probability density functions of the photon counts for different ground-truth photon flux. (a). Each row is the probability density function (PDF) of photon counts observed in one pixel in a co-added image from 2000 PC images corresponding to the photon flux in that pixel. (b). Example PDF's of the photon counts for four different ground-truth photon flux, which correspond to the ones in (a). The PDF of photon counts observed in one pixel in a co-added image from 2000 PC images corresponding to the photon flux 0.01 count/s, 0.1 count/s, 1 count/s and 5 count/s in the pixel.

photon rate of 0.1 photon/s (our expected maximum rate) is well within the linear response regime.

3.6 Example results

With the tools mentioned above, I am able to simulate realistic starshade images. I present the simulated starshade images for the solar system as viewed from 10 pc away. The starshades used are a perfect one as designed, two truncated starshade with different sizes of truncation, and two petal-clocking starshades with different sizes of misplacement. The starshade as designed can effectively suppress the starlight, but the bright dust will affect the visibility of the Earth signal, as shown in Fig. 3.15. Even small starshade defects will introduce bright spots in the image, which may be mistaken as planet signals, as shown in Figures 3.16 to 3.19.

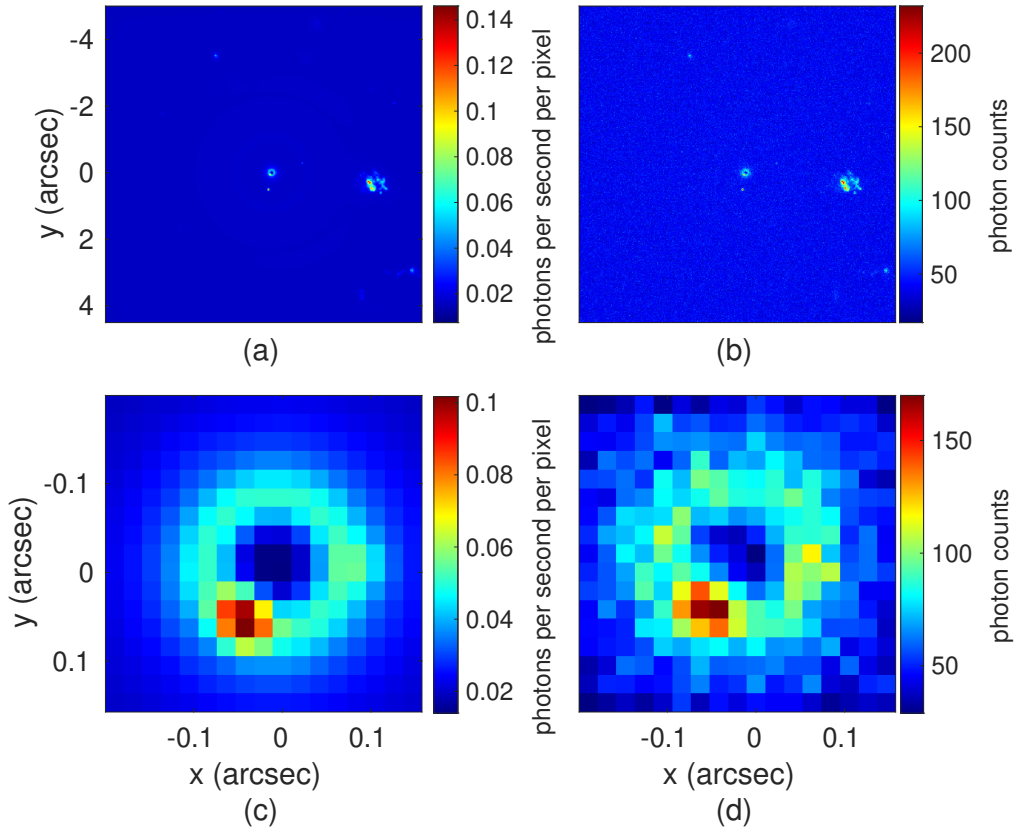

Figure 3.15: The simulated starshade image for the solar system as viewed from 10 pc−astronomical scene from Haystacks[86] as in Fig. 3.3 . The bottom row are zoomed-in views of the images above. The left column is a simulated image with a perfect starshade at $\lambda = 0.55$ μm and with a bandwidth of $\lambda = 0.12$ μm, and no detector noise. The right column is the coadded image from 2000 PC images. The starshade successfully suppressed the starlight in the center. Mars is too dim to be seen and Earth is of similar brightness as the exozodiacal dust.

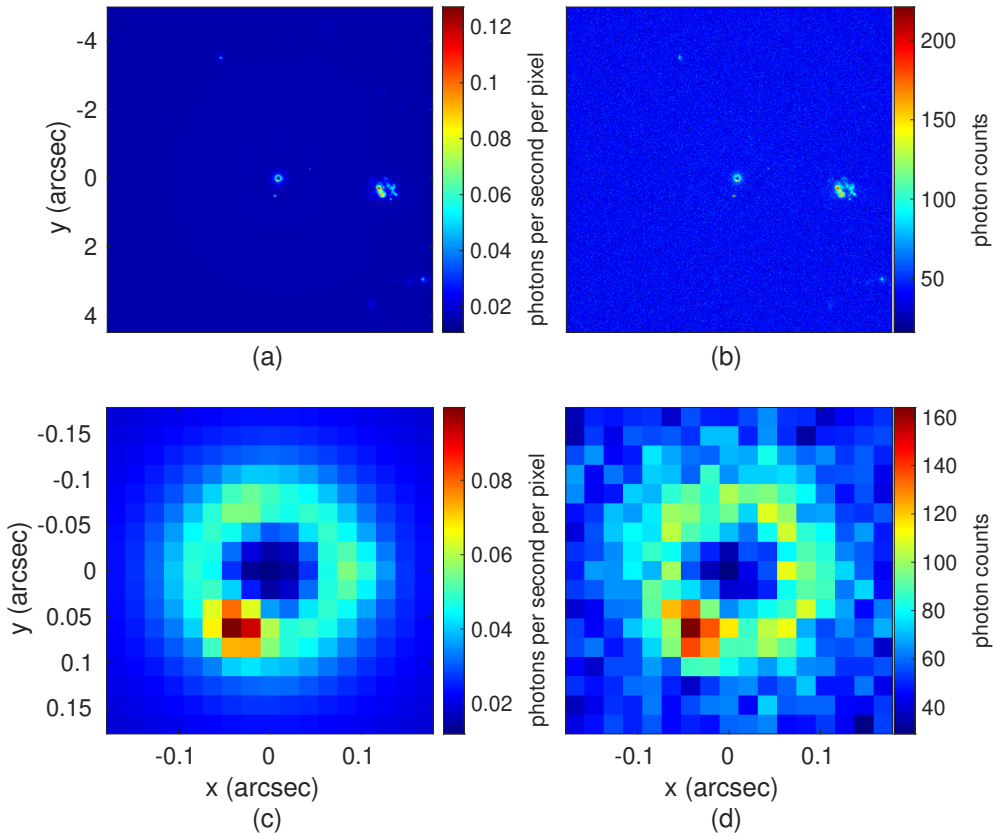

Figure 3.16: The simulated image for the solar system as viewed from 10 pc – astronomical scene from Haystacks[86] as in Fig. 3.3 with a truncated starshade. The bottom row are zoomed-in views of the images above. The starshade has a tip truncated by 0.0065 m as in Fig.3.8 . The left column is a simulated image with a truncated starshade, and no detector noise. The right column is the coadded image from 2000 PC images. The starshade successfully suppressed the starlight in the center. Mars is too dim to be seen and Earth is of similar brightness as the exozodiacal dust. There is a bright spot caused by starshade defects.

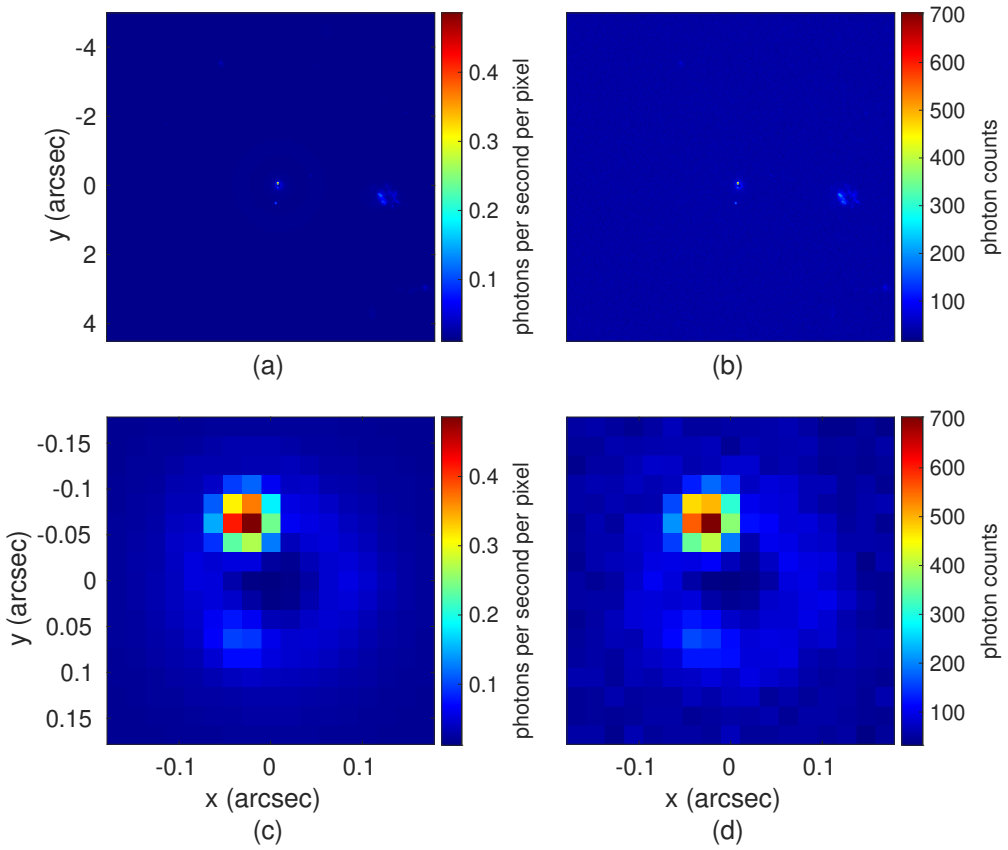

Figure 3.17: The simulated starshade image for the solar system as viewed from 10 pc − astronomical scene from Haystacks[86] as in Fig. 3.3 . The bottom row are zoomed-in views of the images above. The starshade has a tip truncated by 0.0325 m as in Fig.3.8 . The left column is a simulated image with a truncated starshade, and no detector noise. The right column is the coadded image from 2000 PC images. The starshade successfully suppressed the starlight in the center. Mars is too dim to be seen and Earth is of similar brightness as the exozodiacal dust. There is a bright spot caused by starshade defects.

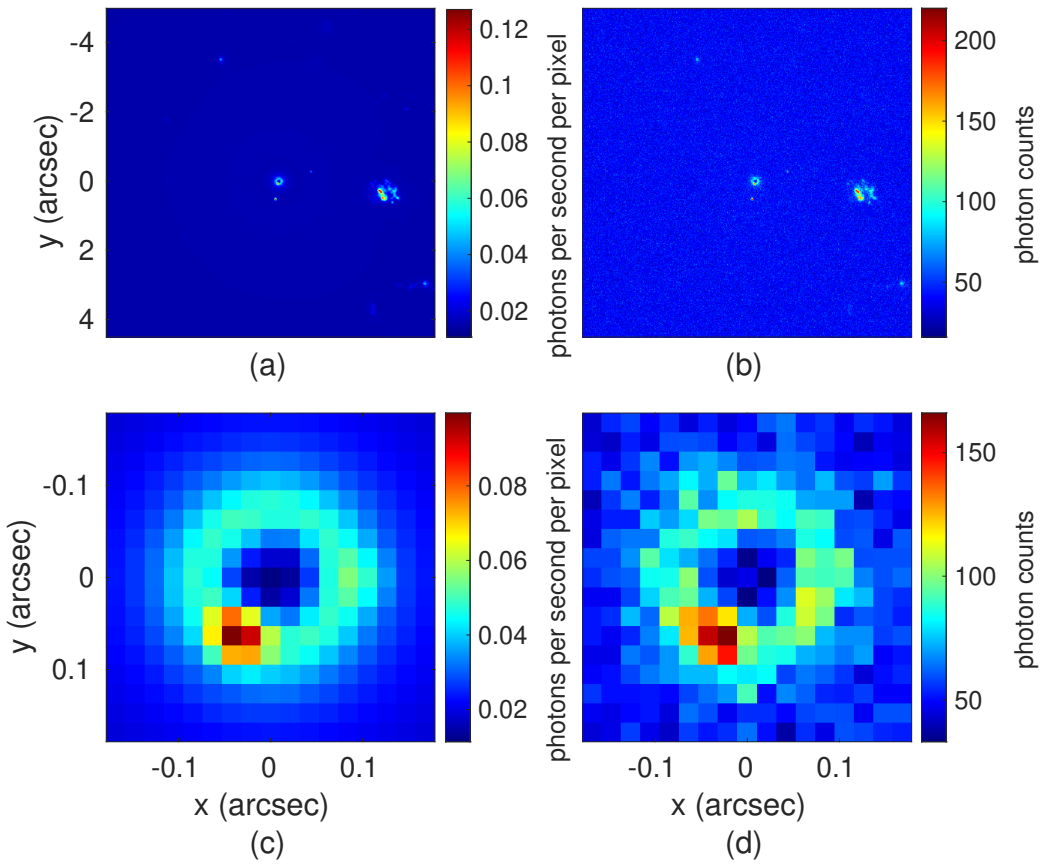

Figure 3.18: The simulated starshade image for the solar system as viewed from 10 pc − astronomical scene from Haystacks[86] as in Fig. 3.3 . The bottom row are zoomed-in views of the images above. The starshade has a clocking angle of $\frac{\pi}{128\times512}$ rad in the same position as that in Fig. 3.10(a). The left column is a simulated image with a petal-clocking starshade, and no detector noise. The right column is the coadded image from 2000 PC images. The starshade successfully suppressed the starlight in the center. Mars is too dim to be seen and Earth is of similar brightness as the exozodiacal dust. There is a bright spot caused by starshade defects.

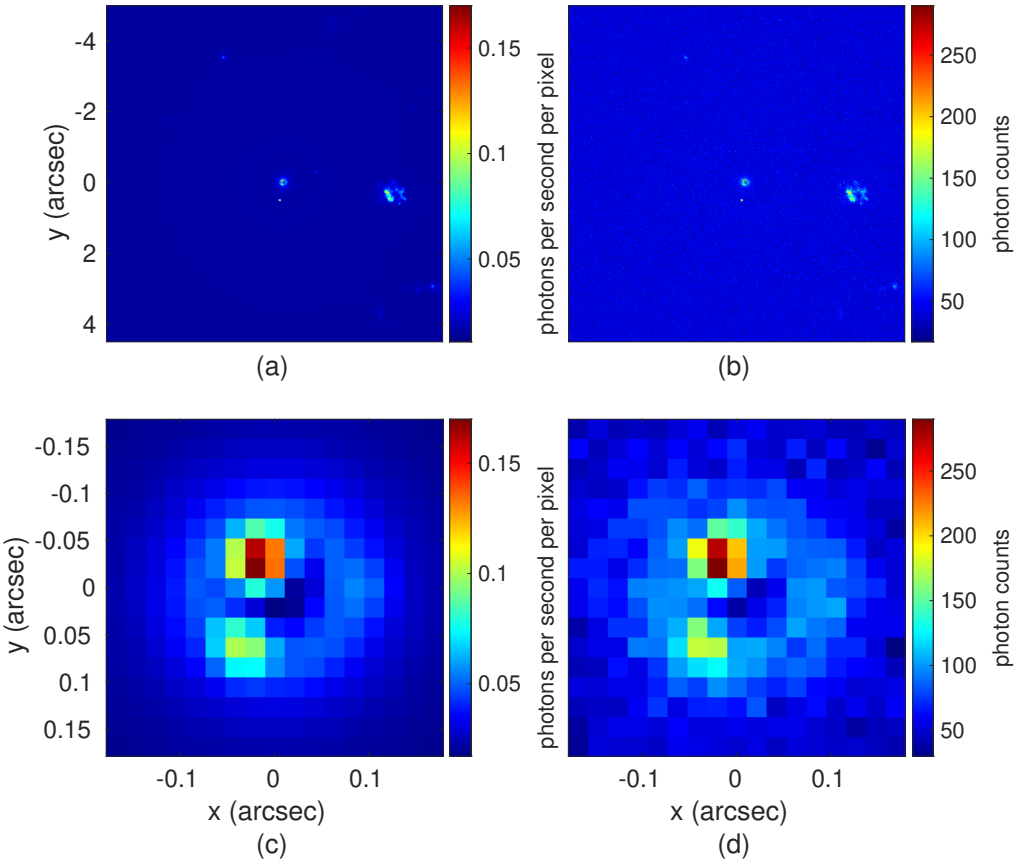

Figure 3.19: The simulated starshade image for the solar system as viewed from 10 pc − astronomical scene from Haystacks[86] as in Fig. 3.3 . The bottom row are zoomed-in views of the images above. The starshade has a clocking angle of 0.00019175 rad in the same position as that in Fig. 3.10(a). The left column is a simulated image with a petal-clocking starshade, and no detector noise. The right column is the coadded image from 2000 PC images. The starshade successfully suppressed the starlight in the center. Mars is too dim to be seen and Earth is of similar brightness as the exozodiacal dust. There is a bright spot caused by starshade defects.

Chapter 4

Signal Detection

4.1 Introduction and problem statement

4.1.1 Introduction

This chapter presents automatic detection methods for starshade missions. This work is motivated by the lack of any previous investigation into signal detection in starshade images. We begin the chapter by reviewing past work on signal detection for direct imaging, most of which are specialized to coronagraph images. Because of the difference in the noise properties in coronagraph images and starshade images, previous work on signal detection in coronagraph images loses its utility on starshade images.

The biggest challenge for coronagraph images is the noise floor set by quasi-static speckles. Different observing techniques and post-processing methods have been developed to try to attenuate the speckles before attempting detection. They are all based on differential imaging, which consist of estimating the star-only coronagraphic image and subtracting it from the science images (also called speckle subtraction technique). Differential imaging relies on specific observation strategies such as angular diversity (ADI)[70], spectral diversity (SDI)[69], or multiple reference star im-

ages (RSDI)[1] to generate the differential signal. The KL Image Projection (KLIP) algorithm[96] and Locally Optimized Combination of Images (LOCI) algorithm[64] are popular post-processing algorithms for star PSF subtraction. However, for starshade images, the residual starlight is minimal and there are no quasi-static speckles, which means these techniques and algorithms are less important. The various speckle subtraction methods developed for coronagraphic images may serve to improve detection in starshade images, but it is beyond the scope of this work to include them. We focus on planet detection in images that have not been post-processed and leave that work to be done in the future.

In my work, I do not post-process the images (as in speckle subtraction), so we now move to detection methods. Ref. 6 and Ref. 58 use hypothesis testing for the detection. The unknown parameters such as the planets' positions and intensities can be removed by marginalizing the probability[6] or using worst-case values [58]. However, the choice of priors or using the worst-case values is an open question. Ref. 58 assumes a known constant background; in my method, I will estimate the background by a maximizing the likelihood. Ref. 73 (SNRt map) essentially tests if the intensity of a single test resolution is different from the other resolution elements in a $1\lambda/D$-wide annulus at the same radius. They use small sample statistics to address the problem of the statistical significance of detection when few realizations of spatial speckles vs azimuth are present. Ref. 10 (ANDROMEDA) makes a signal template considering over/self subtraction caused by ADI rather than directly using a theoretical PSF template when calculating maximum likelihood estimation (MLE). Ref. 88 (FMMF) also uses SNR based methods. They include KLIP-induced distortion in the match-filter template to estimate the signal intensity. The standard deviation is calculated at each pixel while masking a disk with a 5-pixel radius centered on that pixel from the annulus to prevent a planet from biasing its own SNR. Ref. 33 (PACO) uses GLRT and uses the full-covariance rather than assume independent and identically

distributed in the time dimension for the different frames. However, they assume the covariance is the same under the two hypotheses (The null hypothesis (H_0) is that there is no planet; the alternative hypothesis (H_1) is that there is a planet.) and thus calculate only one covariance. Moreover, this covariance is not derived from the gaussian equation together with the signal intensity, and thus the result is not guaranteed to be MLE. Ref. 77 (STIM map) uses a Modified Rician distribution, which is a heavy tail distribution compared to Gaussian, to model the speckles. Ref. 21 (RSM map) uses a Markov process to model the same pixel throughout the different images. They claim the residual quasi-static speckles after ADI can be characterized by their mean and variance. Recent studies also take the detection problem as a binary classification problem, using random-forest classifiers (SODIRF) and deep neural networks (SODINN)[35]. However, these machine learning methods need very large training sets, which are difficult to generate for unknown planet signals, and require a heuristic tuning of hyper-parameters.

In this study, we also take the detection problem as a "hypothesis testing" problem and use a Generalized Likelihood Ratio Test (GLRT). The null hypothesis (H_0) is that there is no planet; the alternative hypothesis (H_1) is that there is a planet. We compare the posterior probabilities under the two hypotheses to decide whether to reject the null. Instead of marginalization, we use MLE to first estimate the unknown parameters and then use them to calculate the likelihood ratio. Using this ratio, even when the maximum likelihood under the alternative hypothesis is low, we may still have a strong detection as long as the ratio is high (i.e., the pattern is much less likely from pure noise). Compared to other likelihood ratio tests, the GLRT can include hypothesis tests which have unknown parameters in the two hypotheses. GLRT uses MLE to estimate the unknowns and then calculates the maximum likelihood ratio. In other words, the MLEs of the unknown parameters such as signal intensity and background intensity, under both positive and negative hypotheses, are first required

to be calculated. Then, a likelihood ratio test using the MLEs can be calculated and applied to decide whether a signal has been detected.

For this work, as a demonstration of the detection method, we use a PSF template as the underlying signal model to detect point sources (planets) in starshade images. However, different signal models can be used and the later discussion of the detection method is still valid; the only difference would be detecting signals with different templates. This provides my methods with broad applicability to various observation scenarios.

We first introduced the GLRT method for co-added images under Gaussian distribution and its preliminary results in Ref. 50. Then, we improved the method by modeling PC images' probability distribution directly from the detector model in Ref. 54. We further analyzed the two methods with a comparison of different methods and receiver operating characteristic curves, and introduced a preliminary study for cases with exozodiacal dust in Ref. 52, 53. In the following sections, we briefly describe the underlying model for starshade images and introduce the general concept of GLRT. Then, GLRT for co-added images is presented. We also extend the method for cases with exozodiacal dust. After that, the improved GLRT methods working directly with PC images is introduced. In this chapter, we also present performance analysis for different methods and utilize the analysis to guide the choice of imaging parameters.

4.1.2 Problem statement

The model for the noiseless image, i.e., the flux arriving on the detector, is

$$\boldsymbol{M} = \sum_{i=1}^{N_x} \sum_{j=1}^{N_y} \alpha_{i,j} \boldsymbol{x}_{i,j} + \boldsymbol{\beta}, \tag{4.1}$$

where $\boldsymbol{M}$ is the matrix for the noiseless image; $\boldsymbol{x}_{i,j}$ is the matrix denoting the values of a normalized PSF centered at (i, j); $\alpha_{i,j}$ is the intensity of the planet relative to the normalized reference PSF at pixel (i, j) in unit of Jy (the value is zero if there is no signal at (i, j)); $\boldsymbol{\beta}$ is the matrix for background such as dust and light leakage from starshade defects and star residual light and bias from the detector; N_x, N_y are the number of pixels in the x and y axes.

Model for an image window

To approach the detection problem, we use the idea of divide-and-conquer. We assume no overlapping signals in the image, so we are able to individually analyze smaller image windows that are the size of the PSF core centered on each pixel one by one, which will be called an image window from here on. In an image window with the size of the PSF core, we can assume that there is only one planet signal. We also assume the background is constant, which should be a reasonable assumption over a small area. Thus, the model for a noiseless image window is:

$$\boldsymbol{s} = \alpha \boldsymbol{x} + \beta \mathbf{1}\,, \tag{4.2}$$

where $\boldsymbol{s}$ is the noiseless result,i.e., the input flux arriving on the detector; $\boldsymbol{x}$ is a reference PSF core of the telescope centered in the area; α is the intensity of the planet relative to the source intensity of the normalized reference PSF (If there is no planet signal, α should be zero.); β is the background light (such as dust and light leakage from starshade defects), and $\mathbf{1}$ is the identity matrix. We stack pixel values in the target area into a column vector for easier mathematical manipulation later. That is to say, $\boldsymbol{s}$ and $\boldsymbol{x} = (x_1, \cdots, x_K)^T$ are column vectors (the subscripts of x represent the pixel indices and K is the total number of pixels in a PSF core). The model states that the area we are observing, $\boldsymbol{s}$, contains a signal centered at the

center of this area along with constant background light. If there is no planet signal, α should be zero.

In real life, due to the randomness of photons and the detector noise, we wouldn't be able to observe $\boldsymbol{s}$ directly, but rather collect the noisy image output from the detector. Assume that N PC images have been collected, which is denoted as $\boldsymbol{y} = \{\boldsymbol{y}_1, \cdots, \boldsymbol{y}_N\}$, and each PC image has K pixels $\boldsymbol{y_n} = (y_{n,1}, \cdots, y_{n,K})^T$. The meaning of indices and symbols are illustrated in Fig. 4.1.

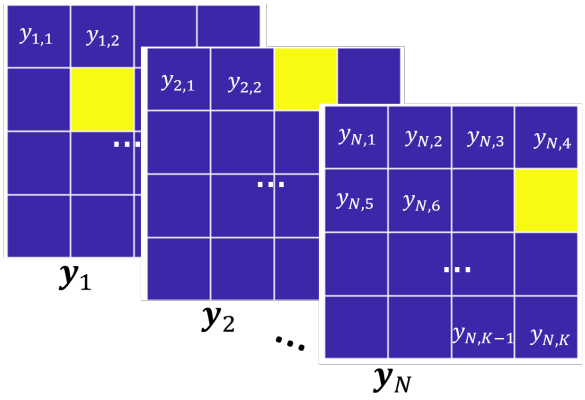

Figure 4.1: Illustration for the variables in the model. K is the number of pixels in each PC image (with the size of PSF core). N is the number of PC images.

The detection problem can be stated as: given the data set $\boldsymbol{y}$, decide which of the two hypotheses is true:

$$\begin{aligned} & H_0 : \alpha = 0 \\ & \text{versus} \\ & H_1 : \alpha \neq 0\,, \end{aligned} \tag{4.3}$$

where the null hypothesis H_0 is that no planet signal exists in the target area; the alternative hypothesis H_1 is that a planet signal exists in the target area. Moreover, it is a composite hypotheses testing problem, where not only α but also β are unknown.

To decide which hypothesis is true, it is intuitive to compare the likelihood of H_1 and H_0 when $\boldsymbol{y}$ occurs. The likelihood ratio (also called odds ratio) is:

$$O(\boldsymbol{y}) = \frac{\mathcal{L}(H_1|\boldsymbol{y})}{\mathcal{L}(H_0|\boldsymbol{y})} = \frac{P(\boldsymbol{y}|H_1)}{P(\boldsymbol{y}|H_0)} = \frac{\int\int h_1(\rho)h_2(\mu)P(\boldsymbol{y}|\alpha=\rho,\beta=\mu)d\rho d\mu}{\int h_3(\mu)P(\alpha=0)P(\boldsymbol{y}|\alpha=0,\beta=\mu)d\mu}\,, \tag{4.4}$$

where $h_1(\cdot)$ is the probability density function of the planet intensity, and $h_2(\cdot)$ and $h_3(\cdot)$ are the probability density functions of the background intensity. We should decide H_1 is true if the odds ratio is larger than one [6]. However, since we have no prior information about the probability distribution of the exoplanet intensity , or the background light during detection, the posterior probability of the observation under the two hypotheses cannot be calculated to decide which hypothesis is more likely. One solution for this challenge is to use the maximum likelihood. We can conduct a generalized likelihood ratio test (GLRT) or also called maximum-likelihood test, i.e., we determine whether there is an exoplanet signal based on the maximum-likelihood ratio. We decide that H_1 is true if the maximum likelihood ratio,

$$R(\boldsymbol{y}) = \frac{\max\limits_{\alpha,\beta} P(\boldsymbol{y}|\alpha,\beta;H_1)}{\max\limits_{\beta} P(\boldsymbol{y}|\alpha=0,\beta;H_0)}\,, \tag{4.5}$$

is larger than a threshold. As we care most about α and β, we only explicitly listed these two parameters in Eqs. eqs. (4.4) and (4.5). Under certain assumptions, there are additional unknown parameters such as noise statistics, and they should be treated in the same way as α and β.

Here we introduce the odd ratio statement but do not mention the detailed probability expressions, which will be elaborated in the following sections. A Gaussian model for co-added images is first discussed in Sec. 4.2 and is further optimized for cases with exozodiacal dust. Then, a more accurate model directly calculating the probability for each signal PC image is presented in Sec. 4.3.

Model for the whole image

We have built a model for an image window that is the size of the PSF core above and will introduce the corresponding detection and estimation method for the image window in the following sections. In reality, an image much bigger than the size of a PSF core will be examined for an unknown number of planets in unspecified locations. Thus, the detection procedure described above is repeated for each image window (a set of K pixels close together) across the whole image. For each pixel, we use the image window centered at this pixel, that is to say, we test H_1: there is a planet centered at this pixel, against H_0: there is only constant background there. Repeating the calculation for all the pixels in the image generates a log-likelihood ratio map for the image. Then, we choose a false alarm rate and its corresponding threshold. By comparing the map with the chosen threshold, signals would be detected. Illustration of the idea described here and concrete examples are provided in the following sections. They will help readers to better understand the idea and explain the details in the methods during real application.

As we have shown in Chapter 3, the PSF changes with the distance away from the starshade center. If we use only one PSF template in GLRT, normally the one without a starshade, we can have a higher false alarm rate, worse position estimation, and worse intensity estimation. Thus, we use a library of PSFs at different distances from the starshade center for the GLRT model.

4.2 Gaussian Generalized likelihood ratio test in a co-added image

4.2.1 Detection for an image window

As mentioned in Sec. 3.5.2, the common practice is to add PC images together to create a co-added image, which has a large enough dynamic range so the different intensity of the sources can be well-reflected. Thus, I also focus on analyzing the co-added images as the initial attempt.

As the time to take a set of PC images is not long (for example, 2000 s in my example), the ground truth of photon flux arriving on the detector should be unchanged. Moreover, the expected maximum flux rate is well within the detector's linear response regime. Therefore, the underlying linear model Eq. 4.2 should be still applicable when using the PSF template for co-added images. Furthermore, photon counts for the same pixel in different PC images are independent and identically distributed(i.i.d), and the number of PC image to be added into a co-added image is relatively large. Therefore, a Gaussian distribution for the photon counts in the co-added image should be a good approximation for the noise due to the central limit theorem. As a result, the model for an image window on a co-added image is:

$$\boldsymbol{Y} = \alpha \boldsymbol{X} + b\mathbf{1} + \boldsymbol{\omega}\,, \tag{4.6}$$

where $\boldsymbol{Y}$ denotes the image window on a co-added image; $\boldsymbol{X}$ the central core of the PSF template for a co-added image; b is the background intensity in the co-added image(because of the detector's property, this value may not be the same as β in the noiseless case); $\boldsymbol{\omega}$ denotes the Gaussian noise. As mentioned before, values are stacked into column vectors. For easier manipulation, the local model can further be

formulated in the matrix form:

$$\boldsymbol{Y} = \boldsymbol{G}\boldsymbol{\theta}_{\boldsymbol{G}} + \boldsymbol{\omega}\,, \tag{4.7}$$

$$\boldsymbol{G} = \begin{bmatrix} X_1 & 1 \\ X_2 & 1 \\ \vdots & \vdots \\ X_K & 1 \end{bmatrix}, \boldsymbol{\theta}_{\boldsymbol{G}} = \begin{bmatrix} \alpha \\ b \end{bmatrix}\,, \tag{4.8}$$

where the noise $\boldsymbol{\omega}$ have mean zero and follow Gaussian distribution; $\boldsymbol{\theta}_{\boldsymbol{G}}$ is the two unknown parameters. The subscript G means Gaussian distribution The hypothesis testing can also be rewritten in the matrix form as:

$$\begin{aligned} &H_0 : \alpha = \boldsymbol{A}\boldsymbol{\theta}_{\boldsymbol{G}} = 0 \\ &\text{versus} \\ &H_1 : \alpha = \boldsymbol{A}\boldsymbol{\theta}_{\boldsymbol{G}} \neq 0\,, \end{aligned} \tag{4.9}$$

where $\boldsymbol{A} = [1, 0]$. As a result, we have K pixel values and K^2+2 unknown parameters including α, b and K^2 unknown elements in the noise covariance matrix under H_1 and $K^2 + 1$ unknown parameters, i.e., β and $K^2/2$ unknown elements in the noise covariance matrix, under H_0. The character of noise in each pixel is similar, so it is reasonable to assume the noise is i.i.d. spatially. That is to say, we now only have three unknown parameters, i.e., α, b and the variance σ_G^2 , under H_1 and two under H_0, i.e., b and the variance σ_G^2 (for convenience, I directly use variance rather than standard deviation as one variable here).

The conditional probability of N images, $\boldsymbol{y} = \{\boldsymbol{y}_1, \cdots, \boldsymbol{y}_N\}$, can be written as

$$\begin{aligned} L_G(\boldsymbol{\theta_G}, \sigma_G^2) &= p(\boldsymbol{y}|\alpha, b, \sigma_G^2) \\ &= p(\boldsymbol{Y}|\alpha, b, \sigma_G^2) \\ &= \prod_{k=1}^{K} p(Y_k|\alpha, b, \sigma_G^2) \\ &= \frac{1}{(2\pi\sigma_G^2)^{K/2}} \exp\left(-\frac{1}{2\sigma_G^2}\sum_{k=1}^{K}(Y_k - \alpha X_k - b)^2\right) \\ &= \frac{1}{(2\pi\sigma_G^2)^{K/2}} \exp\left(-\frac{1}{2\sigma_G^2}\,||\boldsymbol{Y} - \boldsymbol{G\theta_G}||_2\right). \end{aligned} \tag{4.10}$$

As the data $\boldsymbol{y}$ are known and the parameters $\boldsymbol{\theta_G}, \sigma_G^2$ are unknown, this probability function is a likelihood function for the unknown parameters (so it is also denoted as $L_G(\boldsymbol{\theta_G}, \sigma_G^2)$ above). Taking the natural logarithm of both sides of Eq. (4.10), the log-likelihood of the co-added image is

$$\begin{aligned} l_G(\boldsymbol{\theta_G}, \sigma_G^2) &= \ln(L_G(\boldsymbol{\theta_G}, \sigma_G^2)) \\ &= -\frac{K}{2}\ln(2\pi) - \frac{K}{2}\ln(\sigma_G^2) - \frac{1}{2\sigma_G^2}\sum_{k=1}^{K}(Y_k - \alpha X_k - b)^2 \\ &= -\frac{K}{2}\ln(2\pi) - \frac{K}{2}\ln(\sigma_G^2) - \frac{1}{2\sigma_G^2}\,||\boldsymbol{Y} - \boldsymbol{G\theta_G}||_2 \,. \end{aligned} \tag{4.11}$$

We maximizes the likelihood function (equivalently the log-likelihood function) to find the Maximum Likelihood estimator:

$$(\hat{\boldsymbol{\theta}}_{G,1}, \hat{\sigma}_G^2) = \underset{\boldsymbol{\theta_G}, \sigma_G^2}{\operatorname{argmax}}\; l_G(\boldsymbol{\theta_G}, \sigma_G^2)\,. \tag{4.12}$$

As a Gaussian distribution is used as an approximation for the true underlying distribution, the estimation is called Gaussian quasi-maximum likelihood estimation (QMLE). As long as the quasi-likelihood function is not oversimplified, the QMLE is consistent and asymptotically normal. It is less efficient than the MLE, but may

only be slightly less efficient if the quasi-likelihood is constructed so as to minimize the loss of information relative to the actual likelihood [20]. The QMLE under H_1 is:

$$\hat{\boldsymbol{\theta}}_{G,1} = (\boldsymbol{G}^T\boldsymbol{G})^{-1}\boldsymbol{G}^T\boldsymbol{Y}\,, \tag{4.13}$$

which is equivalent to solving the optimization problem to get the estimation of $\boldsymbol{\theta_G}$:

$$\min_{\boldsymbol{\theta_G}} ||\boldsymbol{Y} - \boldsymbol{G\theta_G}||_2\ . \tag{4.14}$$

And the estimated variance under H_1 is:

$$\hat{\sigma_1^2} = \frac{1}{K}(\boldsymbol{Y} - \boldsymbol{G}\hat{\boldsymbol{\theta}}_{G,1})^T(\boldsymbol{Y} - \boldsymbol{G}\hat{\boldsymbol{\theta}}_{G,1})\,. \tag{4.15}$$

Meanwhile, the QMLE under H_0 is:

$$\hat{\boldsymbol{\theta}}_{G,0} = \hat{\boldsymbol{\theta}}_{G,1} - (\boldsymbol{G}^T\boldsymbol{G})^{-1}\boldsymbol{A}^T\left[\boldsymbol{A}(\boldsymbol{G}^T\boldsymbol{G})^{-1}\boldsymbol{A}^T\right]^{-1}(\boldsymbol{A}\hat{\boldsymbol{\theta}}_{G,1})\,, \tag{4.16}$$

which is equivalent to solving the constrained optimization problem to get the estimation of $\boldsymbol{\theta_G}$:

$$\begin{aligned} &\min_{\boldsymbol{\theta_G}} ||\boldsymbol{Y} - \boldsymbol{G\theta_G}||_2 \\ &\text{s.t. } \boldsymbol{A\theta_G} = 0. \end{aligned} \tag{4.17}$$

And the estimated variance under H_0 is:

$$\hat{\sigma_0^2} = \frac{1}{K}(\boldsymbol{Y} - \boldsymbol{G}\hat{\boldsymbol{\theta}}_{G,0})^T(\boldsymbol{Y} - \boldsymbol{G}\hat{\boldsymbol{\theta}}_{G,0})\,. \tag{4.18}$$

In the problem of parameter estimation, we obtain information about the unknown parameters from the observed data of the random variables from the probability distribution governed by the parameters. The Fisher information matrix is a way to quantify the amount of information that the observable random variables carry about

the unknown parameters. The definition of the Fisher information matrix is

$$\begin{aligned} \boldsymbol{I}(\boldsymbol{\phi}) &= \mathrm{Var}_{\boldsymbol{\phi}}\{\nabla l(\boldsymbol{\phi})\} \\ &= -E_{\boldsymbol{\phi}}\{\nabla^2 l(\boldsymbol{\phi})\}\,, \end{aligned} \tag{4.19}$$

where the notation "Var" means the variance; "E" means expectation; $\boldsymbol{\phi}$ is the vector of unknown parameters and $\boldsymbol{\phi} = (\alpha, b, \sigma_1^2)^T$ for the alternative hypothesis H_1 here. In the case here(a linear model), the Fisher information matrix reduces to [74]

$$\boldsymbol{I}_G(\boldsymbol{\phi}) = \begin{pmatrix} -E\left(\frac{\partial^2 l_G}{\partial\,\boldsymbol{\theta}_{G,1}\,\partial\,\boldsymbol{\theta}_{G,1}^T}\right) & 0 \\ 0 & -E\left(\frac{\partial^2 l_G}{\partial\,(\sigma_1^2)^2}\right) \end{pmatrix}. \tag{4.20}$$

Due to the block structure of $\boldsymbol{I}_G(\boldsymbol{\phi})$, the variance-covariance of $\hat{\boldsymbol{\theta}}_{G,1}$ can be estimated by $\boldsymbol{I}^{-1}_{\boldsymbol{\theta}_{G,1}}$ [74]where

$$\begin{aligned} \boldsymbol{I}_{\hat{\boldsymbol{\theta}}_{G,1}} &= -\frac{\partial^2\, l_G(\hat{\boldsymbol{\theta}}_{G,1}, \hat{\sigma}_1^2)}{\partial\,\boldsymbol{\theta}_{G,1}\,\partial\,\boldsymbol{\theta}_{G,1}^T} \\ &= \frac{\boldsymbol{G}^T\boldsymbol{G}}{\hat{\sigma}_1^2}\,, \end{aligned} \tag{4.21}$$

and we can also derive the confidence intervals for the QMLE[44]:

$$\hat{\alpha} \pm z\sqrt{(\boldsymbol{I}^{-1}_{\hat{\boldsymbol{\theta}}_{G,1}})_{11}}, \tag{4.22}$$

and

$$\hat{b} \pm z\sqrt{(\boldsymbol{I}^{-1}_{\hat{\boldsymbol{\theta}}_{G,1}})_{22}}, \tag{4.23}$$

where z is the appropriate critical value (for example, 1.96 for 95% confidence), and the notation $(\boldsymbol{I}^{-1}_{\hat{\boldsymbol{\theta}}_{G,1}})_{ii}$ means that we invert the matrix $\boldsymbol{I}_{\hat{\boldsymbol{\theta}}_{G,1}}$ first, and then take the ii component of the inverted matrix. The variance of $\hat{\sigma}_1^2$ is estimated by $\boldsymbol{I}_G^{-1}(\hat{\sigma}_1^2)$ [74]

where

$$\begin{aligned} \boldsymbol{I}_G(\hat{\sigma}_1^2) &= -\frac{\partial^2 l_G(\hat{\boldsymbol{\theta}}_{G,1}, \hat{\sigma}_1^2)}{\partial\,(\sigma_1^2)^2} \\ &= \frac{K}{2\hat{\sigma}_1^4}\,. \end{aligned} \tag{4.24}$$

We use the QMLE's and the generalized likelihood ratio in Eq. 4.5 becomes

$$R_G(\boldsymbol{y}) = \frac{P(\boldsymbol{Y}|\hat{\boldsymbol{\theta}}_{G,1}, \hat{\sigma^2}_1; H_1)}{P(\boldsymbol{Y}|\hat{\boldsymbol{\theta}}_{G,0}, \hat{\sigma^2}_0; H_0)}\,, \tag{4.25}$$

where R_G denotes the ratio under the Gaussian assumption; $\hat{\boldsymbol{\theta}}_{G,m}, \hat{\sigma^2}_m$ are the maximum likelihood estimates of the planet intensity, background intensity vector and the standard deviation of the noise under hypothesis H_m with $m = \{0, 1\}$. With the Gaussian assumption, we will be able to derive the expression of $R_G(\boldsymbol{y})$ with the known values in the model. To make the computation simpler, I use

$$\begin{aligned} T(\boldsymbol{y}) &= (K-2)(R_G(\boldsymbol{y})^{\frac{2}{K}} - 1) \\ &= (K-2)\frac{\hat{\sigma}_0^2 - \hat{\sigma}_1^2}{\hat{\sigma}_1^2} \\ &= (K-2)\frac{\hat{\boldsymbol{\theta}}_{G,1}^T \boldsymbol{A}^T[\boldsymbol{A}(\boldsymbol{G}^T\boldsymbol{G})^{-1}\boldsymbol{A}^T]^{-1}\boldsymbol{A}\hat{\boldsymbol{\theta}}_{G,1}}{\boldsymbol{Y}^T(\boldsymbol{1}_K - \boldsymbol{G}(\boldsymbol{G}^T\boldsymbol{G})^{-1}\boldsymbol{G}^T)\boldsymbol{Y}}\,, \end{aligned} \tag{4.26}$$

which can be represented directly use the matrix multiplications of values in the model as shown, rather than $R_G(\boldsymbol{y})$ directly. H_1 is favored, i.e., a planet is more likely to exist at the test location, if

$$T(\boldsymbol{y}) > \gamma_G\,, \tag{4.27}$$

where the threshold γ_G is based on the chosen detection performance. The probability of false alarms (false alarm rate, or false positive rate) $P_{\boldsymbol{FA},G}$ and probability of

detection (true positive rate) $P_{\boldsymbol{D},G}$ are given by

$$P_{\boldsymbol{FA},G} = \int_{T(\boldsymbol{y})>\gamma_G} p(\boldsymbol{y}|H_0)\,, d\boldsymbol{y} = Q_{F_{1,K-2}}(\gamma_G) \tag{4.28}$$

$$P_{\boldsymbol{D},G} = \int_{T(\boldsymbol{y})>\gamma} p(\boldsymbol{y}|H_1) d\boldsymbol{y} = Q_{F'_{1,K-2}(\lambda_G)}(\gamma)\,, \tag{4.29}$$

where Q is the probability of exceeding a given value; $F_{1,K-2}$ is an F distribution with one numerator degree of freedom and K-2 denominator degrees of freedom; and $F'_{1,K-2}(\lambda_G)$ is a noncentral F distribution with one numerator degree of freedom and K-2 denominator degrees of freedom and noncentrality parameter λ_G [60]. λ_G is given by

$$\lambda_G = \frac{\boldsymbol{\theta}^T_{\boldsymbol{G,1}} \boldsymbol{A}^T [\boldsymbol{A}(\boldsymbol{G}^T\boldsymbol{G})^{-1}\boldsymbol{A}^T]^{-1} \boldsymbol{A}\boldsymbol{\theta}_{\boldsymbol{G,1}}}{\sigma^2_G}\,, \tag{4.30}$$

where $\boldsymbol{\theta}_{\boldsymbol{G,1}}$ is the true parameter value under H_1 and σ^2_G is the true variance of the noise. This tells us that the probability of a false alarm only depends on the threshold, but the probability of detection depends on the planet intensity. The brighter the planet is, the higher the detection probability.

4.2.2 Multi-signal detection in a co-added image

The method above detects a planet located at the center of an image window with the size of PSF's central core, i.e., the set of K test pixels. However, the number and the locations of the potential planets are unknown, so to perform detection in the whole image, I will traverse the whole image using the method. That is to say, for each pixel, I utilize the image window centered at this pixel to calculate the T value defined in Eq. 4.26. This procedure generates a T value map for the image. By comparing the T values with a chosen threshold, we get the detection result, and can

use the center of the minimum bounding circle of the detected areas as the estimated positions.

Two detection and estimation examples are presented in Figs. 4.2 and 4.3. Venus is located at pixel (7,12), and Earth at (14,9). In Fig. 4.2, the detection process is demonstrated step by step with an image with perfect starshade. In the simulated starshade image examples, I still use the Haystack model as input, but do not include the exozodiacal dust. That is to say, there are the Sun, Earth, and Venus in the images. The Sun is unnoticable due to the suppression of the starshade. Examples of an image window are also shown in Fig. 4.2(b). The white box is of the size of the PSF core. It is the image window used to calculate the T value and then decide whether there is a planet at the position of the white asterisk, i.e., pixel (7,12). The magenta box is for the magenta asterisk, i.e., pixel (8,14). Repeating the process, the T value at each pixel and thus the T value map are generated for the whole image, i.e. Fig. 4.2(c). When the pixel is at the boundary of the PSF in the image (one example is the magenta asterisk in Fig. 4.2(b)), the image window only contains part of the planet which is not centered at the pixel, so neither H_1 nor H_0 is true and the MLE of planet intensity can be negative sometimes. Thus, I set those negative estimates as zero and thus $T = 0$. I then compare each T value with the chosen threshold, and get a binary image as Fig. 4.2(e). Generally speaking, some pixels next to the signal center will also be detected. Thus, to estimate the position of the planet, I first find the convex hulls in the thresholded image and find the minimal circle bounding each convex hull. The center of the circles will be the estimates for the planets' positions, which is also demonstrated in Fig. 4.2(e). The estimated planet intensity is the MLE of α at the estimated planet position. In this work, I define Intensity Error $= \frac{(\text{Estimated Intensity} - \text{Real Intensity})}{\text{Real Intensity}}$.

In Fig. 4.3, I demonstrate the GLRT's ability to distinguish real signals from fake ones by providing the detection result for an image with a starshade with truncated

tips. This defect causes a bright spot in the image, which could be mistaken for a planet. I still use the PSF templates of the perfect starshade for this truncated starshade case, as we may not know the defect beforehand. GLRT successfully distinguishes Venus and Earth from the fake signal. The errors of intensity and position estimation for these two examples are presented in Table. 4.1. The fake signal is close to Venus, so the intensity estimation of Venus is degraded for the truncated starshade case. The pixel size of the images is 0.021 arcsec, so the position estimation is accurate to the pixel level.

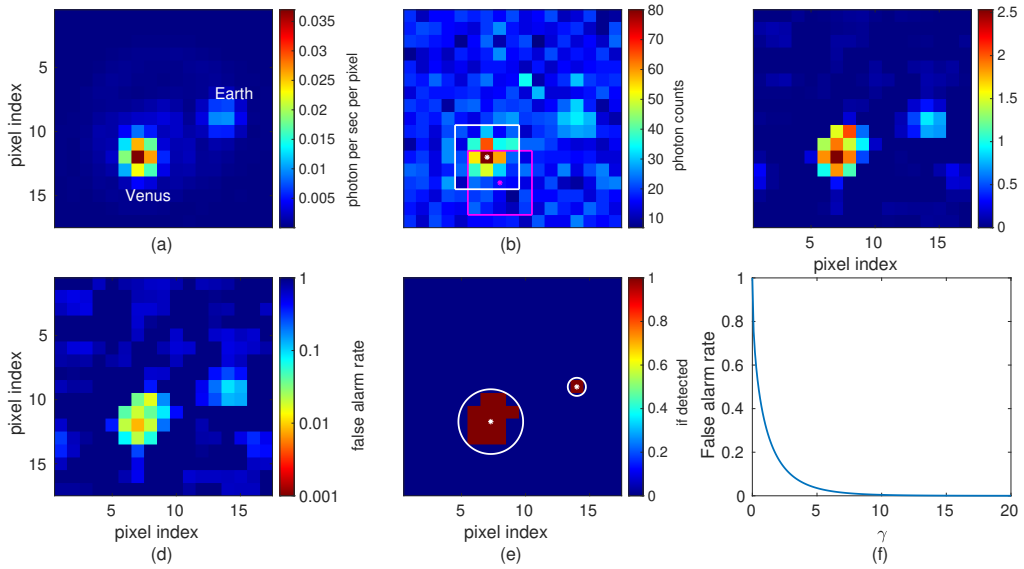

Figure 4.2: Example of the GLRT detection on an image with perfect starshade and without exozodiacal dust. (a) Noiseless image. It should be taken as the ground truth for image processing of this example. (b) A corresponding image with detector noise. Examples of image windows are also shown. The white box is centered on pixel (7,12), marked by the white asterisk. The pixel values in the box form data $\boldsymbol{x}_{7,12}$ in Eq. (4.6). The magenta box forms data $\boldsymbol{x}_{8,14}$ and is the case where the image window is at the edge of the PSF. (c) The T values from Eqs. 4.26 in each pixel. (d) False alarm rate map. (e) Binary detection image after thresholding. I apply a threshold of 0.7354 to the T map, which results in a 0.4 false alarm rate. The white circles are the minimal bounding circles used to estimate the planet's position. (f) The relationship between threshold and false alarm rate from Eqs. 4.28.

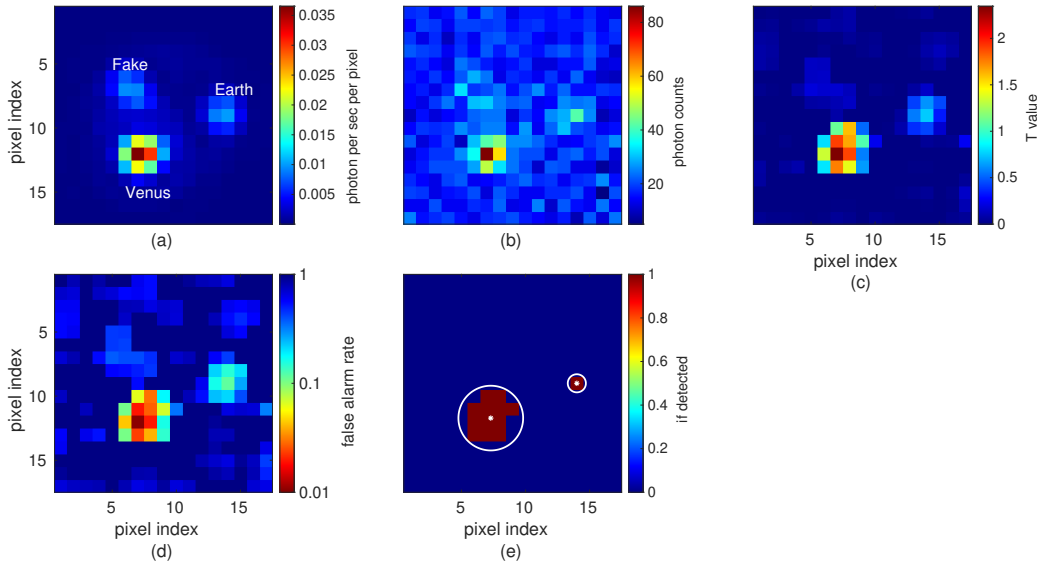

Figure 4.3: Example of the GLRT detection on an image with truncated starshade. (a) Noiseless image. The defect on the starshade causes a bright spot that resembles a fake planet. (b) Image with detector noise applied. (c) The T values from Eqs. 4.26 in each pixel. (d) False alarm rate map. (e) Binary detection image after thresholding. I apply a threshold of 0.7354 to the T map, which results in 0.4 false alarm rate. GLRT successfully detects Venus and Earth and ignores the fake signal in the image.

4.2.3 Performance analysis

To analyze the performance of the method, I also calculate the receiver operating characteristic (ROC) curves for Venus and Earth shown in Fig. 4.4, where I compare the performance of GLRT for co-added images with different numbers of total images, which is denoted as N. A ROC curve plots the relationship between true positive rate and false alarm rate for different thresholds. It illustrates the diagnostic ability of a binary classifier system as its threshold is varied.

Equation (4.28) and Equation (4.29) give the theoretical false alarm rate and true positive rate under a Gaussian assumption, and are therefore only an approximation. Moreover, as shown in Eq. (4.30), the calculation of the true positive rate needs the value of the true variance, which we need to estimate. Thus, to more accurately

Table 4.1: Intensity estimation error and position estimation error comparison between results in images using different starshades.

Starshade	Intensity Error for Venus	Intensity Error for Earth	Position Error for Venus (arcsec)	Position Error for Earth (arcsec)
Perfect starshade	1.5%	1.2%	3E-03	9.5E-03
truncated starshade	20.5%	4.1%	3E-03	9.5E-03

demonstrate the detection's performance, I use a Monte Carlo simulation. The simulated starshade images used in the calculation contains the Sun, Venus and Earth, which is the same as in Fig. 4.2. To calculate the ROC curves, I apply GLRT to get the false alarm rate map for a set of different thresholds and record if it results in detection or missed detection of Earth, Venus and a background pixel. I run a large number of trials, which is denoted as n_{trials}, and record the ratio of detection of Earth and Venus as the true positive rate for Earth and Venus, and record the ratio of detection of the background pixel as the false positive rate. The confidence interval (CI) of a proportion $\hat{p}$ is [25]:

$$\left(\hat{p} - z_{1-\eta/2}\sqrt{\frac{\hat{p}(1-\hat{p})}{n_{trials}}},\ \hat{p} + z_{1-\eta/2}\sqrt{\frac{\hat{p}(1-\hat{p})}{n_{trials}}} \right). \tag{4.31}$$

They are also the confidence interval based on Fisher information. Thus, for a point $(\hat{p}_{false}, \hat{p}_{positive})$ on a ROC curve, I take the confidence interval using the two points:

$$\left(\hat{p}_{false} - z_{1-\eta/2}\sqrt{\frac{\hat{p}_{false}(1-\hat{p}_{false})}{n_{trials}}},\ \hat{p}_{positive} + z_{1-\eta/2}\sqrt{\frac{\hat{p}_{positive}(1-\hat{p}_{positive})}{n_{trials}}} \right) \tag{4.32}$$

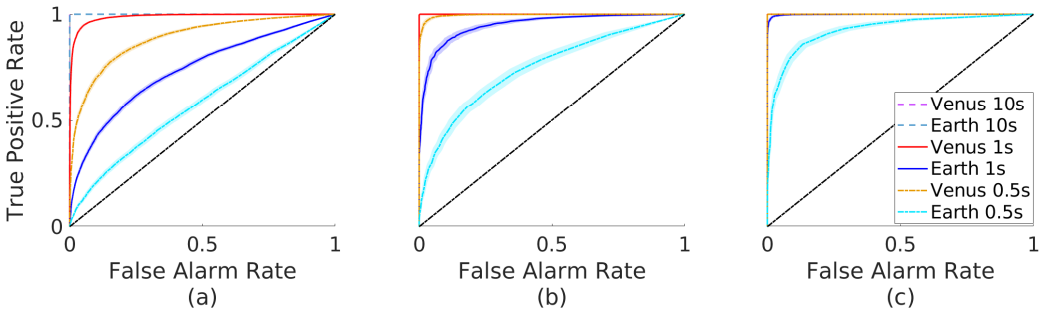

Figure 4.4: ROC with confidence intervals for Venus and Earth using GLRT with different integration time. (a) ROC for co-added images each from $N = 200$ PC images. The curves for an integration time of 10s overlaps with the plot's boundary, which indicates perfect detection performance. (b) ROC for co-added images each from $N = 700$ PC images. (c) ROC for co-added images each from $N = 2000$ PC images. The shaded region behind each ROC curve is its 95% confidence interval.

and

$$\left(\hat{p}_{false} + z_{1-\eta/2}\sqrt{\frac{\hat{p}_{false}(1-\hat{p}_{false})}{n_{trials}}},\ \hat{p}_{positive} - z_{1-\eta/2}\sqrt{\frac{\hat{p}_{positive}(1-\hat{p}_{positive})}{n_{trials}}} \right). \tag{4.33}$$

where $z_{1-\eta}/2$ is the upper critical value for the standard normal distribution with $\eta/2$ area to the right of it. For each ROC curve, I apply these two boundaries to calculate the shaded area as the confidence interval. ROC curves for Venus and Earth with different numbers of PC images to combine into one co-added image N, (with different integration times) are shown in Fig. 4.4. As can be seen, the confidence interval is tight. As Venus is brighter than Earth, the performance for Venus is better than that for Earth. Increasing the integration time has similar effect as increasing the planet intensity because both increase the expected number of photons arriving on the pixel. Moreover, the performance for both Venus and Earth is better with the more number of PC images in the co-added image.

4.2.4 Optimal number of PC images for one co-added image

As I mentioned before, the number of PC images to combine into one co-added image N, is an important hyperparameter to be chosen before doing detection via most of the methods. For example, GLRT's performances vary with the number of PC image for one co-added image, as shown in Fig. 4.4. With too small N, the true positive rate and false alarm rate for the detection may not be desirable. With too big N, precious observation time would be wasted. To choose the best N, we can utilize the ROC curves.

First, given integration time, three parameters need to be specified: the minimum planet intensity to be detected, the maximum false alarm rate that can be accepted, and the minimum true positive rate that is acceptable. Then, for a different N, the ROC is calculated via Monte Carlo simulation. Finally, the minimum N that can reach the requirements are chosen. For example, if we assume the dimmest planet has the same intensity as Earth, the maximum acceptable false alarm rate is 0.16 and the minimum acceptable true positive rate is 0.85. The acceptable false alarm rate, true positive rate pairs are in the shaded green region in Fig. 4.5. I calculate the ROCs with different N for integration time 1s and find that the ROC of $N = 700$ is the first one to reach the green region in Fig. 4.5. Thus I choose $N = 700$ as the optimal number of PC images to be co-added into the final image.

An alternative way is to specify the minimum planet intensity to be detected and the minimum area under the curve (AUC). Then, for a different N, the ROC is calculated via Monte Carlo simulation. Finally, the minimum N that can reach the requirement for AUC is chosen.

Furthermore, we can calculate ROC curves or AUC values for different 'integration time' and 'number of PC images' pairs, and using the previous two methods to find the best pair that has the minimum total observation time.

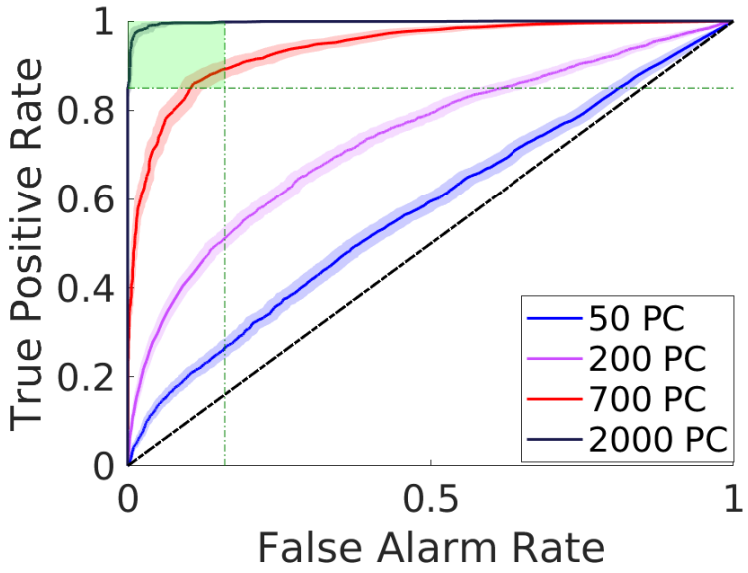

Figure 4.5: ROC with confidence interval for Earth using GLRT with different N. The horizontal green dotted line is the acceptable true positive rate (TP) and the vertical one is the acceptable false alarm rate (FA) region. Thus, the acceptable true TP and acceptable FA region is the shaded green area. The ROC with $N = 700$ is the first ROC reaching the acceptable region.

4.2.5 Iterative generalized likelihood ratio test for exozodiacal dust

Exozodiacal dust is debris in the habitable zones of stars believed to come from extrasolar asteroids and comets[85]. Though the true structure of exozodiacal dust is unknown, as a first attempt, I simply assume it is axisymmetric, which is believed to be a reasonable approximation for small dust grains [62]. The exozodiacal dust can degrade the detection and estimation. When the intensity of exozodiacal dust is similar to that of a target planet, the methods mentioned previously have difficulty detecting the planet's signal. For example, if we directly apply the GLRT method for co-added images introduced in Sec. 4.2 for Fig. 3.15(d), we get a confusing false alarm rate map in Fig. 4.6(a); it is hard to distinguish Earth from the exozodiacal dust. I develop here an iterative GLRT to tackle this problem. It is essentially an Expectation-Maximization (EM) algorithm[27]. The planets' signals and the exozodi-

acal dust are both unknown and need to be estimated. However, it is hard to estimate them accurately at the same time, and their estimation can influence each other. The solution is to iteratively estimate either the planets' signal or the exozodiacal dust first, and then use the estimation as a known factor to estimate the other until both estimates converge.

Similar to Sec.4.2, I work on the co-added image. Then, the model for a whole co-added image with exozodiacal dust is

$$\widetilde{\boldsymbol{M}}(x,y) = \sum_{i=1}^{N_x}\sum_{j=1}^{N_y}[\alpha_{i,j}\boldsymbol{X}_{i,j}(x,y)] + \boldsymbol{b}(x,y) + \boldsymbol{d}(x,y) + \boldsymbol{\omega}(x,y)\,, \tag{4.34}$$

where $\widetilde{\boldsymbol{M}}$ is a whole co-added image (compared with $\boldsymbol{M}$, a whole noiseless image; $\boldsymbol{Y}$, the image window on a co-added image.); $\alpha_{i,j}$ is the intensity of the point source located at (i,j); $\boldsymbol{X}_{i,j}$ is the co-added PSF located at (i,j) (compared with $\boldsymbol{x}_{i,j}$, noiseless PSF); $\boldsymbol{d}$ is the exozodiacal dust, which is also unknown; $\boldsymbol{b}$ is the background light from sources other than the exozodiacal dust; $\boldsymbol{\omega}$ is the noise; (x,y) denotes functions of position (x,y) (compared with functions of radius r later).

Though we only have N_xN_y data points (photon counts in each pixel), we have $3N_xN_y + N_x^2N_y^2$ unknown parameters (signal intensity, background intensity, dust intensity and covariance matrix of noise). To reduce the number of unknowns, I assume that the dust is nearly axisymmetric, which may be a reasonable approximation for small dust grains [62]. Thus,

$$\widetilde{\boldsymbol{M}}(x,y) = \sum_{i=1}^{N_x}\sum_{j=1}^{N_y}[\alpha_{i,j}\boldsymbol{X}_{i,j}(x,y)] + \boldsymbol{b}(x,y) + \boldsymbol{d}(r) + \boldsymbol{\omega}(x,y)\,, \tag{4.35}$$

where $r = \sqrt{x^2+y^2}$. Then optimization equation for parameter estimation becomes

$$\min_{\boldsymbol{\alpha},\boldsymbol{b},\boldsymbol{d}} ||\widetilde{\boldsymbol{M}} - \sum_{i=1}^{N_x}\sum_{j=1}^{N_y}[\alpha_{i,j}\boldsymbol{X}_{i,j}] - \boldsymbol{b} - \boldsymbol{d}||_2\,. \tag{4.36}$$

We can not directly split the whole image into smaller areas and do detection separately like Eq. (4.13) as the estimation of dust in one area also depends on other areas at the same radii from the center. To tackle this, I split the estimation of signals and exozodiacal dust into two steps. First, I take the median of the values for each radius to estimate the dust. I use the median rather than mean to avoid the influence of the existence of planet signals at some radius (an example is shown in Fig. 4.6(b)). This is equivalent to solving the optimization problem for each r:

$$\boldsymbol{d}^*(r) = \underset{\boldsymbol{d}(r)}{\operatorname{argmin}} ||\widetilde{\boldsymbol{M}}(r) - \boldsymbol{d}(r)||_1 \,. \tag{4.37}$$

The $*$ denotes the estimate of the corresponding parameter. Then, I subtract the estimated exozodiacal dust from the co-added image,

$$\widetilde{\boldsymbol{M_b}} = \widetilde{\boldsymbol{M}} - \boldsymbol{d}^*(r)\,, \tag{4.38}$$

so the resulting $\widetilde{\boldsymbol{M_b}}$ should be the signals and background sources without exozodiacal dust. An example is shown in Fig. 4.6(c). Now, we can use the technique introduced in Sec. 4.2. Applying GLRT on this image $\widetilde{\boldsymbol{M_b}}$ produces the T value map in Fig. 4.6(d) and provides an estimation of the planets' positions and intensities, as shown in Fig. 4.6(e). The estimated planets are subtracted to get a better estimation of the background, as shown in Fig. 4.6(f) and the process is repeated iteratively. The procedure is summarized in Fig. 4.7 and the complete example is shown in Fig. 4.6. In Table 4.2, I summarize the intensity and position estimation error for the example. The ROC curves are shown in Fig. 4.8. The performance is undermined a little by the dust, compared to that without dust.

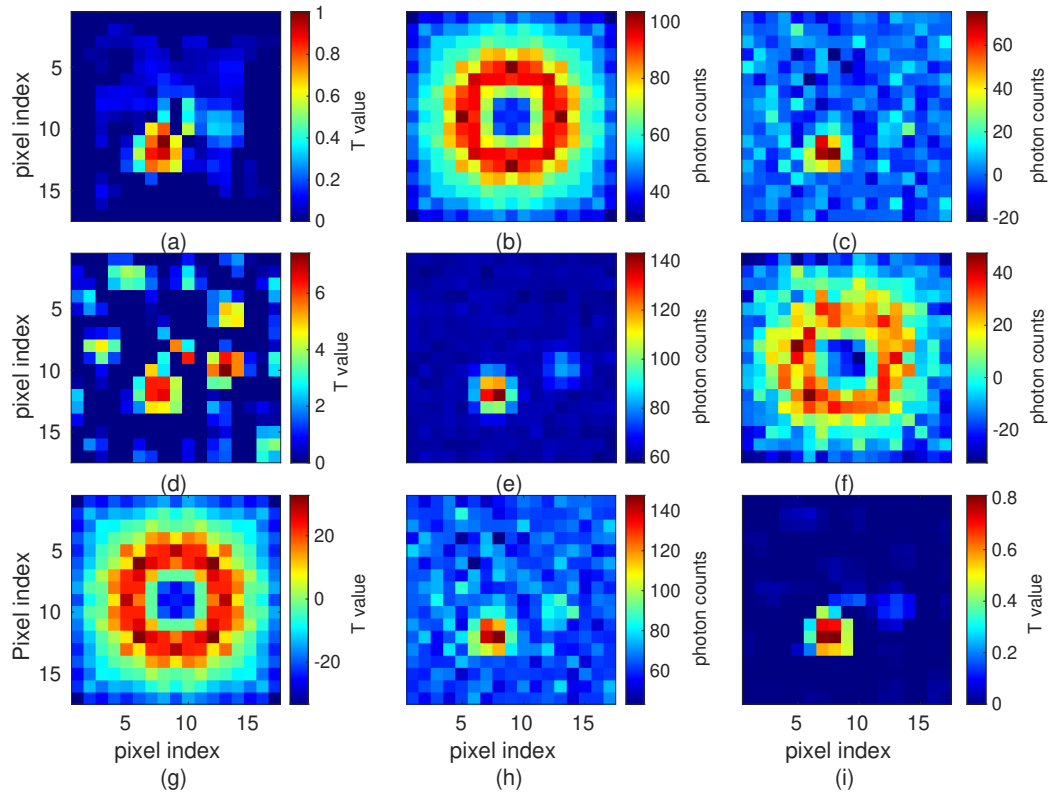

Figure 4.6: Example of iterative GLRT applied to Fig. 3.15(d). (a) T value map for Fig. 3.15(d). (b) The median value for each radius of Fig. 3.15(d), i.e., the exozodiacal dust estimation $\boldsymbol{d}^*$ at initial step. (c) The residual $\widetilde{\boldsymbol{M_b}}$ after subtracting $\boldsymbol{d}^*$ from $\boldsymbol{I}$, i.e., the residual after subtracting (b) from Fig. 3.15(d). It is the initial estimation for the underlying image with only planets. (d) T map for (c). (e) The new estimate of planets $\sum_{i=1}^{N_x}\sum_{j=1}^{N_y}[\alpha_{i,j}\boldsymbol{P}_{i,j}(x,y)]$. After applying GLRT on (c) and get detection, I also obtained the intensity and position estimation of the planets. (f) Exozodiacal dust I_p after subtracting estimated planet signals (e) from the original image Fig. 3.15(d). (g) The dust estimation at the final step. (h) The final residual $\widetilde{\boldsymbol{M_b}}$, i.e., the residual after subtracting (g) from Fig. 3.15(d). It is the final estimation for the underlying image with only planets. (i) T value map for (h).

4.3 Bernoulli generalized likelihood ratio test for photon-counting images

The previous section approximated the noise in co-added images by a Gaussian distribution. In this section, we directly use the detector's probability function derived in

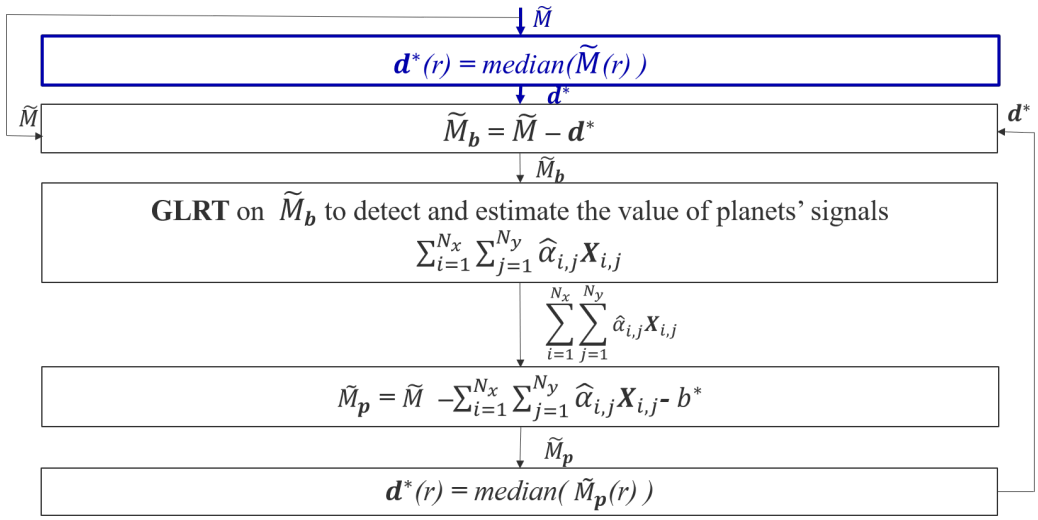

Figure 4.7: The flow chart describes the process of iterative GLRT. The blue box is the initialization step.

Table 4.2: Intensity and position estimation error for Fig. 3.3(f) via iterative GLRT methods

Planet	Intensity Error	Position Error
Venus	-5.9%	21 milli-arcsec
Earth	-38.3%	30 milli-arcsec

Sec. 3.5, which does not rely on a large number of PC images for co-added images. As a result, measurements in each pixel in each PC image follow a Bernoulli distribution.

4.3.1 Detection for an image window

Signal estimation

As in Sec. 4.2.1, we examine an image window that is the size of the PSF's central core (the main part of a signal). We will explain how to apply the method on the whole image, which is normally larger than the PSF core, in Sec. 4.3.2.

We begin with the simple model of the signal received by the detector. Given the PSF shape, $\boldsymbol{x} = (x_1, \cdots, x_K)^T$, the conditional probability of the n-th PC image,

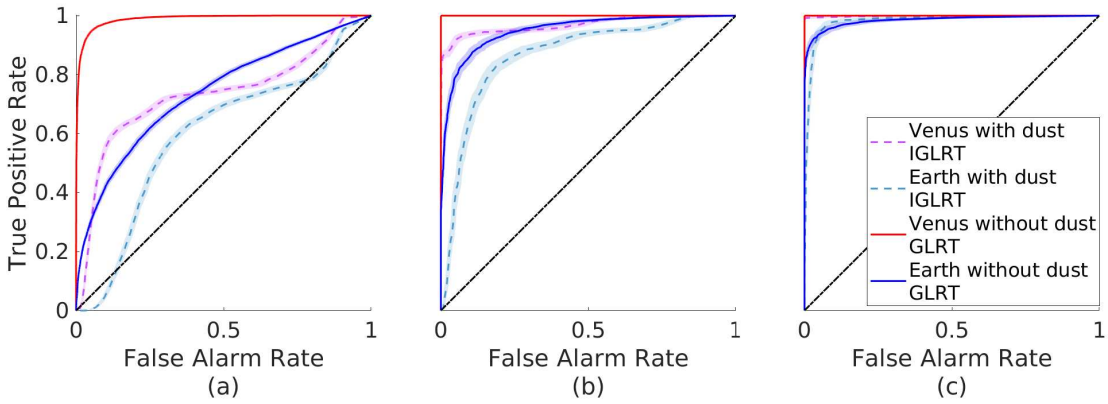

Figure 4.8: The ROCs for the iterative GLRT with 1s integration time. The ROCs without dust with 1s integration time from Fig. 4.4 are added here for reference. (a) ROC for co-added images each from $N = 200$ PC images. (b) ROC for co-added images each from $N = 700$ PC images. (c) ROC for co-added images each from $N = 2000$ PC images.

$\boldsymbol{y}_n = (y_{n,1}, ..., y_{n,K})^T$, is

$$p(\boldsymbol{y}_n|\alpha, \beta) = \prod_{k=1}^{K} [1 - f(\alpha x_k + \beta)]^{1-y_{n,k}} f(\alpha x_k + \beta)^{y_{n,k}}, \tag{4.39}$$

where the function $f(\cdot)$ is the probability function of detecting a one value in Eq. (3.5). The measurement in each pixel satisfies a Bernoulli distribution, and $[1 - f(\alpha x_k + \beta)]^{1-y_{n,k}} f(\alpha x_k + \beta)^{y_{n,k}}$ is the probability for the measurement in the k-th pixel (for PC images, the measurement is either one or zero). The probability for the whole image is simply the product of the probability of every measurement. The interesting part

is that the probabilities in different pixels are correlated because of the underlying signal model in Eq. 4.2.

Furthermore, the conditional probability of N images, $\boldsymbol{y} = \{\boldsymbol{y}_1, \cdots, \boldsymbol{y}_N\}$, can be written as

$$\begin{aligned} L_B(\boldsymbol{\theta_B}) &= p(\boldsymbol{y}|\alpha, \beta) \\ &= \prod_{n=1}^{N} p(\boldsymbol{y}_n|\alpha, \beta) \\ &= \prod_{n=1}^{N}\prod_{k=1}^{K}[1 - f(\alpha x_k + \beta)]^{1-y_{n,k}} f(\alpha x_k + \beta)^{y_{n,k}} \\ &= \prod_{k=1}^{K}[1 - f(\alpha x_k + \beta)]^{N-\sum_{n=1}^{N} y_{n,k}} f(\alpha x_k + \beta)^{\sum_{n=1}^{N} y_{n,k}} \\ &= \prod_{k=1}^{K}[1 - f(\alpha x_k + \beta)]^{N_{0,k}} f(\alpha x_k + \beta)^{N_{1,k}}, \end{aligned} \tag{4.40}$$

where $\boldsymbol{\theta_B}$ is the simpler vector representation for the two unknown parameters $\binom{\alpha}{\beta}$, $N_{0,k} = N - \sum_{n=1}^{N} y_{n,k}$ and $N_{1,k} = \sum_{n=1}^{N} y_{n,k}$ respectively represent the frequency of zero and one occurring in N measurements of the k-th pixel. The equality $N = N_{0,k} + N_{1,k}$ holds for every pixel. As the data $\boldsymbol{y}$ is known and the parameters $\boldsymbol{\theta_B}$ are unknown, this probability function is a likelihood function for the unknown parameters (so it is also denoted as $L_B(\boldsymbol{\theta_B})$ above, where the subscript B means Bernoulli distribution).

Taking the natural logarithm of both sides of Eq. (4.40), the log-likelihood of the series of measurements is

$$l_B(\boldsymbol{\theta_B}) = ln(L_B(\boldsymbol{\theta_B})) = \sum_{k=1}^{K} N_{0,k} ln[1 - f(\alpha x_k + \beta)] + N_{1,k} ln[f(\alpha x_k + \beta)]. \tag{4.41}$$

To estimate α and β, we can conduct a MLE based on Eq. (4.41) by taking the derivatives with respect to α and β and setting them equal to zero,

$$\begin{aligned}\frac{\partial l_B}{\partial \alpha} &= K\sum_{n=1}^{N} U_n f'(\alpha U_n+\beta)\frac{K_{1,n}-Kf(\alpha U_n+\beta)}{Nf(\alpha U_n+\beta)[1-f(\alpha U_n+\beta)]}=0,\\ \frac{\partial l_B}{\partial \beta} &= K\sum_{n=1}^{N} f'(\alpha U_n+\beta)\frac{K_{1,n}-Kf(\alpha U_n+\beta)}{Kf(\alpha U_n+\beta)[1-f(\alpha U_n+\beta)]}=0,\end{aligned} \tag{4.42}$$

where $f'(s)=\frac{df(s)}{ds}$. These equations can be solved for estimates of α and β using a gradient descent method. We denote the solution as $\hat{\boldsymbol{\theta}}_{B,1}=(\hat{\alpha}_{B,1},\hat{\beta}_{B,1})^T$. As can be seen, the derivatives are weighted summations of the difference between the measurements and the distribution means, where $Kf(\cdot)$ and $Kf(\cdot)[1-f(\cdot)]$ are, respectively, the mean and variance (the series of measurements follows a Binomial distribution, since each measurement satisfies a Bernoulli distribution). According to Fig. 3.13(b), the function $f'(s)$ is zero when $s\to+\infty$. That means that the method neglects the difference between different intensities that are too large in the estimation since the photon counting detector always gives 1 in these cases.

When solving for the MLE of β under H_0, we have an additional constrain $\alpha=0$. That is to say, we solve

$$\frac{\partial l_B}{\partial \beta} = K\sum_{n=1}^{N} f'(\beta)\frac{K_{1,n}-Kf(\beta)}{Kf(\beta)[1-f(\beta)]}=0\,, \tag{4.43}$$

We denote estimation as $\hat{\beta}_{B,0}$.

For this model, the Fisher information matrix is

$$\begin{aligned}\boldsymbol{I_B}(\boldsymbol{\theta_B}) &= \mathrm{Var}_{\boldsymbol{\theta_B}}\{\nabla l_B(\boldsymbol{\theta_B})\}\\ &= -E_{\boldsymbol{\theta_B}}\{\nabla^2 l_B(\boldsymbol{\theta_B})\},\end{aligned} \tag{4.44}$$

and

$$\nabla^2 l_B(\boldsymbol{\theta_B}) = \begin{bmatrix} N\sum_{k=1}^{K} x_k^2 g & N\sum_{k=1}^{K} x_k g \\ N\sum_{k=1}^{K} x_k g & N\sum_{k=1}^{K} g \end{bmatrix}, \tag{4.45}$$

and

$$g = \frac{1}{Nf^2(1-f)^2}\Big\{-N_{1,k}ff' + (N+N_{1,k})f^2f' - Nf^3f' - Nff'^2 + \dots \\ \cdots + Nf^2f'^2 + N_{1,k}ff'' - (N+N_{1,k})f^2f'' + Nf^3f''\Big\}. \tag{4.46}$$

For simpler notation, here f is $f(\alpha x_k + \beta)$; f' is $f'(\alpha x_k + \beta)$; f'' is $f''(\alpha x_k + \beta)$ and $f''(s) = \frac{d^2 f(s)}{d^2 s}$

With the Fisher information matrix, we can also derive the confidence intervals for the MLE[44]:

$$\hat{\alpha} \pm z\sqrt{(\boldsymbol{I_B}(\hat{\boldsymbol{\theta}}_{B,1})^{-1})_{11}}, \tag{4.47}$$

and

$$\hat{\beta} \pm z\sqrt{(\boldsymbol{I_B}(\hat{\boldsymbol{\theta}}_{B,1})^{-1})_{22}}, \tag{4.48}$$

where z is the appropriate critical value (for example, 1.96 for 95 % confidence), and the notation $(\boldsymbol{I_B}(\hat{\boldsymbol{\theta}}_{B,1})^{-1})_{ii}$ means that we invert the Fisher information matrix first, and then take the ii component of the inverted matrix.

Signal detection

The detection of an exoplanet signal is considered as a composite hypotheses testing problem in the thesis. Due to the lack of prior knowledge of the parameters, similar to the previous section, we can conduct a generalized likelihood ratio test, i.e., we

determine whether there is an exoplanet signal based on the ratio

$$\begin{aligned} R_B &= \frac{max_{\alpha,\beta}\ p_1(\boldsymbol{y}|\alpha,\beta)}{max_{\alpha,\beta}\ p_0(\boldsymbol{y}|\alpha,\beta)} \\ &= \frac{max_{\alpha,\beta}\ \prod_{k=1}^{K} f(\alpha x_k+\beta)^{N_{1,k}}[1-f(\alpha x_k+\beta)]^{N_{0,k}}}{max_{\beta}\ \prod_{k=1}^{K} f(\beta)^{N_{1,k}}[1-f(\beta)]^{N_{0,k}}} \\ &= \frac{\prod_{k=1}^{K} f(\hat{\alpha_1} x_k+\hat{\beta}_1)^{N_{1,k}}[1-f(\hat{\alpha_1} x_k+\hat{\beta}_1)]^{N_{0,k}}}{\prod_{k=1}^{K} f(\hat{\beta}_0)^{N_{1,k}}[1-f(\hat{\beta}_0)]^{N_{0,k}}}, \end{aligned} \tag{4.49}$$

where $p_0(\cdot)$ and $p_1(\cdot)$ are the probability under hypotheses H_0 and H_1, respectively, and the two maximal probabilities and the corresponding parameters (α and β) are calculated using the estimation algorithm mentioned above. R is the generalized likelihood ratio.

For easier calculation, we usually take the log of R, that is the log likelihood ratio. Therefore the log-likelihood ratio is

$$\begin{aligned} r_B = \sum_{k=1}^{K} & N_{0,k} ln[1-f(\hat{\alpha}_{B,1} x_k+\hat{\beta}_{B,1})] + N_{1,k} ln[f(\hat{\alpha}_{B,1} x_k+\hat{\beta}_{B,1})] \\ & - N_{0,k} ln[1-f(\hat{\beta}_{B,0})] + N_{1,k} ln[f(\hat{\beta}_{B,0})]\,. \end{aligned} \tag{4.50}$$

In a real space mission, we can conduct sequential detection while sequentially collecting images. After receiving every new image, we update the test ratio in Eq. (4.49); when $r_B \geq \pi_U$ or $r_B \leq \pi_L$, we conclude H_1 or H_0 is accepted and stop taking new images, otherwise we take a new image and repeat the detection procedure, where π_U and π_L are thresholds chosen beforehand.

The thresholds can be determined according to users' desired true positive and false alarm rates. According to Wilks' theorem, the probability distribution of $2R_B$ under H_0, i.e., twice the ratio, is approximately a chi-squared distribution with one degree of freedom[110]. There is no simple closed-form theoretical solution for the true positive rate and false alarm rate given a threshold for this model, so we numerically calculate them via Monte Carlo simulation. Given a planet intensity users want to

detect and the number of PC images that they plan to take, they can numerically compute the true positive and false alarm rate for each threshold using this detection algorithm. They can choose a desirable true positive and false alarm rate value pair and thus its corresponding threshold. Details on choosing the appropriate threshold are given in Sec. 4.4

We simulate a signal (signal only) with intensity 1e-8 Jy (for reference, Venus is 2.99e-8 Jy and Earth is 4.85e-9 Jy if viewed from 10 pc at 0.552 µm) and run multiple trials to get the statistics of the method's performance, shown in Fig. 4.9. The Bernoulli GLRT method correctly estimates the intensity of the signal quickly. The value of the log-likelihood ratio is high and increases quickly with the increasing number of observations. This means that it is possible to confidently detect the existence of a signal with just a few images and the more observations the larger the gain in confidence for the detection.

4.3.2 Multi-signal detection in an image

The method described in the Sec. 4.3.1 is for an image window with K pixels. In reality, an image much bigger than the size of a core will be examined for an unknown number of planets in an unspecified location. Thus, the detection procedure is repeated for each set of K pixels across the whole image. This generates a log-likelihood ratio map for the image. The process is the same as described in Sec. 4.2.2 but using the new method in each image window. We also demonstrate the performance of the sequential GLRT detection method on simulated starshade images.

Though the method is applied to each PC image separately rather than on a co-added image, there is insufficient space to show all PC images one-by-one here. Thus, to give readers a sense of what the data look like, the co-added images are shown in Figs. 4.10 (a), (b) and (c). Their corresponding log-likelihood ratio maps given by Bernoulli GLRT are shown in Figs. 4.10 (d), (e) and (f). To decide the exact position

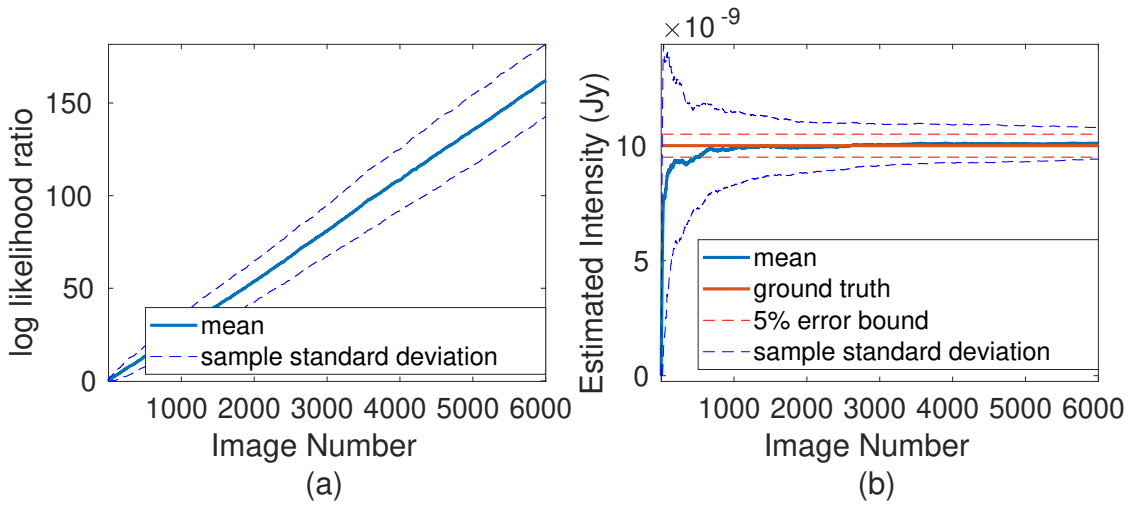

Figure 4.9: Statistics of the maximum likelihood planet intensity estimation from 100 trials. The blue solid line is the average of all trials with an increasing number of observations and the blue dashed lines are the sample standard deviation band. (a) The log-likelihood ratio with an increasing number of observations. The more images that are available, the bigger the log-likelihood ratio is. Thus, the greater the confidence of the existence of a true signal. (b) The estimated intensity with the increasing number of images. The red solid line is the true intensity. The red dashed lines are the 5% error band. The blue dashed line is the standard deviation band. The method results in a good estimate.

of the signal, after thresholding the log-likelihood map, we will just choose the center of the detected area's circumscribed circle as the position of the planet. An example is shown in Fig. 4.11. My method detects the existence of the signals quickly and separates them from the background successfully. The more observations, the larger the gain in confidence for the detection.

The changes of log-likelihood ratio at Venus, Earth and a background pixel at (5,5) after each observation are shown in Fig. 4.12. As the figures demonstrate, my method can detect the existence of the signals quickly and separate them from the background successfully.

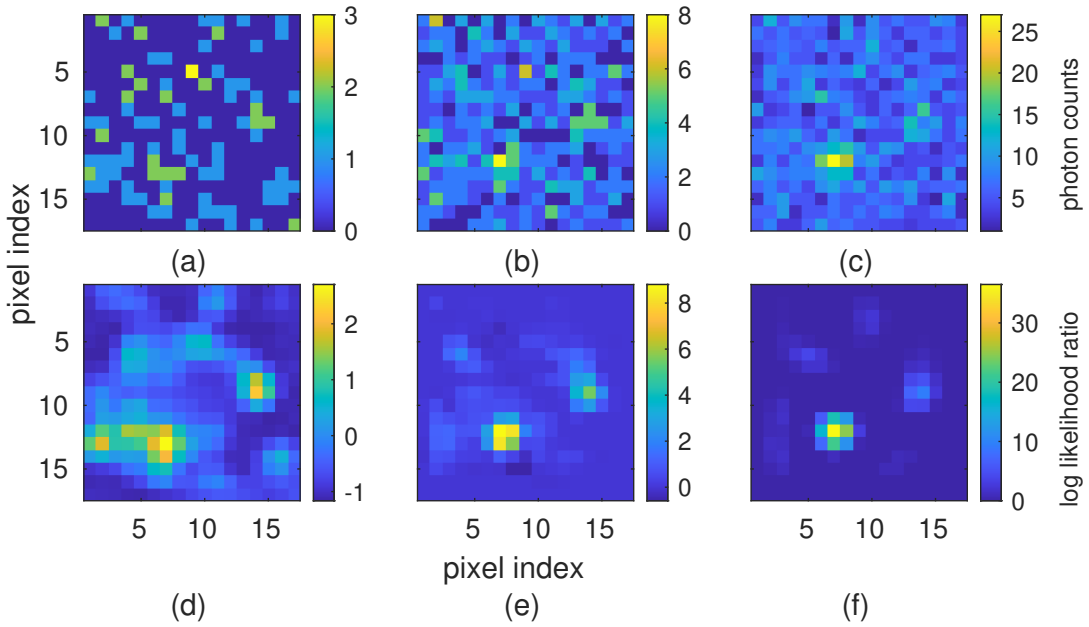

Figure 4.10: Results of the new Bernoulli GLRT. (a) Co-added image with 50 sequential PC images for Fig.4.2(a). (b) Co-added image with 200 sequential PC images for Fig.4.2(a). (c) Co-added image with 700 sequential PC images for Fig.4.2(a). (d) Log likelihood ratio of each pixel using the 50 sequential PC images in Fig.4.10(a). (e) Log likelihood ratio of each pixel using the 200 sequential PC images in Fig.4.10(c). (f) Log likelihood ratio of each pixel using the 700 sequential PC images in Fig.4.10(e). The change of Log likelihood ratio of Venus, Earth and a background pixel with increasing number of observations is shown in Fig 4.12.

4.3.3 Early stopping for observation when no planets exists

As shown in the previous examples, the Bernoulli GLRT successfully detects a planet even for short integration times. Another important problem is to know when to stop when no detection is made so time wasted on a system with no planet is minimized. As no closed-form analytical solution for Bernoulli GLRT can be derived among false alarm rate and intensity and number of PC images, which will define the total time needed, it is impossible to solve for the time needed to reach a specific false alarm rate given the planet intensity via inverting a function. Instead, I will rely on numerical calculation via Monte Carlo simulation.

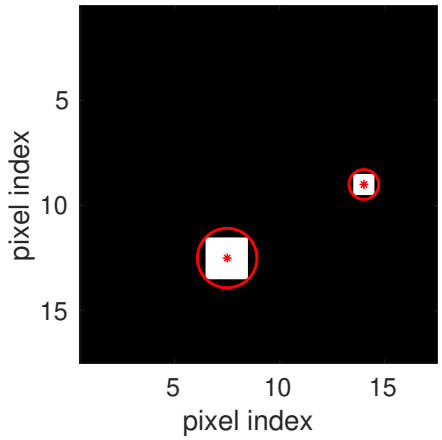

Figure 4.11: Example of position estimation. Binary detection image after thresholding the log-likelihood ratio map in Fig. 4.10(e) with a threshold of 5 . The red circles are the minimal bounding circles of the detected area. The centers of the circles can be used to estimate the planet positions.

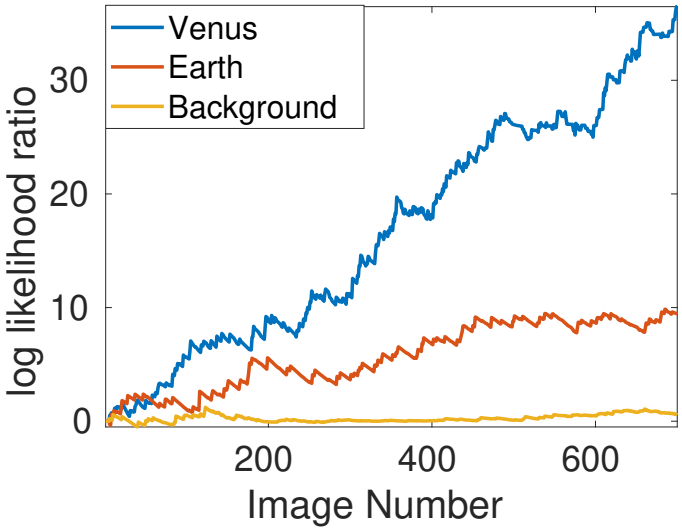

Figure 4.12: Log likelihood ratio of Venus, Earth and a background pixel at (5,5) with increasing number of observations for Fig.4.2(a) using Bernoulli GLRT.

The procedure is the same as choosing the optimal number of PC images for a co-added image in Sec. 4.2.4. First, three parameters are specified: the minimum planet intensity to be detected, the maximum false alarm rate that can be accepted, and the minimum true positive rate that is acceptable. Then, for a different number

of images, the ROC is calculated via Monte Carlo simulation. Finally, the minimum number of PC images that can reach the requirements are chosen. For example, if we assume the dimmest planet has the same intensity as Earth, the maximum acceptable false alarm rate is 0.16 and the minimum acceptable true positive rate is 0.85. The acceptable false alarm rate, true positive rate pairs are in the shaded green region in Fig. 4.13. I calculate the ROCs with different numbers of PC images and find that the 200 PC images' ROC is the first one to reach the green region, as shown in Fig. 4.13. Thus, after taking 200 PC images and if there is still no signal detected, the telescope system could move on to observing another target star with confidence there is no planet. For the same three parameters chosen, we need 700 PC images for the Gaussian method as shown in Sec. 4.2.4, which is more than 2 times of the number for the Bernoulli method. This demonstrates the Bernoulli model utilizes the information more efficiently than the Gaussian model.

4.4 Comparison of methods

We have introduced a GLRT method that was applied to co-added images generated from the combination of many frames. That method assumed the values in each pixel followed a Gaussian distribution, so the summation of frames was necessary in order to build enough signal in each pixel for the Gaussian assumption to be valid. I then introduced an alternative: the Bernoulli distribution in the new SGLRT method works for single PC images, which makes it easier to use online as it can process even a few PC images.

The underlying relationship between the probability in the Bernoulli distribution and flux intensity can be derived theoretically based on the detector model or directly measured in an experiment. No approximation is used and thus the method is accurate and efficient at extracting information. In Figs. 4.14 (a),(b) and (c) I show the T

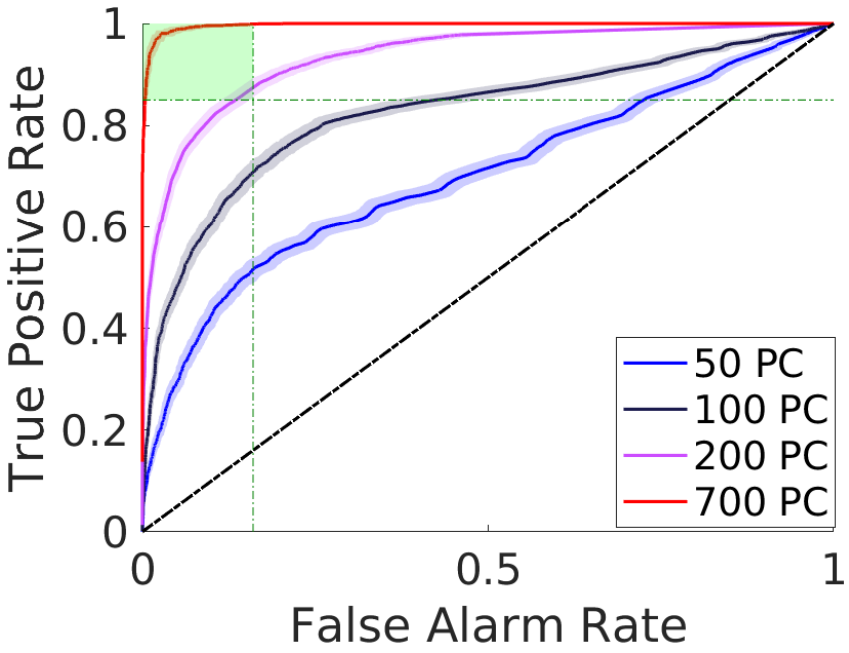

Figure 4.13: ROC curves with confidence intervals for Earth using Bernoulli GLRT with different number of PC images. The horizontal green dotted line is the acceptable true positive rate (TP) and the vertical one is the acceptable false alarm rate (FA) region. Thus, the acceptable true TP and acceptable FA region is the shaded green area. The ROC curves with 200 PC is the first ROC reaching the acceptable region.

map using the Gaussian GLRT for the co-added images of Fig. 4.10. As the T value defined in Eq. 4.26 is a proxy for the log-likelihood ratio that is easier to compute, the absolute value of T should not be compared with the log-likelihood ratio directly. Instead, attention should be paid to the relative difference of T values between the signals and the background. Fig. 4.14 shows that the T map is noisier than the log-likelihood map from the Bernoulli GLRT. The corresponding false alarm rate for the T value of Venus and Earth for the three cases are in table 4.3. We generally have higher confidence using Bernoulli GLRT.

The above comparison indicates that the Bernoulli model for PC images contributes to the performance improvement. To further analyze the contribution from GLRT, we also compared the Bernoulli GLRT with the performance of detection based on SNR from our Bernoulli model. With the MLE of signal intensity and esti-

mated standard deviation of the MLE derived from the Fisher information matrix in Sec. 4.3.1, we define their ratio as the SNR from our model. We will refer to this SNR definition as Bernoulli SNR (BSNR). For each pixel, we utilize the image window centered at it and calculate the estimated signal intensity and the standard deviation. Then, we calculate the ratio. After repeating the process for all the pixels in the image, we obtain a BSNR map. The BSNR maps for the three example co-added images in Fig. 4.10 are shown in Fig. 4.15 to help visually compare the performance with the BGLRT method.

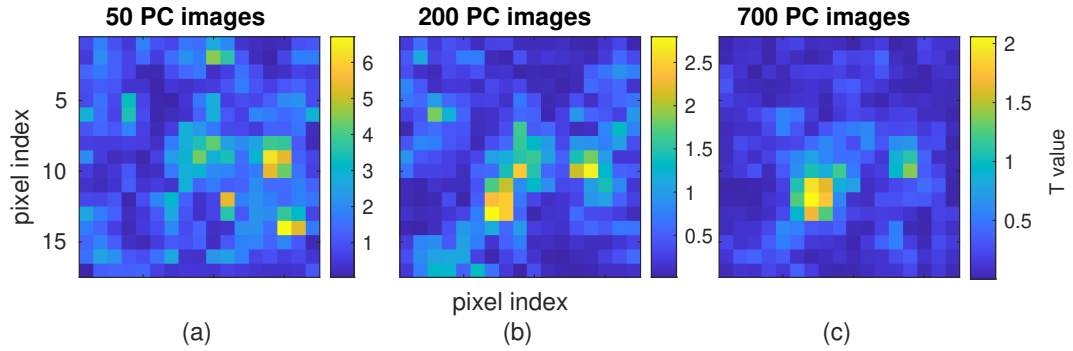

Figure 4.14: Results of a Gaussian based GLRT for images in Fig.4.10. (a) T value of each pixel for the co-added image with 50 sequential PC images for Fig.4.10(a). (b) T value of each pixel for the co-added image with 200 sequential PC images for Fig.4.10(b). (c) T value of each pixel for the co-added image with 700 sequential PC images for Fig.4.10(c).

Table 4.3: False alarm rate (FA) for the cases in Fig. 4.10 using Bernoulli GLRT (BGLRT) and Gaussian GLRT (GGLRT)

Case	Venus BGLRT	Venus GGLRT	Earth BGLRT	Earth GGLRT
Fig. 4.10(a)	0.326	0.655	0.076	0.110
Fig. 4.10(b)	0.000	0.002	2.000e-04	0.004
Fig. 4.10(c)	0.000	0.000	0.000	0.000

I also compared the Bernoulli GLRT with the performance of the detection method based on the SNR map implemented in pyKLIP[108]. For each pixel, the algorithm

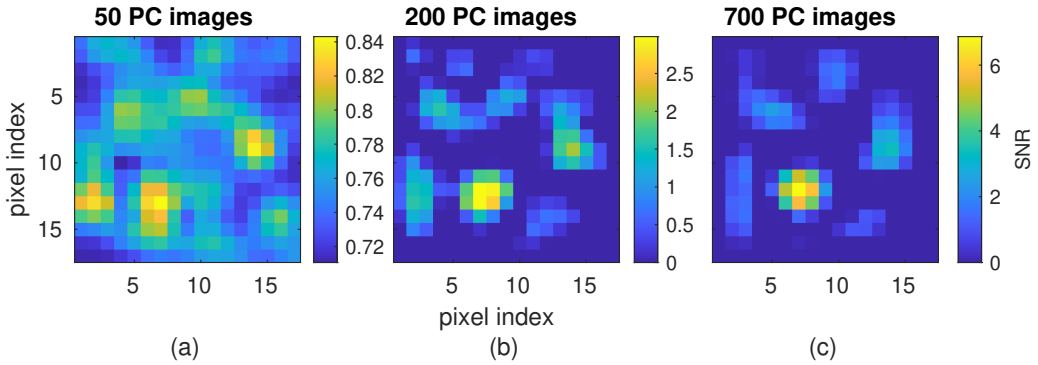

Figure 4.15: The SNR map based on the Bernoulli model for images in Fig. 4.10. (a) The SNR map of each pixel for the co-added image with 50 sequential PC images for Fig. 4.10(a). (b) The SNR map of each pixel for the co-added image with 200 sequential PC images for Fig. 4.10(b). (c) The SNR map of each pixel for the co-added image with 700 sequential PC images for Fig. 4.10(c).

masks its surrounding pixels within the signal area in question (I chose the size of signal area as the size of PSF core) and then computes the standard deviation using the rest of pixels in concentric annuli. The ratio of the pixel value and this standard deviation as SNR value at this pixel. The width of the annuli used is the diameter of the PSF core in this paper. Repeating the process for all the pixels in the image generates a SNR map. The SNR maps for the three example co-added images in Fig. 4.10 are shown in Fig. 4.16 to help visually compare the performance with the GLRT methods.

To further demonstrate the different properties of the methods, I compare their ROC curves for the detection of Venus and Earth. It is difficult to analytically derive a closed-form relationship between the false alarm rate and true positive rate and the threshold chosen in the new Bernoulli GLRT, unlike my previous GLRT, which assumes Gaussian noise. Thus, I use Monte Carlo simulations, using multiple thresholds for each simulation, to calculate the ROC curves, shown in Fig. 4.17. The simulated starshade images used in the calculation contains the Sun, Venus and Earth,

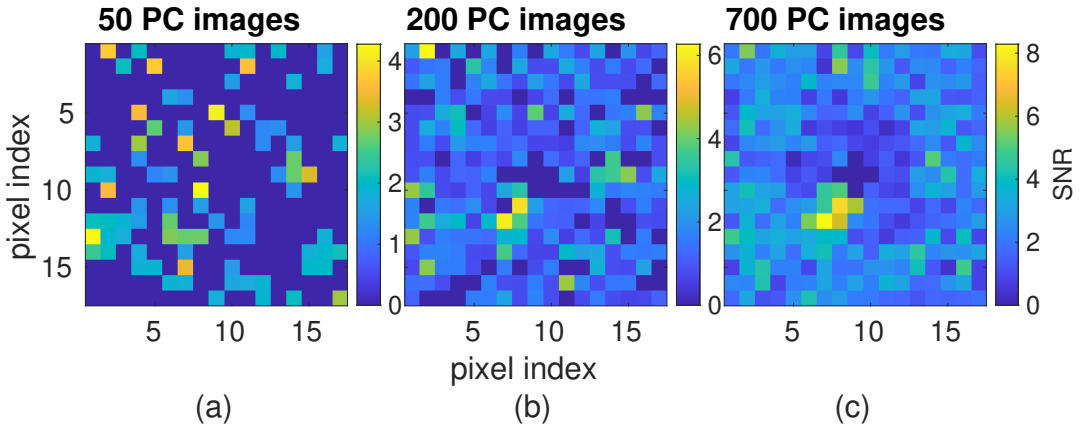

Figure 4.16: The SNR map from the pyKLIP package[108] for images in Fig.4.10. (a) SNR of each pixel for the co-added image with 50 sequential PC images as shown in Fig.4.10(a). (b) SNR of each pixel for the co-added image with 200 sequential PC images as shown in Fig.4.10(b). (c) SNR of each pixel for the co-added image with 700 sequential PC images as shown in Fig.4.10(c).

which is the same as in Fig. 4.2(a) (and thus Fig. 4.2(b) is a concrete example used in Monte Carlo simulations). I compare the performance of the methods using different numbers of total images N. I apply the Bernoulli GLRT on the set of images and obtain the log-likelihood ratio map; I also apply the Gaussian GLRT to get the false alarm rate map. We also apply Bernoulli SNR and SNR from pyKLIP on the images. I apply a set of different thresholds with the resulting detection or missed detection of Earth, Venus and a background pixel. I run a large number of trials, which is denoted as n_{trials}, and record the ratio of detection of Earth and Venus as the true positive rate for Earth and Venus, and record the ratio of detection of the background pixel as the false positive rate. The confidence interval of a proportion $\hat{p}$ is given by eqs. (4.32) and (4.33). For each ROC curve, we also calculate the confidence interval shown as the shaded areas in Fig. 4.17. The confidence interval is standard Monte Carlo statistics, which is detailed in the Appendix. As can be seen in Fig. 4.17, the confidence interval is tight.

For Fig. 4.17(a), I ran 5000 trials with 50 PC images generated for Venus and Earth in each trial. The Bernoulli GLRT and Bernoulli SNR were applied to the 50 PC images sequentially; the Gaussian GLRT and SNR from pyKLIP were applied to the co-added image of the 50 PC images. Results for different decision thresholds were recorded and combined into the ROC curve. For Fig. 4.17(b), I ran 5000 trials and 200 PC images for each trial. For Fig. 4.17(c), I ran 2000 trials and 700 PC images for each trial. The performance for Venus is better than Earth when I use the same method and the same number of PC images. One reason is that Venus is brighter than Earth. Moreover, Venus is further away from the star at the center, so the influence from the residual starlight is smaller compared to that for Earth. The performance for both Venus and Earth using either method is better with more images. It is easy to understand that the method performs better with more information, i.e., more images. Furthermore, the Bernoulli GLRT outperforms my previous method. ROC curves using the SNR map are also calculated, shown in Fig. 4.17. The calculation uses the same set of images as the ones used for all three methods. Generally speaking, the Bernoulli GLRT also outperforms the other methods.

For easier comparison, I also list the area under the ROC curve (AUC) for all the curves in Table. 4.4. AUC is an aggregate measure of performance across all possible thresholds. It can be interpreted as the probability that the model ranks a random positive example higher than a random negative example. AUC is 1 if the model's decisions are all correct and 0 if all wrong. More comparisons of GLRT with Gaussian assumption and the SNR method can be found in my other work[52]. Overall, Bernoulli GLRT outperforms GLRT with Gaussian assumption and the SNR method.

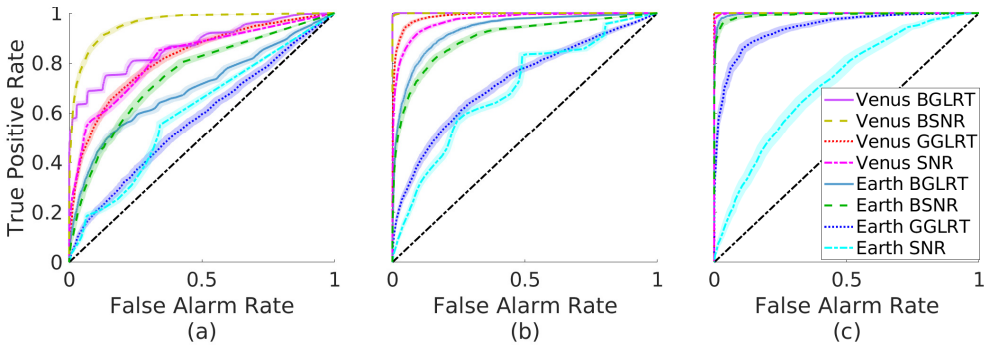

Figure 4.17: Receiver operating characteristic curves with confidence interval for Earth and Venus detection with the four different methods. 'BGLRT' means the result used the Bernoulli GLRT, which processes each PC images sequentially using the GLRT based on a Bernoulli distribution. 'BSNR' means the detection method based on our Bernoulli SNR, which utilizes the final MLEs from our Bernoulli model and estimated standard deviation from Fisher information matrix. 'GGLRT' in the legends means the result used the Gaussian GLRT, which processes co-added images and assumes Gaussian noise. 'SNR' means the detection method based on SNR implemented in pyklip, which is applied to co-added images . The shaded region behind each ROC curve is its 95% confidence interval. (a) ROC curves using 50 PC images calculated from 5000 trials. (b) ROC curves using 200 PC images calculated from 5000 trials. (c) ROC curves using 700 PC images calculated from 2000 trials.

Table 4.4: Comparison of area under the curve (AUC) for BGLRT, BSNR, GGLRT and SNR method from pyKLIP[108].

	Venus BGLRT	Venus BSNR	Venus GGLRT	Venus SNR	Earth BGLRT	Earth BSNR	Earth GGLRT	Earth SNR
50PC	0.8697	0.9594	0.8205	0.8224	0.6991	0.7488	0.5753	0.5991
200PC	0.9999	0.9996	0.9878	0.9714	0.9392	0.9002	0.7245	0.6953
700PC	1	1	1	0.9993	0.9970	0.9920	0.9401	0.7159

Chapter 5

Conclusion and future work

5.1 Conclusion

In this thesis, I describe my process for simulating realistic starshade images and preliminary study of signal detection and estimation in starshade images, which no previous work has looked into.

Realistic starshade image simulation is an important and necessary first step for performance validation and testing image processing and signal detection methods for starshades. I demonstrate my ability to generate realistic starshade images. I include factors such as real scale, astronomical scene, starshade manufacturing and deployment errors, and the special detector model: PC mode using EMCCD. I introduce the concept of ROI, which helps speed up the simulation process. From the simulation results, we know that even small shape defects on a starshade may result in confusing bright spots similar to planets.

With the starshade images, we are able to investigate signal detection and estimation. Previous work on PC image processing for the most part only uses co-added PC images, so I also start with a detection method for a co-added image. The core detection and estimation part is done by GLRT under the assumption of Gaussian

noise. First, estimates of unknown parameters are obtained by QMLE. Then, the T value, a proxy of the likelihood ratio which is easier to compute, with respect to estimated parameters is calculated. After comparing the T with a chosen threshold, we get the detection results. For cases with exozodiacal dust, I split the process into two parts: dust estimation and signal estimation and use GLRT iteratively. The GLRT method successfully and efficiently flags potential planets with a concrete false alarm rate. It can help distinguish planet signals from artifacts caused by small starshade shape errors, such as a truncated petal tip. In addition, I provide guidance to choose the best number of PC images to combine into one co-added image. It utilizes the ROC curves and will help utilize the observation time efficiently.

Due to the limitation of a Gaussian as an approximation for the noise distribution in the image, Gaussian GLRT introduces detection performance improvement but not drastically, compared to the SNR method commonly used in high-contrast imaging. Therefore, I introduce an improved version of the GLRT method based on a detector model for individual PC images rather than an approximation, which more accurately represents the noise characteristics and improves the detection performance. This method directly works with each PC image, so there is no need to choose the number of PC images to combine into one co-added image. I showed that such a method outperforms our GLRT method for co-added images under a Gaussian noise assumption, and the SNR method commonly used in high-contrast imaging. We also compare the BGLRT with the BSNR, which also uses the estimation results from our Bernoulli model. The BGLRT and the BSNR have similar performance (The BGLRT is a little better in most cases) and are better than other methods, which indicates the performance gain in detection is mostly the result of improved model for the imaging process. Furthermore, this method also provides the maximum likelihood estimate of exoplanet intensity and background intensity. This approach maximizes the utilization of information presented in each observation. I applied this method to simulated

starshade images and successfully detected the existing planets. Directly processing the PC images online helps allocate the observation time efficiently. We can compare the log-likelihood ratio with thresholds chosen beforehand after each observation and stop accordingly. As we can decide the existence or lack of a planet efficiently in this way, we can move to other planetary systems if there is no planet or make sure that enough information is gathered if there is a planet. Besides the observation time, the analysis of detection performance introduced could also give quantitative guidance on the choice of imaging parameters, such as the threshold of the PC mode. Similar to GLRT under the Gaussian assumption, we can also use BGLRT iteratively to deal with the dust.

The two models and detection methods (the Gaussian model for co-added images and the resulting GLRT, and the Bernoulli model for PC images and the resulting GLRT) are general models and detection methods that can be significantly expanded for different applications. The likelihoods in different pixels are related by the underlying template for signals we want to detect, i.e., a PSF template plus constant background as in Eq. 4.2 in my work. Thus, the resulting GLRT decides whether such a template exists in the observed area. However, this is just one particular application example of the model and the method. By replacing the signal template, different forms of signals can be chosen to appropriately match the observation scenario; the remaining steps in the derivation and the application of the two detection methods are the same. Possible applications include signal detection in PC images from ground-based telescopes and medical imaging. In this work, I present the iterative GLRT assuming face-on, uniform exozodiacal dust, but the same concept can be applied to more detailed models of the dust structure or other global features in the image.

5.2 Future Work

First, the methods introduced in this work assume non-overlapping signals. When two signals overlap, the light distribution in the image window centered on the signals will be distorted. This violates the hypothesis that the image area contains a PSF-shaped signal and constant background. Therefore, the estimation and detection performance may be influenced. If there is not too much overlap, the intensity estimate for both signals will be higher than the true values and the position estimate will biased towards each other. If the signals are close enough, the algorithm may consider them as one signal. Future work can look into solving this problem by expanding the image area and modeling overlapping signals. Moreover, astronomers can take another set of images after a while, because the signals' relative positions are likely to change and will separate.

Second, this work presents two cases of the background: locally constant background and axisymmetric dust. In the case of non-uniform background, the algorithm's performance depends on how well we know the non-uniform background. The current algorithm finds the signal looking like the PSF template against the uniform background in an image window of the size as PSF core. We traverse the whole image by checking the PSF-core-sized area one by one. Thus, the assumption of the algorithm is that the background is locally constant but can be non-uniform in the whole image. If the non-uniform background changes slowly spatially, a locally constant background may still be a good approximation and the detection will not be influenced much. If we have zero knowledge about the distribution of the bright background close to the planets, the results are affected by the distorted signal. However, if we have some knowledge about the nonuniform background, we can accommodate it in the model. For example, it is a reasonable approximation to assume the face-on exozodiacal light is axisymmetric, which is discussed in Sec. 4.2.5.

Third, in this work, due to the short time needed to take enough images, I assume that the positions of the light sources are fixed. Future work can include the dynamics of the planetary system. It can be useful for investigating follow-up observations to confirm the detection.

Fourth, when experimental images of sub-scale starshades with different light sources are available, we can test the methods on the experimental data.

Future work can be done to further improve the methods performance. First, post-processing may improve the performance. This thesis tests all the methods on raw images without post-processing. How various post-processing techniques influence the detection and estimation deserves detailed investigation. Second, the performance of the detection methods can be further improved if we have prior knowledge about the probability distribution of the planets' intensity, which may be available after future exoplanet surveys.

Bibliography

[1] C. Aime, R. Soummer, C. Marois, R. Doyon, D Nadeau, R. Racine, and G. A. H. Walker. Effects of quasi-static aberrations in faint companion searches. *European Astronomical Society Publications Series*, 8:233–243, 2003.

[2] Guillem Anglada-Escudé, Pedro J Amado, John Barnes, Zaira M Berdiñas, R Paul Butler, Gavin AL Coleman, Ignacio de La Cueva, Stefan Dreizler, Michael Endl, Benjamin Giesers, et al. A terrestrial planet candidate in a temperate orbit around proxima centauri. *Nature*, 536(7617):437–440, 2016.

[3] A. Aspect. From huygens' waves to einstein's photons: Weird light. *Comptes Rendus Physique*, 18(9-10):498–503, 2017.

[4] B. Beky. *Development and Application of Tools to Characterize Transiting Astrophysical Systems*. PhD thesis, Harvard University, Cambridge, Massachusetts, 2014.

[5] M. Bottom, S. Martin, C. Seubert, E. Cady, S.K. Zareh, and S. Shaklan. Precise starshade stationkeeping and pointing with a zernike wavefront sensor. In *International Society for Optics and Photonics*, volume 10400 of *Techniques and Instrumentation for Detection of Exoplanet*, page 104001B, 2017.

[6] I. Braems and N. J. Kasdin. Bayesian hypothesis testing for planet detection. *arXiv*, 2004.

[7] D. Briot and J. Schneider. Prehistory of transit searches. In H.J. Deeg and J.A. Belmonte, editors, *Handbook of Exoplanets*, pages 35–49. Springer, 2018.

[8] E. Cady. *Design, Tolerancing, and Experimental Verification of Occulters for Finding Extrasolar Planets*. PhD thesis, Princeton University, Princeton (NJ), 2010.

[9] E. Cady, K. Balasubramanian, M. Carr, M. Dickie, P. Echternach, J. Kasdin, S. Shaklan, D. Sirbu, and V. White. Broadband suppression and occulter position sensing at the princeton occulter testbed. In *International Society for Optics and Photonics*, volume 7731 of *Space Telescopes and Instrumentation 2016: Optical, Infrared, and Millimeter Wave*, page 99043I, 2010.

[10] F. Cantalloube, D. Mouillet, L.M. Mugnier, J. Milli, O. Absil, C.G. Gonzalez, G. Chauvin, J.L. Beuzit, and A. Cornia. Direct exoplanet detection and characterization using the ANDROMEDA method: Performance on VLT/NaCo data. *Astronomy & Astrophysics*, 582:A89, 2015.

[11] A. Carlotti, N.J. Kasdin, R.J. Vanderbei, and A. Riggs. Hybrid coronagraphic design: optimization of complex apodizers. In *Techniques and Instrumentation for Detection of Exoplanets VI*, volume 8864 of *International Society for Optics and Photonics*, page 88641Q, 2013.

[12] A. Carlotti, R.J. Vanderbei, and N.J. Kasdin. Optimal pupil apodizations of arbitrary apertures for high-contrast imaging. *Optics Express*, 19(27):26796–26809, 2011.

[13] S. Casement, S. Warwick, D. Smith, S. Ellis, and J. Stover. Results of edge scatter testing for a starshade mission. In *Optical, Infrared, and Millimeter Wave*, volume 9904 of *Space Telescopes and Instrumentation*, page 99043H, 2016.

[14] W. Cash. Detection of Earth-like planets around nearby stars using a petal-shaped occulter. *Nature*, 442(7098):51 – 53, Jul. 2006. [doi:10.1038/nature04930].

[15] W. Cash, S. Kendrick, C. Noecker, J. Bally, J. DeMarines, J. Green, P. Oakley, A. Shipley, S. Benson, S. Oleson, and D. Content. The new worlds observer: the astrophysics strategic mission concept study. In *In UV/Optical/IR Space Telescopes: Innovative Technologies and Concepts IV*, volume 7436 of *International Society for Optics and Photonics*, page 743606, 2009.

[16] G. Chauvin, A.M. Lagrange, C. Dumas, B. Zuckerman, D. Mouillet, I. Song, J.L. Beuzit, and P. Lowrance. A giant planet candidate near a young brown dwarf-direct vlt/naco observations using ir wavefront sensing. *Astronomy & Astrophysics*, 425:L29–L32, 2004.

[17] R. Claudi. The direct imaging method. In V. Bozza, L. Mancini, and A. Sozzetti, editors, *Methods of detecting exoplanets*, pages 181–242. Springer, 2018.

[18] J.L. Codona, M.A. Kenworthy, P.M. Hinz, J. Angela, and N. Woolf. A high-contrast coronagraph for the MMT using phase apodization: design and observations at 5 microns and 2 λ/D radius. In *Ground-based and Airborne Instrumentation for Astronomy*, volume 6269 of *International Society for Optics and Photonics*, page 62691N, 2006.

[19] Craig J Copi and Glenn D Starkman. The big occulting steerable satellite (boss). *The Astrophysical Journal*, 532(1):581, 2000.

[20] D. R. Cox and N. Reid. A note on pseudolikelihood constructed from marginal densities. *Biometrika*, 91:729–737, 2004.

[21] C.H. Dahlqvist, F. Cantalloube, and O. Absil. Regime-switching model detection map for direct exoplanet detection in ADI sequences. *Astronomy & Astrophysics*, 633:A95, 2020.

[22] O. Daigle, C. Carignan, J.L. Gach, C. Guillaume, S. Lessard, Fortin C.A, and S. Blais-Ouellette. Extreme faint flux imaging with an emccd. *Publications of the Astronomical Society of the Pacific*, 121(882):866, 2009.

[23] O. Daigle, O. Djazovski, D. Laurin, R. Doyon, and E. Artigau. Characterization results of emccds for extreme low-light imaging. *Proc. SPIE*, 8453:845303, 2012.

[24] Mario Damasso, Fabio Del Sordo, Guillem Anglada-Escudé, Paolo Giacobbe, Alessandro Sozzetti, Alessandro Morbidelli, Grzegorz Pojmanski, Domenico Barbato, R Paul Butler, Hugh RA Jones, et al. A low-mass planet candidate orbiting proxima centauri at a distance of 1.5 au. *Science advances*, 6(3):eaax7467, 2020.

[25] Joaquim P. Marques de Sá. *Applied Statistics Using SPSS, STATISTICA, MATLAB and R*, pages 92–93. Springer, 2007.

[26] G. A. de Vree, A. H. Westra, I. Moody, F. van der Have, K. M. Ligtvoet, and F.J. Beekman. Photon-counting gamma camera based on an electron-multiplying ccd. *IEEE Transactions on Nuclear Science*, 52(3):580–588, 2005.

[27] A.P. Dempster, N.M. Laird, and D.B. Rubin. Maximum likelihood from incomplete data via the EM algorithm. *Journal of the Royal Statistical Society: Series B (Methodological)*, 39:1–22, 1977.

[28] M. C. DeSantis, S. H. DeCenzo, S. H. Li, and Y. M. Wang. Precision analysis for standard deviation measurements of immobile single fluorescent molecule images. *Optics Express*, 18(7):6563–6576, 2010.

[29] C. Ducourant, R. Teixeira, G. Chauvin, G. Daigne, J.F. Le Campion, I. Song, and B. Zuckerman. An accurate distance to 2m1207ab. *Astronomy & Astrophysics*, 477(1):L1–L4, 2008.

[30] EXOPLANET EXPLORATION: astrometry. `https://exoplanets.nasa.gov/alien-worlds/ways-to-find-a-planet/#/5`. Accessed: 2020-12-08.

[31] EXOPLANET EXPLORATION: gravitational microlensing. `https://exoplanets.nasa.gov/alien-worlds/ways-to-find-a-planet/#/4`. Accessed: 2020-12-08.

[32] EXOPLANET EXPLORATION: transit. `https://exoplanets.nasa.gov/alien-worlds/ways-to-find-a-planet/#/2`. Accessed: 2020-12-08.

[33] O. Flasseur, L. Denis, E. Thiébaut, and M. Langlois. An unsupervised patch-based approach for exoplanet detection by direct imaging. *25th IEEE International Conference on Image Processing*, pages 2735–2739, 2018.

[34] T. Glassman, S. Warwick, A. Lo, and S. Casement. Starshade starlight-suppression performance with a deployable structure. In *Optical, Infrared, and Millimeter Wave*, volume 9904 of *Space Telescopes and Instrumentation*, page 990425, 2016.

[35] C.A.G. Gonzalez, O. Absil, and M. Van Droogenbroeck. Supervised detection of exoplanets in high-contrast imaging sequences. *A&A*, 613, 2018.

[36] C.A.G. Gonzalez, O. Wertz, O. Absil, V. Christiaens, D. Defrère, D. Mawet, J. Milli, P.A. Absil, M. Van Droogenbroeck, F. Cantalloube, and P.M. Hinz. Vip: Vortex image processing package for high-contrast direct imaging. *The Astronomical Journal*, 154(1):7, 2017.

[37] J. W. Goodman. *Introduction to Fourier Optics*. The McGraw-Hill companies, 2004.

[38] T.D. Groff, A. Riggs, B. Kern, and N.J. Kasdin. Methods and limitations of focal plane sensing, estimation, and control in high-contrast imaging. *Journal of Astronomical Telescopes, Instruments, and Systems*, 2(1):011009, 2015.

[39] L. K. Harding, R. Demers, M. E. Hoenk, P. Peddada, B. Nemati, M. Cherng, D. Michaels, L. S. Neat, A. Loc, N. L. Bush, and D. J Hall. Technology advancement of the ccd201-20 emccd for the wfirst coronagraph instrument: sensor characterization and radiation damage. *JATIS*, 2(1):011007, 2015.

[40] A. Harness. *High Contrast Astronomy with Starshades*. PhD thesis, University of Colorado, Boulder, CO, 2016.

[41] A. Harness, N.J. Kasdin, M. Galvin, S. Shaklan, K. Balasubramanian, V. White, K. Yee, R. Muller, P. Dumont, S. Vuong, and P. Willems. Starshade technology development activity milestone 1a: Demonstration of high contrast in monochromatic light at a flight-like fresnel number. *Jet Propulsion Laboratory Publications*, 2019.

[42] A. Harness, S. Warwick, A. Shipley, and W. Cash. Ground-based testing and demonstrations of starshades. In *International Society for Optics and Photonics*, volume 9904 of *Space Telescopes and Instrumentation 2016: Optical, Infrared, and Millimeter Wave*, page 99043I, 2016.

[43] K. B. W. Harpsøe, M. I. Andersen, and P. Kjægaard. Bayesian photon counting with electron-multiplying charge coupled devices (emccds). *Astronomy & Astrophysics*, 537:A50, 2012.

[44] T. Hastie, R. Tibshirani, and J. Friedman. *The Elements of Statistical Learning*, pages 111–156. Springer, 2009.

[45] A.P. Hatzes. The radial velocity method for the detection of exoplanets. In V. Bozza, L. Mancini, and A. Sozzetti, editors, *Methods of detecting exoplanets*, pages 3–86. Springer, 2018.

[46] J.J. Hermes. Timing by stellar pulsations as an exoplanet discovery method. *arXiv*, page 1708.00896, 2017.

[47] S. Hildebrandt and M. Turnbull S. Shaklan, E. Cady. SISTER: Starshade imaging simulation toolkit for exoplanet reconnaissance. *Journal of Astronomical Telescopes, Instruments, and Systems*, 7(2), 2021.

[48] M. Hirsch, R.J. Wareham, M.L. Martin-Fernandez, M.P. Hobson, and D.J. Rolfe. A stochastic model for electron multiplication charge-coupled devices – from theory to practice. *PLoS One*, 8(1), 2013.

[49] M.J. Holman1 and N.W. Murray. The use of transit timing to detect extrasolar planets with masses as small as earth. *Science*, 307(5713):1288–1291, 2005.

[50] M. Hu, A. Harness, and N.J. Kasdin. Image processing methods for exoplanets detection and characterization in starshade observations. In *Space Telescopes and Instrumentation 2018: Optical, Infrared, and Millimeter Wave*, volume 10698, page 106985K, Jul. 2018.

[51] M. Hu, A. Harness, Y. Kim, N.J. Kasdin, R. Vanderbei, M.J. Rizzo, and A. Roberge. Simulation of realistic images for starshade missions. In *Techniques and Instrumentation for Detection of Exoplanets VIII*, volume 10400, page 104001S, Sep. 2017.

[52] M. Hu, A. Harness, H. Sun, and N. J. Kasdin. Exoplanet detection in starshade images. *Journal of Astronomical Telescopes, Instruments, and Systems*, 7(2), 2021.

[53] M. Hu, H. Sun, A. Harness, and N.J. Kasdin. Bernoulli generalized likelihood ratio test for signal detection from photon counting images. *Journal of Astronomical Telescopes, Instruments, and Systems*, Accepted in 2021.

[54] M. Hu, H. Sun, and N.J. Kasdin. Sequential generalized likelihood ratio test for planet detection with photon-counting mode. In *Techniques and Instrumentation for Detection of Exoplanets IX*, volume 11117, page 111171k, Sep. 2019.

[55] P.G.J. Irwin. Detection methods and properties of known exoplanets. In J.W. Mason, editor, *Exoplanets*, pages 1–20. Springer, 2008.

[56] L. Kaltenegger and F. Selsis. Esa white paper: atmospheric modeling: setting biomarkers in context. *arXiv*, page 0809.4042, 2008.

[57] N.J. Kasdin. THEIA: Telescope for Habitable Exoplanets and Interstellar/Intergalactic Astronomy. *White Paper Submitted to NRC ASTRO-2010 Survey.*

[58] N.J. Kasdin and I. Braems. Linear and Bayesian planet detection algorithms for the terrestrial planet finder. *the astrophysical journal*, 646(2):1260, 2006.

[59] N.J. Kasdin, R.J. Vanderbei, D.M. Spergel, and M.G. Littman. Extrasolar planet finding via optimal apodized-pupil and shaped-pupil coronagraphs. *The Astrophysical Journal*, 582(2):1147, 2003.

[60] S.M. Kay. *Fundamentals of statistical signal processing*, volume v.1 : Estimation theory. Prentice Hall, Upper Saddle River, NJ, 1993.

[61] Y. Kim, A. Harness, D. Sirbu, M. Hu, M. Galvin, N.J. Kasdin, R.J. Vanderbei, and S. Shaklan. Optical demonstration of a starshade at flight fresnel numbers. In *International Society for Optics and Photonics*, volume 10400 of *Techniques and Instrumentation for Detection of Exoplanet*, page 104001A, 2017.

[62] M.J. Kuchner and C.C. Stark. Collisional grooming models of the Kuiper Belt dust cloud. *The Astrophysical Journal*, 140(4):1007, 2010.

[63] M.J. Kuchner and W.A. Traub. A coronagraph with a band-limited mask for finding terrestrial planets. *The Astrophysical Journal*, 570(2):900–908, 2002.

[64] D. Lafreniere, C. Marois, R. Doyon, D. Nadeau, and E. Artigau. A new algorithm for point-spread function subtraction in high-contrast imaging: a demonstration with angular differential imaging. *The Astrophysical Journal*, 660(1):770, 2007.

[65] E. Lantz, J. L. Blanchet, L. Furfaro, and F. Devaux. Multi-imaging and bayesian estimation for photon counting with emccds. *Monthly Notices of the Royal Astronomical Society*, 386:2262–2270, 2008.

[66] B. Lyot. The study of the solar corona and prominences without eclipses. *Monthly Notices of the Royal Astronomical Society*, 99:580, 1939.

[67] C. Mackay, T. Staley, D. King, F. Suess, and K. Weller. High-speed, photon-counting ccd cameras for astronomy. *Proc. SPIE*, 7742:774202, 2010.

[68] C. Marchal. Concept of a space telescope able to see the planets and even the satellites around the nearest stars. *Acta Astronautica*, 12:195–201, 1985.

[69] C. Marois, R. Doyon, D. Nadeau, R. Racine, M. Riopel, P. Vallée, and D. Lafrenière. Trident: An infrared differential imaging camera optimized for the detection of methanated substellar companions. *PASP*, 117:745, 2005.

[70] C. Marois, D. Lafreniere, R. Doyon, B. Macintosh, and D. Nadeau. Angular differential imaging: A powerful high-contrast imaging technique. *The Astrophysical Journal*, 641(1):556, 2006.

[71] T. R. Marsh. *High-speed optical spectroscopy*, pages 75–94. Springer, 2008.

[72] S.R. Martin, S. Shaklan, S. Crawford, S.C. Lee, B. Khayatian, D. Hoppe, E. Cady, and P.D. Lisman. Starshade optical edge modeling, requirements, and laboratory tests. In *Techniques and Instrumentation for Detection of Exoplanets VI*, volume 8864, page 88641G, Sep. 2013.

[73] D. Mawet, J. Milli, Z. Wahhaj, D. Pelat, O. Absil, C. Delacroix, A. Boccaletti, M. Kasper, M. Kenworthy, C. Marois, and B. Mennesson. Fundamental limitations of high contrast imaging set by small sample statistics. *The Astrophysical Journal*, 792(2):97, 2014.

[74] Maximum likelihood estimation in a Gaussian regression model. `http://sia.webpopix.org/regressionML.html#the-fim-for-a-regression-model`. Accessed: 2021-1-23.

[75] M. Mayor and D. Queloz. A Jupiter-mass companion to a solar-type star. *Nature*, 378(65555):355–359, 1995.

[76] NASA exoplanet archive: confirmed planets. `https://exoplanetarchive.ipac.caltech.edu/docs/counts_detail.html`. Accessed: 2020-12-10.

[77] B. Pairet, F. Cantalloube, C.A. Gomez Gonzalez, O. Absil, and L. Jacques. STIM map: detection map for exoplanets imaging beyond asymptotic gaussian residual speckle noise. *Monthly Notices of the Royal Astronomical Society*, 487(2):2262–2277, 2019.

[78] L.M. Palacios, A. Harness, and N.J. Kasdin. Hardware-in-the-loop testing of formation flying control and sensing algorithms for starshade missions. *Acta Astronautica*, 171:97–105, 2020.

[79] M. Perryman. Cambridge University Press, 2011.

[80] T. Plakhotnik, A. Chennu, and A. V. Zvyagin. Statistics of single-electron signals in electron-multiplying charge-coupled devices. *IEEE Transactions on Electron Devices*, 53(4):618–622, 2006.

[81] L. Pueyo, N. Zimmerman, M. Bolcar, T. Groff, C. Stark, G. Ruane, J. Jewell, R. Soummer, K.St. Laurent, J. Wang, D. Redding, J. Mazoyer, K. Fogarty, R. Juanola-Parramon, S. Domagal-Goldman, A. Roberge, O. Guyon, and A. Mandell. The LUVOIR Architecture "A" coronagraph instrument. In *UV/Optical/IR Space Telescopes and Instruments: Innovative Technologies and Concepts VIII*, volume 10398, page 103980F, Sept. 2017.

[82] D. Redding, K. Coste, O. Polanco, C. Pineda, K. Hurd, H. Tseng, S. Martin, R. Morgan, K. Schulz, J. Tesch, and E. Cady. A Habitable Exoplanet Observatory (HabEx) starshade-only architectures. In *UV/Optical/IR Space Telescopes and Instruments: Innovative Technologies and Concepts IX*, volume 111115, page 1111150V, Sep. 2019.

[83] A. Riggs. *Integrated Wavefront Correction and Bias Estimation for the High-Contrast Imaging of Exoplanets*. PhD thesis, Princeton University, Princeton, NJ, 2016.

[84] M. J. Rizzo, T.D. Groff, N.T. Zimmermann, Q. Gong, A.M. Mandell, P. Saxena, M.W. McElwain, A. Roberge, J. Krist, A.E. Riggs, and E.J. Cady. Simulating the WFIRST coronagraph integral field spectrograph. *Techniques and Instrumentation for Detection of Exoplanets VIII*, 10400:104000B, 2017.

[85] A. Roberge, C.H. Chen, R. Millan-Gabet, A.J. Weinberger, P.M. Hinz, K.R. Stapelfeldt, O. Absil, M.J. Kuchner, and G. Bryden. The exozodiacal dust problem for direct observations of exo-Earths. *Publications of the Astronomical Society of the Pacific*, 124(918):799, 2012.

[86] A. Roberge, M.J. Rizzo, A.P. Lincowski, G.N. Arney, C.C. Stark, T.D. Robinson, G.F. Snyder, L. Pueyo, N.T. Zimmerman, T. Jansen, and E.R. Nesvold. Finding the needles in the haystacks: high-fidelity models of the modern and archean solar system for simulating exoplanet observations. *Publications of the Astronomical Society of the Pacific*, 129(982):124401, 2017.

[87] F. Roddier and C. Roddier. Stellar coronograph with phase mask. *Publications of the Astronomical Society of the Pacific*, 109(737):815–820, 1997.

[88] J.B. Ruffio, B. Macintosh, J.J. Wang, L. Pueyo, E.L. Nielsen, R.J. De Rosa, I. Czekala, M.S. Marley, P. Arriaga, V.P. Bailey, and T. Barman. Improving and assessing planet sensitivity of the GPI exoplanet survey with a forward model matched filter. *The Astrophysical Journal*, 842(1):14, 2017.

[89] Science and Technology Definition Team. Exo-s: Starshade probe-class, exoplanet direct imaging mission concept, final report. `https://exoplanets.nasa.gov/stdt/Exo-S_Starshade_Probe_Class_Final_Report_150312_URS250118.pdf`.

[90] S. Seager, N.J. Kasdin, J. Booth, D. Lisman, S. Shaklan, S. Warwick, M. Greenhouse, B. Macintosh, M. Vess, and D. Webb. Starshade rendezvous probe. 2019.

[91] S. Seager and D.D. Sasselov. Theoretical transmission spectra during extrasolar giant planet transits. *The Astrophysical Journal*, 537(2):916, 2000.

[92] S. B. Shaklan, M.C. Noecker, T. Glassman, A.S. Lo, P.J. Dumont, N.J. Kasdin, E.J. Cady, R. Vanderbei, and P.R. Lawson. Error budgeting and tolerancing of starshades for exoplanet detection. In *Space Telescopes and Instrumentation 2010: Optical, Infrared, and Millimeter Wave*, volume 7731, page 77312G, Aug. 2010.

[93] D. Sirbu. *Occulter-based high-contrast exoplanet imaging: Design, scaling, and performance verification*. PhD thesis, Princeton University, Princeton (NJ), 2014.

[94] D. Sirbu, R.J. Vanderbei, and N.J. Kasdin. Diffractive analysis of limits of an occulter experiment. In *Optical, Infrared, and Millimeter Wave*, volume 9143 of *Space Telescopes and Instrumentation*, page 9143P, 2014.

[95] A. Sommerfeld. Lectures on theoretical physics: optics. *Academic press*, 4, 1954.

[96] R. Soummer, L. Pueyo, and J. Larkin. Detection and characterization of exoplanets and disks using projections on Karhunen-Loève eigenimages. *The Astrophysical Journal*, 755(2):L28, 2012.

[97] R. Soummer, L. Pueyo, A. Sivaramakrishnan, and R.J. Vanderbei. Fast computation of lyot-style coronagraph propagation. *Optics Express*, 15(24):15935–15951, 2007.

[98] D.N. Spergel. A new pupil for detecting extrasolar planets. *astro-ph/0101142*, 2001.

[99] L. Spitzer. The beginnings and future of space astronomy. *American Scientist*, 50(3):473–484, 1962.

[100] M.R. Stanford and B.J. Hadwen. The noise performance of electron multiplying charge coupled devices. *IEEE Transactions on Electron Devices*, 50(5):1227–1232, 2003.

[101] H. Subedi, N.T. Zimmerman, N.J. Kasdin, and A. Riggs. Sparse aperture mask wavefront sensor testbed results. In *Optical, Infrared, and Millimeter Wave*, volume 9904 of *Space Telescopes and Instrumentation*, page 990464, 2016.

[102] H. Sun, N.J. Kasdin, and R. Vanderbei. Identification and adaptive control of a high-contrast focal plane wavefront correction system. *Journal of Astronomical Telescopes, Instruments, and Systems*, 4(4):049006, 2018.

[103] W. A. Traub. Direct imaging of exoplanets. In *Exoplanets*. 2010.

[104] W.A. Traub and K.W. Jucks. A possible aeronomy of extrasolar terrestrial planets. In M. Mendillo, A. Nagy, and J.H. Waite, editors, *Atmospheres in the solar system: Comparative aeronomy*, pages 369–380. American geophysical union, 2002.

[105] R. Vanderbei, D. Spergel, and N. J. Kasdin. Circularly symmetric apodization via star-shaped masks. *The Astrophysical Journal*, 599(1):686, 2003.

[106] R.J. Vanderbei. Fast fourier optimization: Sparsity matters. *Mathematical Programming Computation*, pages 1–17, 2012.

[107] R.J. Vanderbei, E.J. Cady, and N.J. Kasdin. Optimal occulter design for finding extrasolar planets. *Astrophysical Journal*, page 665, 2007.

[108] J.J. Wang, J.B. Ruffio, R.J. De Rosa, J. Aguilar, S.G. Wolff, and L. Pueyo. pyKLIP: PSF subtraction for exoplanets and disks. *ascl*, pages ascl–1506, 2015.

[109] A. N. Wilkins, M. W. McElwain, T. J. Norton, B. J. Rauscher, J. F. Rothe, M. Malatesta, G. M. Hilton, J. R. Bubeck, C. A. Crady, and D. J. Lindler. Characterization of a photon counting emccd for space-based high contrast imaging spectroscopy of extrasolar planets. *Proc. SPIE*, 9154:91540C, 2014.

[110] S.S. Wilks. The large-sample distribution of the likelihood ratio for testing composite hypotheses. *The annals of mathematical statistics*, 9(1):60–62, 1938.

[111] A. Wolszczan and D.A. Frail. A planetary system around the millisecond pulsar PSR1257+12. *Nature*, 355(6356):145–147, 1992.

[112] G.R. Woodcock. Concept analysis and discussion: observations of extrasolar planets with an lst. *Future Space Transportation Systems Analysis*, page 135–137, 1974.